Wachstum und Transporteigenschaften dünner Co-basierter Heusler-Filme

Dissertation
zur Erlangung des Grades

DOKTOR DER NATURWISSENSCHAFTEN

am Fachbereich 08
der Johannes Gutenberg-Universität
in Mainz

Horst Schneider
geboren in Wiesbaden

JG|U
JOHANNES GUTENBERG
UNIVERSITÄT MAINZ

Mainz, 2010

1. Berichterstatter: *entfernt aus Datenschutzgründen*
2. Berichterstatter: *entfernt aus Datenschutzgründen*
Tag der mündlichen Prüfung: 3. November 2010

CONTENTS

Introduction 1

1 Heusler Compounds 5
- 1.1 General Properties 6
- 1.2 $Co_2Cr_{0.6}Fe_{0.4}Al$ 9
- 1.3 $Co_2Mn_{1-x}Fe_xSi$ 10

2 Thin Film Deposition and Characterization 17
- 2.1 Substrates 18
- 2.2 Sputter Deposition 21
- 2.3 Pulsed Laser Deposition 24
- 2.4 X-Ray Diffraction 28
- 2.5 X-Ray Reflectometry 30
- 2.6 Electron Diffraction 31
- 2.7 Bulk Magnetometry 33
- 2.8 Transmission Electron Microscopy 34
- 2.9 Nuclear Magnetic Resonance 34
- 2.10 Morphology 35

3 Heusler Thin Films 37
- 3.1 Sputter Deposition of $Co_2Cr_{0.6}Fe_{0.4}Al$ 37
- 3.2 Sputter Deposition of Co_2FeSi 41
- 3.3 Pulsed Laser Deposition of $Co_2Mn_{1-x}Fe_xSi$ 55

4 Electronic Transport **63**
4.1 Experimental Considerations 63
4.2 Zero-Field Resistivity 68
4.3 Magnetoresistance 71
4.4 Hall Effect 75

5 Further Characterization **93**
5.1 Kerr Magnetometry 93
5.2 Photoemission Spectroscopy 99
5.3 X-Ray Magnetic Circular Dichroism 101

Summary **109**

A Sample Patterning **111**

B Hall Resistivity and Hall Conductivity **113**

Bibliography **115**

Acknowledgments **141**

List of Publications **143**

Lebenslauf **147**

LIST OF FIGURES

1 Principle of the GMR effect. 2
2 Principle of the TMR effect. 3

1.1 The $L2_1$ “Heusler” structure. 6
1.2 Magnetization of Heusler compounds. 7
1.3 Calculated density of states of $Co_2Cr_{0.6}Fe_{0.4}Al$. 9
1.4 Calculated density of states of $Co_2Mn_{1-x}Fe_xSi$. 12
1.5 Magnetization of $Co_2Mn_{1-x}Fe_xSi$. 13

2.1 RHEED patterns of an MgO substrate. 20
2.2 Sputter deposition chamber. 22
2.3 Co_2FeSi sputtering target. 22
2.4 Pulsed laser deposition system. 25
2.5 Portable vacuum system. 26
2.6 Target carousel for the pulsed laser deposition system. 27
2.7 The Ewald construction. 30
2.8 Geometry of a rotating crystal X-ray diffraction experiment. 31
2.9 Reflectometry and refraction. 31
2.10 Ewald sphere construction for a RHEED experiment. 32

3.1 ω–2θ scan of a $Co_2Cr_{0.6}Fe_{0.4}Al$ film deposited at room temperature. . . . 38
3.2 Structure vs. annealing temperature in $Co_2Cr_{0.6}Fe_{0.4}Al$. 39
3.3 Magnetization vs. annealing temperature in $Co_2Cr_{0.6}Fe_{0.4}Al$. 40
3.4 $Co_2Cr_{0.6}Fe_{0.4}Al$ transmission electron diffraction. 41
3.5 Bragg scan of a sputter deposited Co_2FeSi / Al_2O_3 film. 42

3.6 Finite size oscillations in Co_2FeSi. 43
3.7 Reflectometry of a Co_2FeSi / Al_2O_3 sample. 44
3.8 HKL-scan of a Co_2FeSi / Al_2O_3 film. 45
3.9 φ scan of a Co_2FeSi / Al_2O_3 film. 46
3.10 Lattice mismatch between Co_2FeSi and Al_2O_3. 47
3.11 AFM image of a Co_2FeSi film. 48
3.12 Bragg scan of a Co_2FeSi / MgO film. 49
3.13 φ scan of a Co_2FeSi / MgO film. 50
3.14 TEM image of a Co_2FeSi / MgO film. 50
3.15 Integrated intensities of equivalent reflections in Co_2FeSi / Al_2O_3. 51
3.16 X-ray intensities and Co-Si disorder. 52
3.17 X-ray intensities and Fe excess. 53
3.18 Magnetic properties of Co_2FeSi. 54
3.19 Interplay of structure and magnetism in Co_2FeSi. 55
3.20 Droplets on laser deposited films. 56
3.21 RHEED of Co_2FeSi / Cr / MgO. 59
3.22 RHEED of Co_2FeSi / Cr / MgO, continued. 60
3.23 Bragg scan of Co_2FeSi / Cr / MgO. 60
3.24 Magnetic properties of $Co_2Mn_{1-x}Fe_xSi$. 61

4.1 Denotation for transport experiments. 65
4.2 Transport structures. 65
4.3 Effect of Al cap on transport properties. 66
4.4 Temperature dependent resistivity of Co_2FeSi. 69
4.5 Resistivity of nanocrystalline Co_2FeSi. 71
4.6 Magnetoresistance of Co_2FeSi. 72
4.7 High-field magnetoresistance of Co_2FeSi. 73
4.8 Hall resistivity in ferromagnets. 75
4.9 Scattering mechanisms in the anomalous Hall effect. 77
4.10 Scaling behavior of the anomalous Hall conductivity. 79
4.11 Hall effect in a sputtered Co_2FeSi films. 80
4.12 Anomalous Hall effect in sputtered Co_2FeSi samples. 82
4.13 Hall effect in laser ablated Co_2FeSi samples. 83
4.14 Hall effect in laser ablated $Co_2Mn_{1-x}Fe_xSi$ samples. 84
4.15 Anomalous Hall effect in $Co_2Mn_{1-x}Fe_xSi$ samples. 85
4.16 Dispersion relations and Fermi surfaces of $Co_2Mn_{1-x}Fe_xSi$. 86
4.17 Scaling of the anomalous Hall effect: theory and experiment. 88
4.18 Scaling of the anomalous Hall effect: repulsive impurity potential. 90

5.1 Magnetic anisitropy of Co_2FeSi / Al_2O_3. 94
5.2 Magnetic anisitropy of Co_2FeSi / MgO. 95
5.3 MOKE: experimental setup. 96
5.4 Thickness dependent MOKE and loop symmetrization. 97
5.5 LEED pattern of a Co_2FeSi film. 100
5.6 Spin resolved photoemission spectra. 101
5.7 Principle of XMCD spectroscopy. 102
5.8 TEY and transmitted intensity of a Co_2FeSi film. 104
5.9 X-ray absorption spectra of a Co_2FeSi film. 105
5.10 XMCD spectra of a Co_2FeSi film. 106
5.11 Reconstructed density of states for $Co_2Mn_{1-x}Fe_xSi$. 107

LIST OF TABLES

1.1 Disorder in Heusler compounds. 8

2.1 Properties of substrate and buffer layer materials. 19
2.2 Scattered intensities for the Heusler structure. 29

4.1 Magnetoresistance of $Co_2Mn_{1-x}Fe_xSi$. 74

INTRODUCTION

The discovery of the giant magnetoresistance (GMR) effect in 1988 is generally considered the hour of birth for spintronics [1–3]. This interdisciplinary field is an extension of traditional electronics: the manipulation and measurement of the electron spin in addition to its charge is expected to result in devices such as fast non-volatile memory [4], programmable logic circuits [5] or magnetic field sensors [6]. GMR elements have been integrated in hard disk read heads and caused a rapid increase of storage density. However, for future demands the GMR effect is deemed too small and therefore no longer feasible. It many cases it has been superseded by devices based on the tunneling magnetoresistance (TMR) effect.

Both GMR and TMR effects are based on two ferromagnetic layers separated by a normal metal and an insulator, respectively. The exchange split d bands result in an imbalance of spin up and spin down states at the Fermi energy. If the magnetization directions of the two ferromagnets are parallel, the electric resistance is low. If the magnetization of one electrode is reversed, the resulting resistance will increase. Figures 1 and 2 outline the different physical processes responsible for these two magnetoresistance effects.

The asymmetry of the majority and the minority charge carriers at the Fermi level is quantified [7] by the spin polarization

$$P = \frac{n_{\uparrow}(E_{\mathrm{F}}) - n_{\downarrow}(E_F)}{n_{\uparrow}(E_F) + n_{\downarrow}(E_F)}.$$

In order to fabricate smaller circuits, large magnetoresistive effects are indispensable. A straightforward way to achieve this is the use of electrodes with high spin polarization. For the optimal case $P = \pm 1$ one spin direction has metallic character whereas

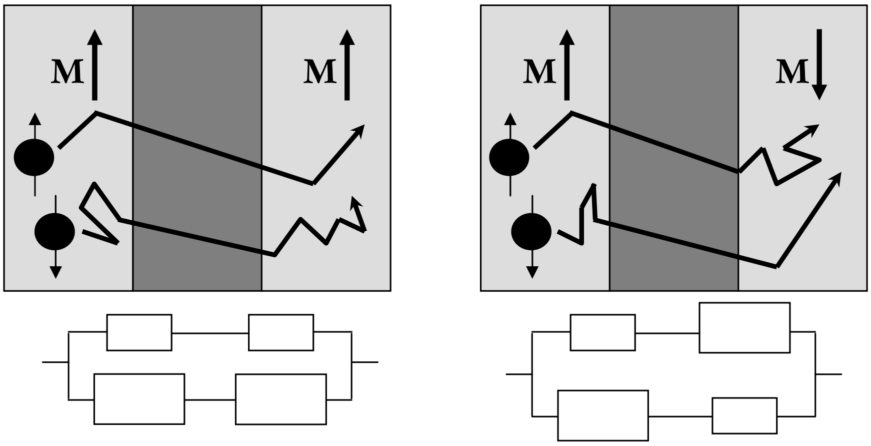

Figure 1: Principle of the GMR effect: The scattering rate for electrons with spin aligned parallel to the magnetization in the ferromagnetic electrodes and at the interfaces is low compared with electrons with opposite spin direction. If the two spin currents are independent, the different processes can be depicted as a circuit of Ohmic resistors.

the opposite direction has a band gap at the Fermi level. Due to this peculiarity, these materials have been named half-metals or half-metallic ferromagnets [8].

Half-metallicity has been predicted for several materials: oxide perovskites [9] and double perovskites [10], Fe_3O_4 [11] and CrO_2 [12]. However, up to now solid experimental evidence for a nearly complete spin polarization was found only for $La_{2/3}Sr_{1/3}MnO_3$ at low temperatures [13, 14]. Unfortunately, a Curie temperature of 345 K results in a dramatically decreased spin polarization at room temperature.

Due to the limited success of the materials mentioned above, the focus of attention has shifted toward Heusler and half-Heusler compounds. A large number of these intermetallic compounds has been predicted to be half-metallic [15]. With Curie temperatures of up to 1100, K a high spin polarization at room temperature is more likely.

The investigation of some members of this materials class—$Co_2Cr_{0.6}Fe_{0.4}Al$ as well as the alloyed series $Co_2Mn_{1-x}Fe_xSi$—has been the scope of this work. An overview of the properties of Heusler compounds in general as well as the investigated materials in particular will be given in chapter 1.

In order to analyze their properties thin film samples with a thickness of 100 nm and below were fabricated. This particular sample geometry allows the application of very high current densities parallel to the surface. Furthermore the *in vacuo* deposition of the films results in very clean surfaces. This is necessary for sur-

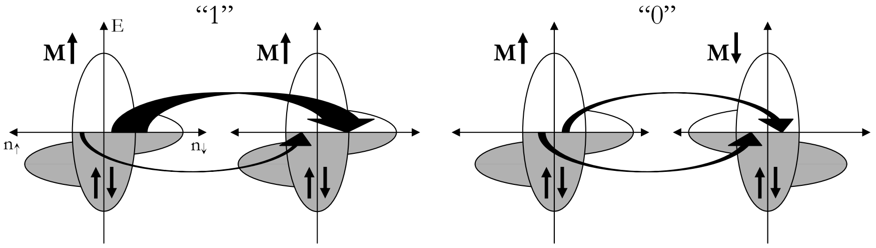

Figure 2: Principle of the TMR effect: Fermi’s Golden Rule allows electrons only to tunnel from occupied into unoccupied states. Assuming independent spin currents and a spin conserving tunneling process, for the parallel alignment of the magnetization a low resistance is caused by the spin down channel.

face sensitive measurement techniques and the fabrication of multilayer structures, employed for example in GMR and TMR devices. Chapter 2 details the deposition techniques used to prepare the samples as well as the characterization methods used to determine film quality. Chapter 3 gives the results for $Co_2Cr_{0.6}Fe_{0.4}Al$ and $Co_2Mn_{1-x}Fe_xSi$ films deposited under different conditions.

As mentioned above, a high current density allows precise electronic transport experiments. Since these properties are governed by electrons at the Fermi surface, these measurements can be used to gain insight into the electronic structure of the Heusler materials. Chapter 4 presents the result of magnetoresistance and Hall effect experiments for optimized $Co_2Mn_{1-x}Fe_xSi$ samples. The results are compared with calculated electronic structures and general transport theories in ferromagnets. It will be shown that the experimental findings are compatible with the theoretical predictions.

Thin film samples were also provided to external research groups. Their investigation techniques and the results relevant for this work are presented in chapter 5. Especially X-ray magnetic circular dichroism data reinforces the picture found by transport experiments.

CHAPTER 1

HEUSLER COMPOUNDS

In 1903, Friedrich Heusler reported that some alloys consisting of copper, manganese, and a main group metal are ferromagnetic although their constituents are paramagnetic [16, 17]. In order to resolve this discrepancy and to gain further insight into the magnetism of solids, these and similar materials were closely investigated both experimentally and theoretically.

Today the group of Heusler compounds contains a large number of members, which exhibit a wealth of diverse properties [18, 19]. For example the "prototypical" Heusler compound Cu_2MnAl shows localized ferromagnetic order [20]. If Cu is substituted with Ni, incommensurate antiferromagnetic order is observed [21]. Fe_2VAl is a semiconductor [22], Ni_2NbAl is a superconductor [23]. In systems like Ni_2MnGa a large magnetically induced shape memory effect is observed [24]. However, despite their different properties, Heusler compounds possess physical and chemical similarities, which will be reviewed in the first part of this chapter.

Thin film samples of $Co_2Cr_{0.6}Fe_{0.4}Al$ and $Co_2Mn_{1-x}Fe_xSi$ have been prepared and investigated during the course of this work. They belong to a group of ferromagnetic Heusler compounds that are expected to possess a spin polarization of up to 100 % [8, 25–28]. Additionally, they order magnetically considerably above room temperature and are closely lattice-matched to standard semiconductor materials. Because of these properties they are deemed very promising candidates for a multitude of spintronic applications [29–31]. However, despite numerous experimental efforts, solid evidence of high spin polarization has been scarce until now [31, 32]. In the second part of this chapter, the specific findings for the investigated materials are summarized.

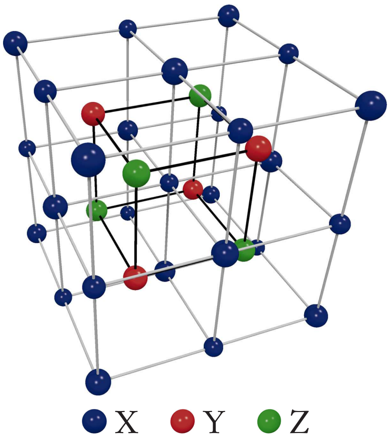

Figure 1.1: The fully ordered $L2_1$ “Heusler” structure.

1.1 General Properties

Heusler compounds are a class of intermetallic compounds with the stoichiometry X_2YZ, where X and Y are transition metal elements while Z is a main group element. In the fully ordered case they crystallize in the $L2_1$ “Heusler” structure (space group $Fm\overline{3}m$), which is shown in figure 1.1. Multiple equivalent descriptions of this structure exist, but for the needs of this work it is best to be considered as four interpenetrating fcc lattices, each containing only one element. The sublattices containing X atoms are located at $(0, 0, 0)$ and $(\frac{1}{2}a, \frac{1}{2}a, \frac{1}{2}a)$, the Y and Z atoms are located at $(\frac{1}{4}a, \frac{1}{4}a, \frac{1}{4}a)$ and $(\frac{3}{4}a, \frac{3}{4}a, \frac{3}{4}a)$, respectively.

It was realized early that the occurrence of ferromagnetism in the Heusler compounds is closely connected with the $L2_1$ crystal structure [38]. For X_2MnZ compounds with more than 28 valence electrons per unit cell it was shown by neutron diffraction that localized magnetic moments are situated on the Mn sites [20, 33, 39]. Their magnitude has a value of approximately 4 μ_B/atom, independent of the X and Z atoms [40]. It decreases significantly and might even vanish if the Mn atoms are not located on an fcc sublattice [38].

For Co_2MnZ compounds as well as compounds not containing Mn a different behavior is observed [33, 39]. Although the main fraction of the magnetization is still localized at the Y sites, additional contributions, which couple ferromagnetically to the Y moments, are found at the X atoms. Furthermore, the total magnetic moment shows a linear dependence on the number of valence electrons per unit cell. Again for these compounds the highest magnetization values are reported if the samples show the $L2_1$ structure. These results are summarized in figure 1.2.

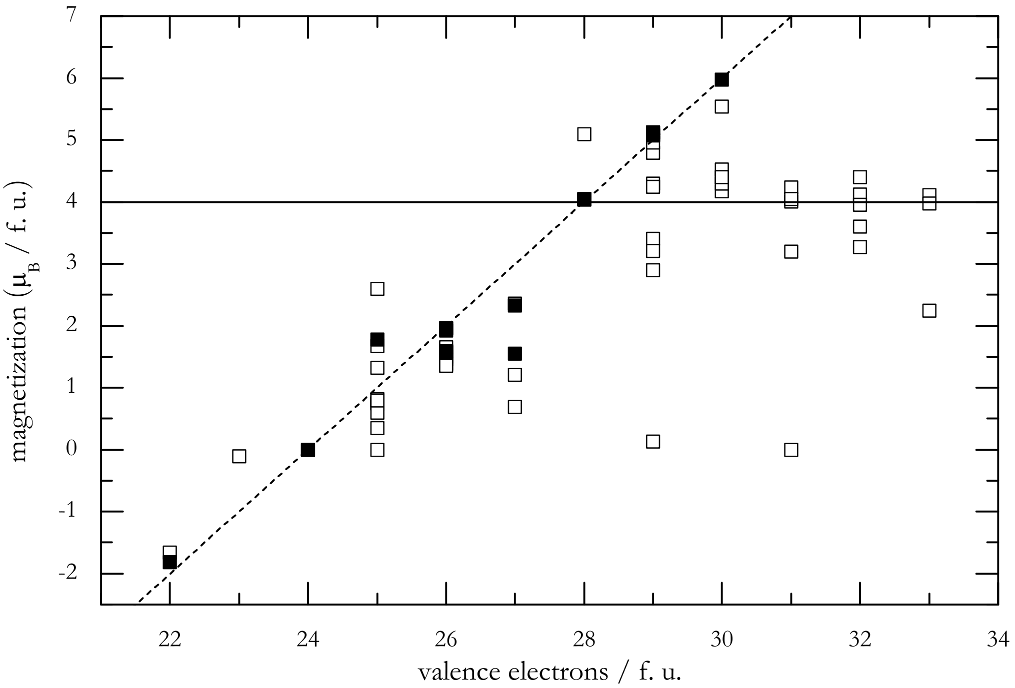

Figure 1.2: Experimental magnetization values of Heusler compounds as a function of the valence electron count (values taken from references 33–35). Full symbols represent compounds that have been predicted to be half-metallic [25, 36, 37]. The dashed line indicates the Slater-Pauling rule, which gives the expected theoretical magnetization values for the fully spin polarized materials.

The linear behavior of the spontaneous magnetization was shown to be an extension of the Slater-Pauling rule [41–43]. Its general form states that in ferromagnets the sum of the number of spin-up ($Z_\uparrow$) and spin-down ($Z_\downarrow$) electrons per atom must be equal to the number of valence electrons (Z) per atom. The magnetization is determined from their difference. Combining these two equations results in $M = (Z - 2Z_\downarrow)\ \mu_B$/atom. For the half-metallic Heusler compounds it was shown that the four atoms in the unit cell have a constant total number of 12 spin minority electrons [25, 43, 44]. The magnetization therefore depends linearly on the number of valence electrons:

$$M = (Z - 24)\mu_B/\text{f. u.} \tag{1.1}$$

The experimental determination of the sample magnetization therefore serves as a rather simple method to select potential half-metals. This is also illustrated in figure 1.2. However, the relative position of majority and minority states with respect

Table 1.1: Relevant types of structural disorder in Heusler compounds. X, Y, and Z indicate which fraction of each element is located on the respective sublattice.

Structure	(0, 0, 0)	$\left(\frac{1}{4}a, \frac{1}{4}a, \frac{1}{4}a\right)$	$\left(\frac{1}{2}a, \frac{1}{2}a, \frac{1}{2}a\right)$	$\left(\frac{3}{4}a, \frac{3}{4}a, \frac{3}{4}a\right)$
$L2_1$	X	Y	X	Z
B2	X	$Y_{1/2}Z_{1/2}$	X	$Y_{1/2}Z_{1/2}$
DO_3	$X_{2/3}Y_{1/3}$	$X_{2/3}Y_{1/3}$	$X_{2/3}Y_{1/3}$	Z
	$X_{2/3}Z_{1/3}$	Y	$X_{2/3}Z_{1/3}$	$X_{2/3}Z_{1/3}$
A2	$X_{1/2}Y_{1/4}Z_{1/4}$	$X_{1/2}Y_{1/4}Z_{1/4}$	$X_{1/2}Y_{1/4}Z_{1/4}$	$X_{1/2}Y_{1/4}Z_{1/4}$

to the Fermi energy cannot be inferred from the fulfillment of equation 1.1 alone. It is therefore no proof of a completely spin polarized material. Additionally it should be noted that the Slater-Pauling rule only accounts for the spin magnetic moment. However, a significant orbital contribution to the total magnetization has been observed in Heusler compounds [45–47]. It should therefore be kept in mind that real systems are not perfectly half-metallic, because spin orbit interaction causes a mixing of the spin directions. Nevertheless, in Heusler compounds this reduction is considerably less than 1 % [48].

The theoretical predictions of half-metallicity require $L2_1$ ordered Heusler compounds [25]. Depending on the method of crystal growth and the specific Heusler compound, this might be difficult or impossible to realize experimentally [40, 49, 50]. Instead, to a varying degree one of the following types of disorder is obtained. In some cases, they will drastically alter the spin polarization and the magnetic properties of a Heusler compound.

The disordering mechanism most commonly encountered is the intermixing of Y and Z atoms. The maximum degree of disorder is reached if half of the Y atoms are randomly distributed on Z sites and vice versa. In this case the B2 (CsCl-type) structure is present in the Heusler compound. XY- or XZ-disorder will result in the DO_3 (Fe_3Al) structure. If random intermixing between all sublattices occurs the result will be an A2 (bcc) lattice. These relevant cases of disorder are summarized in table 1.1. In principle, further types of disorder are possible [51] but they are unfeasible and have not been observed in real samples.

It has been argued that the hybridization of next-nearest neighbor Co atoms is the principal source of the half-metallic gap in the Co_2YZ compounds [25]. Consequently, it is expected that B2 disorder has only a small effect on spin polarization and magnetization [36]. For DO_3 and A2 disorder on the other hand, Co atoms can be found on nearest neighbor lattice sites. This introduces minority states at

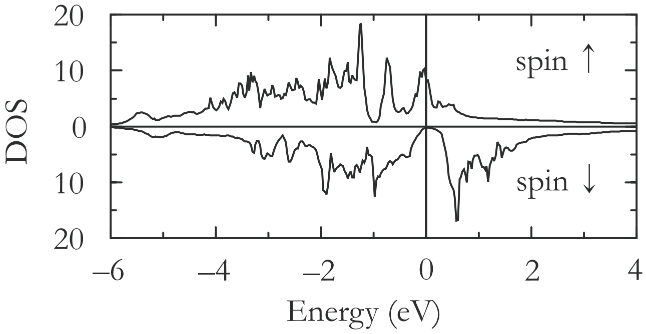

Figure 1.3: Calculated spin-resolved density of states for $Co_2Cr_{0.6}Fe_{0.4}Al$ [59].

the Fermi energy, which lowers both spin polarization and magnetic moments significantly [52–54]. Experimental evidence for this interplay between disorder and magnetism has been published in references 55 and 56. A similar problem is the deviation from the X_2YZ sample composition [57, 58]. With the same arguments as before it can be seen that also certain types of off-stoichiometry can be responsible for a reduction of the spin polarization.

1.2 $Co_2Cr_{0.6}Fe_{0.4}Al$

The system $Co_2Cr_{1-x}Fe_xAl$ has been subject to numerous theoretical investigations [25, 26, 52, 55, 59–61]. For Co_2CrAl half-metallicity has been predicted independent of the calculational technique [25, 55]. However, a Curie temperature of 335 K is too low for applications [62]. One possibility to raise the magnetic ordering temperature is the substitution of Cr with Fe. The maximum of 1000 K is reached with Co_2FeAl [63]. The downside of this approach is the closing of the half-metallic gap. The question whether at high Fe concentrations full spin polarization is retained [26] or not [52] is still an open question. The compound $Co_2Cr_{0.6}Fe_{0.4}Al$ investigated in this work seems to be the best compromise between a high Curie temperature and a high spin polarization. T_C of bulk samples was determined to be 750 K [59]. For $x = 0.4$ all band structure calculations predict a high spin polarization [26, 52, 59]. The reason as shown in figure 1.3 is a high density of majority electron states at the Fermi energy caused by a van Hove singularity. This allows the conservation of a high spin polarization even if due to disorder a small finite density of minority states is introduced.

A large negative magnetoresistive effect was observed in compressed powder samples of $Co_2Cr_{0.6}Fe_{0.4}Al$, which was explained with intergranular tunneling [59].

Bulk samples could be prepared in the $L2_1$ structure [56]. For sputtered polycrystalline [64] and epitaxial [65–67] thin films the fully ordered Heusler structure was not observed. Nevertheless tunneling junctions based on these films showed a maximum TMR ratio[1] of 101 % [68], if an amorphous tunneling barrier was used. The Jullière model [7] gives a spin polarization of 62 %, which is clearly above any value reported for conventional ferromagnets. Whether the reduced spin polarization is intrinsic or caused by imperfect tunneling junctions is not yet answered. $L2_1$ ordered films grown by molecular beam epitaxy have been claimed [69], but both the reported magnetization and tunneling spin polarization are exceedingly low. Fully epitaxial tunneling junctions show a magnetoresistive effect of 240 % [70]. However, the presence of a crystalline MgO tunneling barrier causes a spin filtering which enhances the TMR ratio [71]. Therefore, an intrinsic value of the spin polarization cannot easily be deduced.

1.3 $Co_2Mn_{1-x}Fe_xSi$

Just like $Co_2Cr_{0.6}Fe_{0.4}Al$, Co_2MnSi has received a lot of attention due to its predicted half-metallicity [28, 72, 73]. A Curie temperature of 985 K is well suited for applications [40]. X-ray diffractograms of bulk samples commonly show growth in the $L2_1$ structure [40, 74], but in some samples a small amount of DO_3 disorder between Co and Mn was detected [75]. Sputtered [31] or laser ablated [46] thin films grow epitaxially and they show a high degree of atomic order. Tunneling experiments with Co_2MnSi electrodes have been demonstrated [31, 32]. These junctions showed very high magnetoresistive effects at low temperatures. Regrettably, the observed tunneling magnetoresistive ratio dropped rapidly from 570 % at 2 K down to 70 % at room temperature [76], a value which can be obtained with conventional ferromagnetic electrodes [77].

The band structures mentioned above describe the electronic structure at absolute zero temperature. The reduction of the spin polarization at elevated temperatures has only been analyzed to a small extend so far. One proposed mechanism is the thermal excitation of magnons [78], which results in a $T^{3/2}$-dependence of the spin polarization, analogous to the decrease in magnetization [79]. However, the high Curie temperature of Co_2MnSi and its weak T-dependence of the magnetization in the examined temperature region seem to rule out this mechanism as a major source of the problem. A reduced magnetization [80] and a more pronounced temperature dependence [78] are often encountered at surfaces and interfaces of

---

[1] For all TMR ratios presented in this thesis the "optimistic" definition $\left(R_{\uparrow\downarrow} - R_{\uparrow\uparrow}\right)/R_{\uparrow\uparrow}$ is used.

ferromagnetic samples. However, XMCD experiments on Co_2MnSi samples did not show a significant effect at the interface either [81]. A further intrinsic possibility is the thermal excitation of electrons at the Fermi energy [82, 83]. A recent third interpretation considers the impact of electron-electron interactions on the half-metallic properties [84]. The main consequence in the context here is the occurrence of superpositions between electron excitations and magnons [85]—so-called non-quasiparticle states—in the minority gap at finite temperatures. Further approaches put the blame on problems with the insulating barrier, which are the source of a spin-*independent* electron tunneling. As possible extrinsic causes localized states [78] or bosonic excitations in the insulating barrier [86, 87] have been proposed.

It is important to note that the electronic band structure of Co_2MnSi is unfavorable with respect to the problems mentioned above. All calculations show a low majority density of states at E_F (see for example the top of figure 1.4), in contrast to $Co_2Cr_{0.6}Fe_{0.4}Al$ [28, 72, 88]. This means that even small effects will have a significant influence on the spin polarization. Furthermore, the Fermi level seems to be positioned close to the border of the minority spin gap, which increases the impact of both thermally excited and non-quasiparticle states.

For Co_2FeSi *ab initio* calculations do not show full spin polarization [25, 27]. Interestingly, these models predict magnetic moments of 5.7 μ_B/f. u. or less. This disagrees with experimental data of bulk samples, which exhibit values between 5.9 and 6 μ_B/f. u. [27, 89], in accordance with the Slater-Pauling rule [25]. In addition, a T_C of 1150 K marks the record value for Heusler compounds so far.

This discrepancy prompted for a refinement of the computational techniques used. Band structures of solids are routinely calculated using the density functional theory [90]. Exchange and correlation effects in the calculations mentioned before were treated with the local spin density approximation (LSDA). More recent publications introduced the LSDA+U formalism [27]. Here coulomb repulsion between electrons is treated in the same way as in Hubbard models: An energy penalty U is placed upon doubly occupied orbitals. The magnitude of U was chosen in such a way that the resulting band structure reproduced the correct experimental magnetization value. It was shown that this choice also opens up a half-metallic gap in the minority density of states at E_F.

This raises the question of the importance of electron-electron interactions in the investigated materials. The LSDA + U formalism is usually applied to systems with localized electrons such as transition metal oxides or rare earth elements. However, even though Heusler compounds are considered localized moment ferromagnets, their d electrons are itinerant [91]. To what extend is an on-site correlation between electrons retained in this case? Moreover, what is the origin of the strik-

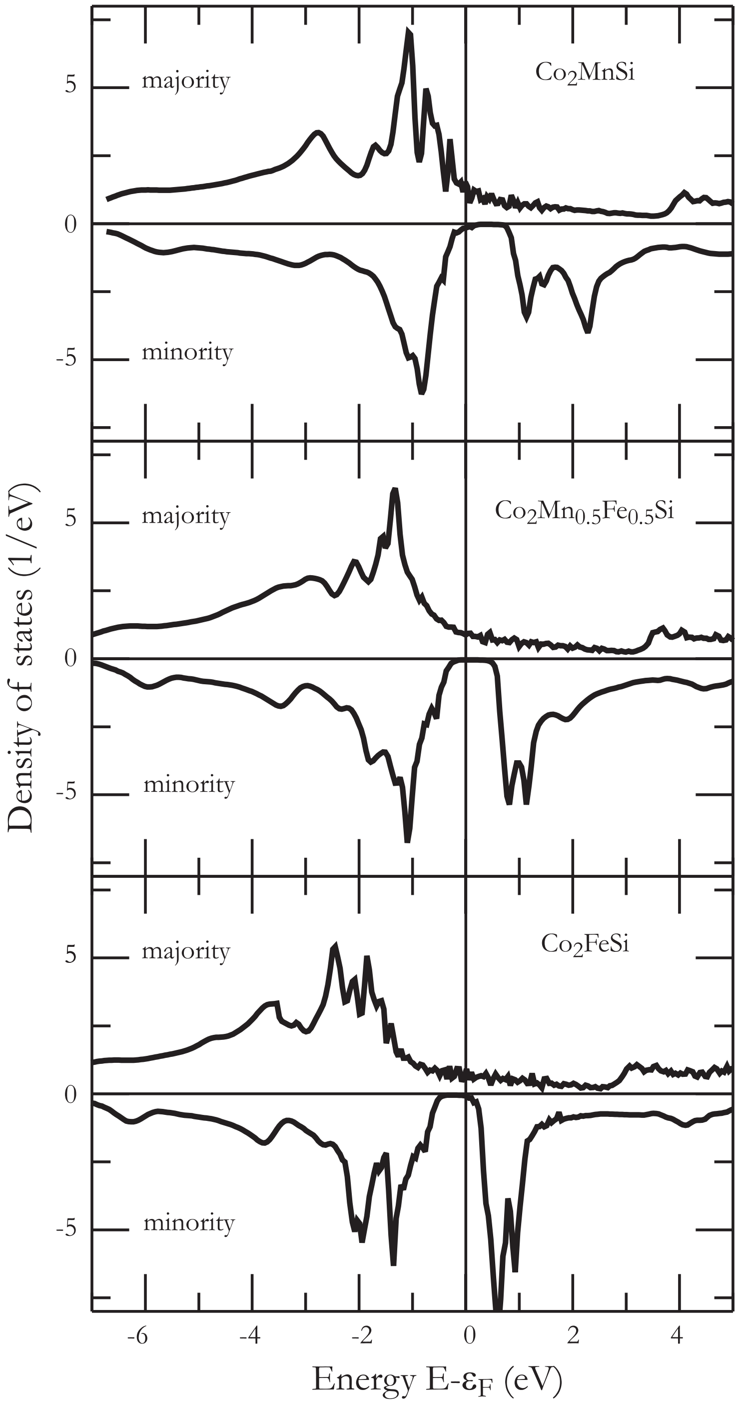

Figure 1.4: Calculated spin-resolved densities of states for $Co_2Mn_{1-x}Fe_xSi$ [88].

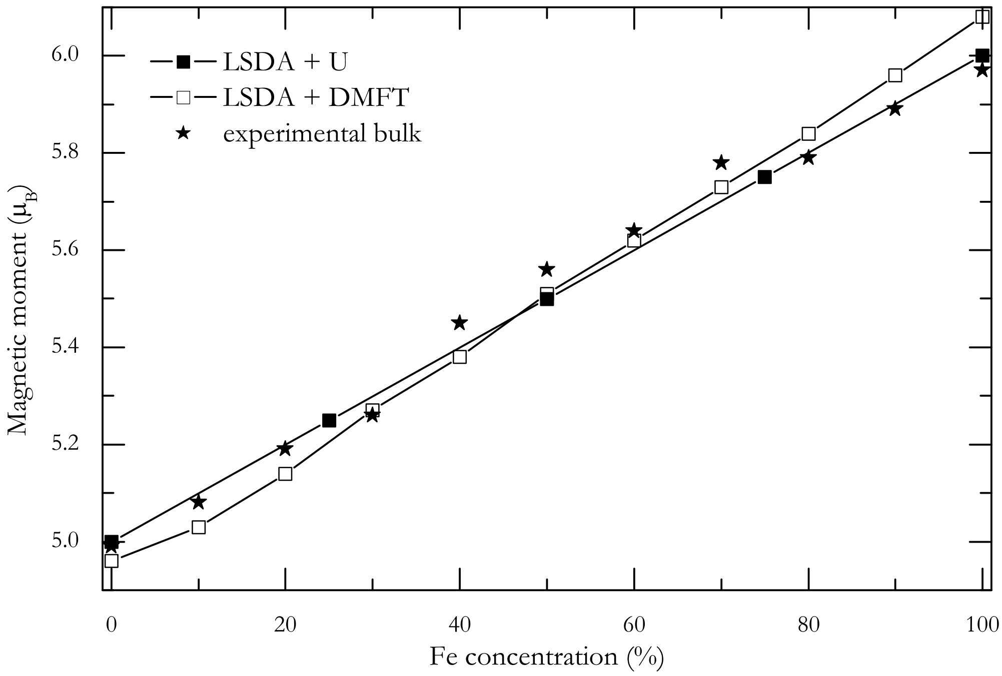

Figure 1.5: Experimental and theoretical magnetic moments of $Co_2Mn_{1-x}Fe_xSi$. The experimental bulk data and the LSDA + U calculations are reported in reference 73, the LSDA+DMFT results are taken from reference 88.

ing difference between Co_2MnSi and Co_2FeSi? It was shown by Kandpal *et al.* that in both compounds half-metallicity along with the correct experimental magnetization value is sustained over a large range of the effective Coulomb exchange interaction $U_{eff} = U - J$, where J denotes the exchange energy. Co_2MnSi is half-metallic for U_{eff} between 0 and 2 eV while for the Fe compound it is found that half-metallicity occurs for $2 \lesssim U_{eff} \lesssim 5$ eV [92].

Further theoretical investigations focused therefore on the effect of the Y atom in the alloy series $Co_2Mn_{1-x}Fe_xSi$ [73, 93]. Here a constant $U_{eff} = 2$ eV was assumed since this is the borderline value for half-metallicity in both Co_2FeSi and Co_2MnSi. The increase of the Fe content from 0 to 1 results in a shift of the Fermi energy across the half-metallic gap. The size of the gap as well as the majority density of states stay nearly constant. From these results the best temperature stability of the spin polarization is expected for $x \approx 0.5$. Experimental data from bulk samples show that the whole alloy series can be grown with the $L2_1$ structure and that the samples follow the Slater-Pauling rule very well [73] (see figure 1.5). The Heusler structure in these samples was also confirmed by XMCD [94] and NMR [95]. High-energy photoelectron spectroscopy showed indeed a shift of the Fermi energy with respect to salient features of the occupied states [93]. However, tunneling junctions based on $Co_2Mn_{0.5}Fe_{0.5}Si$ show only a comparatively low TMR ratio [96] although in this case oxidation of Mn atoms rather than intrinsic properties seem to be responsible for these poor results [97].

The interpretation of the Hall effect of $Co_2Mn_{1-x}Fe_xSi$ in chapter 4.4 is based on very recent calculations [88], which differ in two ways from the LSDA+U calculations mentioned above. First, the local correlations are treated in the framework of the dynamical mean-field theory (DMFT) [98]. The inclusion of dynamical correlations is expected to improve mainly the description of high-energy excitations. It has a sizable impact for example on photoelectric spectra [88]. The second difference concerns the calculation of the independent particle band structures shown in figure 1.4. They have been calculated by fully taking into account relativistic effects. Compared with earlier results [73] it can be seen that the properties at the half-metallic energy gap remain mostly unchanged. Again the Fermi level of Co_2MnSi is located at the top of the minority valence band, electron doping causes E_F to move across the gap.

It is important to note that according to these calculations both Co_2FeSi and Co_2MnSi are no longer half-metals. Nevertheless, the spin polarization of more than 95 % predicted here is still compatible with the published tunneling experiments. For intermediate stoichiometries the minority density of states decreases but does not vanish completely. This is an effect of the relativistic calculations, which allows for spin-orbit coupling. As discussed on page 8 this has a small effect on the spin polarization [48, 99]. This can more clearly be seen in a deviation from the Slater-Pauling rule as shown in figure 1.5.

The findings presented in this chapter show that Heusler compounds bear a considerable potential for use in spintronic applications. Computed band structures suggest a very high spin asymmetry at the Fermi energy. It seems, however, that in these materials the electronic structure is very sensitive to impurities or a finite sample temperature. Also intrinsic mechanisms like spin orbit interaction or Coulomb repulsion need to be taken into account.

Among the materials for which half-metallicity at zero temperature was postulated are those investigated in this work—$Co_2Cr_{0.6}Fe_{0.4}Al$ and $Co_2Mn_{1-x}Fe_xSi$. Experimentally, high spin polarizations have indeed been observed, but the values are strongly temperature dependent. For Co_2MnSi and Co_2FeSi, the problem seems to be an unfortunate position of the Fermi energy at the edge of the half-metallic gap. In order to improve the temperature stability of these compounds electron doping has been suggested. The Fermi energy is predicted to move across the half-metallic gap if Mn is substituted by Fe. The optimal case seems to be $Co_2Mn_{0.5}Fe_{0.5}Si$, for which the Fermi energy is located in the center of the gap. Experiments on bulk samples support this hypothesis. The magnetization of $Co_2Mn_{1-x}Fe_xSi$ follows the Slater-Pauling rule for half-metallic Heusler compounds and integral photoelectron spectra show a doping induced shift of the occupied states. However, despite these promising first results further investigations are needed to investigate the interplay between structural and electronic properties.

CHAPTER 2

THIN FILM DEPOSITION AND CHARACTERIZATION

The term “thin film” generally denotes a solid or liquid coating whose thickness is much smaller than the dimensions of the underlying material. The border between “thin” and “thick” is dependent on the specific application and ranges from one atomic monolayer to several millimeters. The films prepared and analyzed in this work had a typical thickness between 10 and 100 nm. This geometry offers several benefits over bulk samples.

Most important with respect to this work are the consequences for transport experiments. The reduced thickness allows the application of very high current densities through the sample. Consequently, a higher signal to noise ratio of the measured voltage signal may be obtained. Photolithographic patterning of the films can be used to create current leads with a typical width of 50 μm, which allows for even higher current densities. Furthermore, it enables the precise measurement of anisotropies in the transport properties. Another advantage is the possibility to obtain a very flat, clean, and well-ordered surface. This offers the chance to perform surface sensitive experiments such as photoemission spectroscopy. Alternatively, well-defined artificial superlattice or multilayer systems may be prepared. Finally, it should be noted that thin film growth is no thermal equilibrium process. In some cases, this can be used to grow crystals with a metastable structure or thin film single crystals with higher quality than their bulk counterparts.

On the other hand, the last point more often than not turns out to be a disadvantage. Usually, bulk samples can be grown with a higher structural quality than thin films. Here of specific interest for Heusler compounds is the short-range ordering. For some materials—including $Co_2Cr_{0.6}Fe_{0.4}Al$ (see page 9)—it proved complicated or even impossible to deposit $L2_1$ ordered thin films, although the corresponding bulk samples showed the Heusler structure [40, 100]. A technological challenge is the fact that during the deposition process the film material is vaporized prior to the transport to the substrate. The very high surface to volume ratio imposes high demands on the ambient conditions in order to minimize oxidation and other contaminations. This is also known to be a crucial obstacle for Heusler compounds because even a small degree of sample oxidation can cause a severe reduction of the spin polarization [76, 101].

In this chapter, the experimental techniques used during the course of this work are presented. The first part presents the two preparation methods in use: the well tested and widely used sputter deposition as well as pulsed laser deposition, which promises a higher flexibility under improved vacuum conditions. In addition, the choice of the substrates on which the films were deposited is elucidated.

Following the discussion in chapter 1, the films were primarily optimized with respect to their crystal structure and their magnetic properties. Importance was also attached to a smooth sample surface. The second part of this chapter gives a brief overview of the techniques that were used to analyze these relevant sample properties. More details on the various subjects can be found in the references.

2.1 Substrates

The properties of the underlying substrate are important factors for the structural properties of the thin film deposited on top [103, 104]. An amorphous substrate surface will result in polycrystalline or amorphous samples, because no preferential direction parallel to the surface is present [32, 49]. If on the other hand the substrate possesses an ordered surface, the first film atoms impinging on the substrate will ideally arrange in such a way that the bonding energy between them and the substrate is minimized. It is therefore energetically favorable for the film atoms to duplicate the substrate crystal structure. Further stacking of film atoms on top will result in epitaxial growth—a single-crystalline film possessing a fixed orientation with respect to the substrate below.

On the other hand, the presence of an ordered surface means that the deposited atoms are not located at their bulk equilibrium positions if film and substrate do not share the same crystal structure. The relaxation of the stress thus exerted on the film results in crystal defects, strained, or non-epitaxial growth. It is therefore very advantageous that film and substrate are closely lattice-matched. Furthermore, it is

Table 2.1: Structural properties of substrate and buffer layer materials used in this work [102]. The minimal lattice misfits defined as $(d_{\mathrm{sub}} - d_{\mathrm{film}})/d_{\mathrm{sub}}$ are given for the surface orientations in the first column. d denotes the distance between atoms along the expected growth direction. The data of the investigated compounds [59, 73] are given for comparison.

Material	Structure		Misfit with respect to	
			$Co_2Cr_{0.6}Fe_{0.4}Al$	$Co_2Mn_{1-x}Fe_xSi$
MgO (100)	fcc	$a = 4.21$ Å	3.5 %	5.2 %
Al_2O_3 $(11\bar{2}0)$	hex	$a, b = 4.76$ Å	1.5 %	3.2 %
		$c = 12.99$ Å	12 %	13 %
Fe (100)	bcc	$a = 2.87$ Å	< 0.1 %	1.7 %
Cr (100)	bcc	$a = 2.89$ Å	0.7 %	2.4 %
Ag (100)	fcc	$a = 4.09$ Å	0.7 %	2.4 %
$Co_2Cr_{0.6}Fe_{0.4}Al$	fcc	$a = 5.74$ Å		
$Co_2Mn_{1-x}Fe_xSi$	fcc	$a = 5.64$ Å		

necessary to have a clean and smooth substrate surface. Imperfections in the form of steps or particles at the surface will be the source of microscopic or macroscopic film defects. Finally, inertness and thermal stability of the interface is needed in order to prevent chemical reactions or interdiffusion between film and substrate material.

For the deposition of the cubic Heusler structure, two substrates were chosen. It can be gathered from table 2.1 that the (100)-surface of MgO forms a centered square lattice with $a_{\mathrm{MgO}} = 4.21$ Å. Since $\sqrt{2}a_{\mathrm{MgO}} \approx a_{\mathrm{Heusler}}$ it can be expected that the Heusler films grow (100)-oriented and that the unit cells are rotated by 45 ° with respect to the substrate. The successful growth of epitaxial thin Heusler films using MgO was reported in reference 105. MgO is hygroscopic and if exposed to air it will form $Mg(OH)_2$ and $MgCO_3$ at its surface [106].

In order to limit this surface degradation, the span of time the substrates were exposed to ambient conditions was minimized. To remove the reactants formed during substrate handling an *in situ* annealing step at 700 °C was performed prior to film deposition. This heat treatment also resulted in a smoother substrate surface [106]. The effect on the MgO surface is presented in figure 2.1. The photo on top shows a RHEED pattern of a substrate directly after transferring into the vacuum chamber. An ordered surface is evident from the distinct reflections. After annealing for one hour at 700 °C the reflections become line shaped, which is an

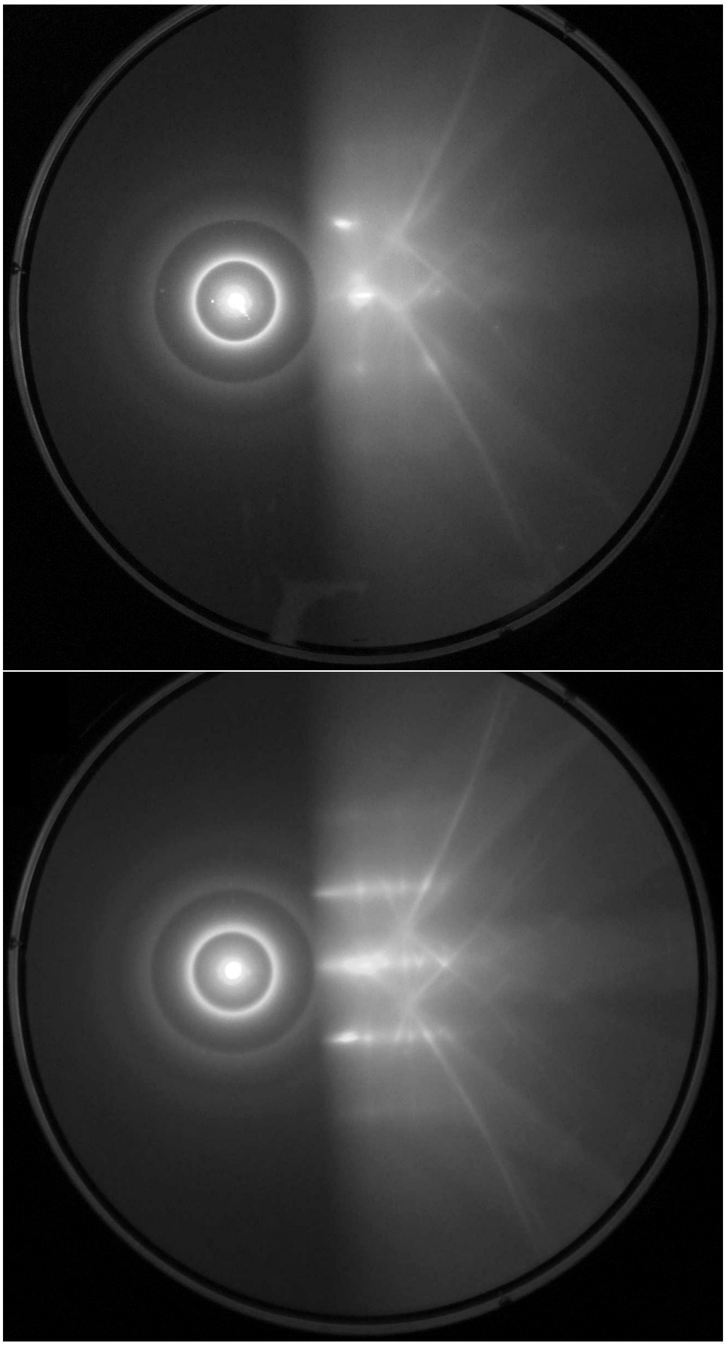

Figure 2.1: RHEED patterns of an MgO substrate before (top) and (after) vacuum annealing

indication of a smooth surface, the increased intensity suggests an increase in surface ordering [107]. Additional *ex situ* preparation procedures suggested in literature [108, 109] showed no observable improvement in surface quality and were therefore omitted.

The second substrate in use was $(11\bar{2}0)$-oriented Al_2O_3 ("a-plane sapphire"). It is inert under ambient conditions, therefore it sufficed to heat the substrate to moderate temperatures in order to remove adsorbed water or hydrocarbons. At first glance the rectangular structure of the Al_2O_3 surface—especially the large misfit along the c axis—seems to be problematic for the growth of Heusler films. Nevertheless, epitaxial growth of (110)-oriented Heusler films has been realized [65, 100].

As shown in table 2.1 the lattice misfit between the chosen substrates and the Heusler films is not optimal. The epitaxial films reported [65, 100, 105] therefore relied upon high substrate temperatures during deposition. This yields a higher kinetic energy of the adsorbed metal atoms and hence a better relaxation of the stress imposed by the substrate. However, the resulting samples showed very rough surfaces, which poses a major problem for a number of continuative experiments [65, 110–112]. In order to overcome this issue, a second approach was pursued. Before film growth, a buffer layer consisting of an elemental metal was deposited on the substrate. The structures of the buffer materials in use are better lattice-matched to the films. This is expected to enable flat, crystalline samples at lower deposition temperatures. A further reduction of lattice defects and further smoothing of the film surface might be achieved with a post-deposition annealing process [31, 32]. This method has also been applied successfully to the fabrication of epitaxial Heusler films [31, 49]. The disadvantage of this sample preparation is that the presence of a second metallic layer prohibits the conduction of transport experiments with the current flowing in the film plane.

2.2 Sputter Deposition

The term "sputtering" describes the erosion of a material by ion bombardment [113]. Its application in thin film deposition is illustrated in the left part of figure 2.2. The deposition chamber is flooded with gas—for the metallic Heusler compounds, inert Ar is used. Afterward a voltage is applied between the target material and the substrate. The gas atoms are first ionized and then accelerated toward the target. The neutral atoms or clusters sputtered from the surface are finally transported to the substrate surface. In order to increase the deposition rate, the "magnetron sputtering" technique is used. Here two ring magnets are placed concentrically behind the target. The resulting radial magnetic field in front of the cathode forces the

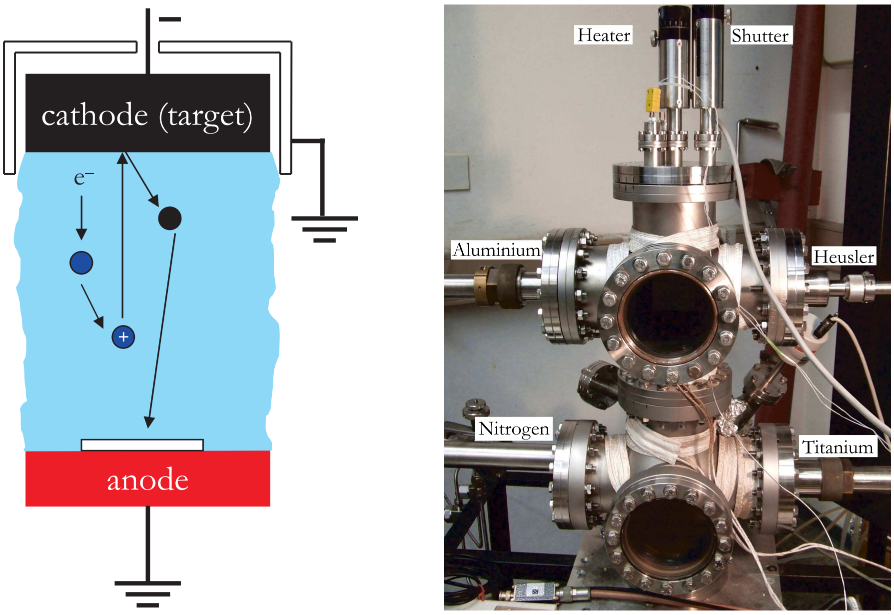

Figure 2.2: Left: Sketch of the processes relevant for sputter deposition. Right: Actual sputter deposition chamber used for the preparation of Co_2FeSi and $Co_2Cr_{0.6}Fe_{0.4}Al$.

Figure 2.3: Co_2FeSi target mounted on a sputtering cathode.

charged particles on a circular orbit close to the target surface. This will increase ionization and sputtering rates.

If the sputter target is an electrical conductor, a DC power supply can be used to drive the process. Due to charge buildup, this is not possible for dielectric targets. Instead, an RF power supply needs to be used. In order to create the DC bias voltage required for sputtering from an alternating voltage, a high pass frequency filter needs to be introduced between source and cathode. Because of their lower mass, this leads to an accumulation of electrons at the target.

Sputtering is a non-equilibrium process, therefore it can be used to deposit thin films from basically any target material. However, it should be noted that the sputter yield (the ratio between sputtered atoms and incident ions) at the target is element dependent. Also element dependent are the adsorption and desorption rates at the film surface as well as interaction of the sputtered atoms with each other and the background gas. Therefore, the constituents of a compound target should have similar characteristics with respect to these effects. Compounds of elements with similar masses and melting temperatures are therefore preferable. Otherwise, the stoichiometries of target and film might differ significantly. Deposition parameters like the applied bias voltage or substrate temperature usually have only a minor impact on the film composition.

Sputter deposition can be considered the standard technique for the preparation of Heusler compound thin films (see for example references 32, 49, 108, and 114). It was therefore chosen as one growth method in this work. The preparation of Co_2FeSi and $Co_2Cr_{0.6}Fe_{0.4}Al$ was carried out with the vacuum system shown in figure 2.2. A turbomolecular pump was utilized for evacuation to approximately 3×10^{-7} mbar. Two sputtering cathodes were flange-mounted on the top half of the chamber. One comprised the Heusler target, the other one was employed for Al sputtering. The latter was deposited on top of the Heusler films in order to protect the samples from oxidation. On the lower right hand side, a third cathode was used to sputter a Ti target. On its opposite a liquid nitrogen cold trap was mounted. The Ti atoms chemically bind residual gas and were afterward adsorbed by the cold plate of the trap. The cooled area also served to reduce the partial pressure of water. In conjunction with a bake out procedure after sample loading, the base pressure of the system could be reduced to 5×10^{-8} mbar. The substrates were glued onto a heater block. Rotation along the vertical axis allowed the choice of the target cathode, a linear shutter was placed between Heusler target and sample in order to create samples with a thickness gradient. The substrates could be heated resistively to temperatures of up to 750 °C.

In order to create the sputtering targets, polycrystalline ingots were prepared by arc melting [27, 73]. Afterward the ingots were cut into rectangular plates by spark erosion, polished, cleaned, and glued to a copper plate in order to form circular targets with a diameter of 5 cm. In figure 2.3 the boundaries between each piece can clearly be seen. This might pose a problem, because erosion of silver glue or copper from the back plate is possible. Fortunately, such contamination could not be observed by EDX analysis of the films.

2.3 Pulsed Laser Deposition

In pulsed laser deposition (PLD)—also named laser ablation—short light pulses with a duration of typically 10 – 50 ns and high energy densities of several J/cm^2 are used to vaporize the bulk target material. A sketch of the principle and the actual realization are shown in figure 2.4. The light source used in this work was a KrF excimer laser, which emits at a wavelength of 248 nm. The use of ultraviolet light in laser ablation is generally advantageous because many materials show strong absorption in this frequency region [115]. Due to the short pulse duration, the emitted light is divergent. It needs therefore first to be parallelized and then focused on an area of a few mm^2 at the target. The photon energy is initially converted into electronic excitations and subsequently into thermal, chemical, or mechanical energy. The exact nature of these energy transfer mechanisms is complex and dependent on the target material as well as the laser characteristics [116, 117]. The result is the creation of a very dense ($p \approx 100-500$ bar) and highly energetic ($E_{\text{kin}} \approx 1$ eV) plasma. It expands rapidly and forms a “plume”, which transports the vaporized target material to the substrate.

Like sputtering, PLD is a non-equilibrium deposition process. Hence, it is expected that the target stoichiometry will be carried over to the film [118]. However, due to the same substrate-vapor interaction issues as in sputter deposition, elements of a compound should again have similar masses. The main advantage of PLD is the fact that no process gas is needed during sample deposition. No throttling of the pumping power is required and ultrahigh vacuum conditions may be maintained at all times. On the other hand, the deposition rate of laser ablation is lower, which to a certain degree offsets the previously mentioned advantage. The most severe disadvantage of PLD is the formation of melt droplets caused by superheating of subsurface target regions [119]. The dimensions of these droplets can reach up to several micrometers. If they are transported to the substrate, they can obstruct further experiments. Finally, the energy to evaporate the target material is delivered only to a small target region. This limits the area over which a homogeneous film stoichiometry and thickness may be obtained. The advantage of this point is that a small amount of target material suffices for thin film deposition.

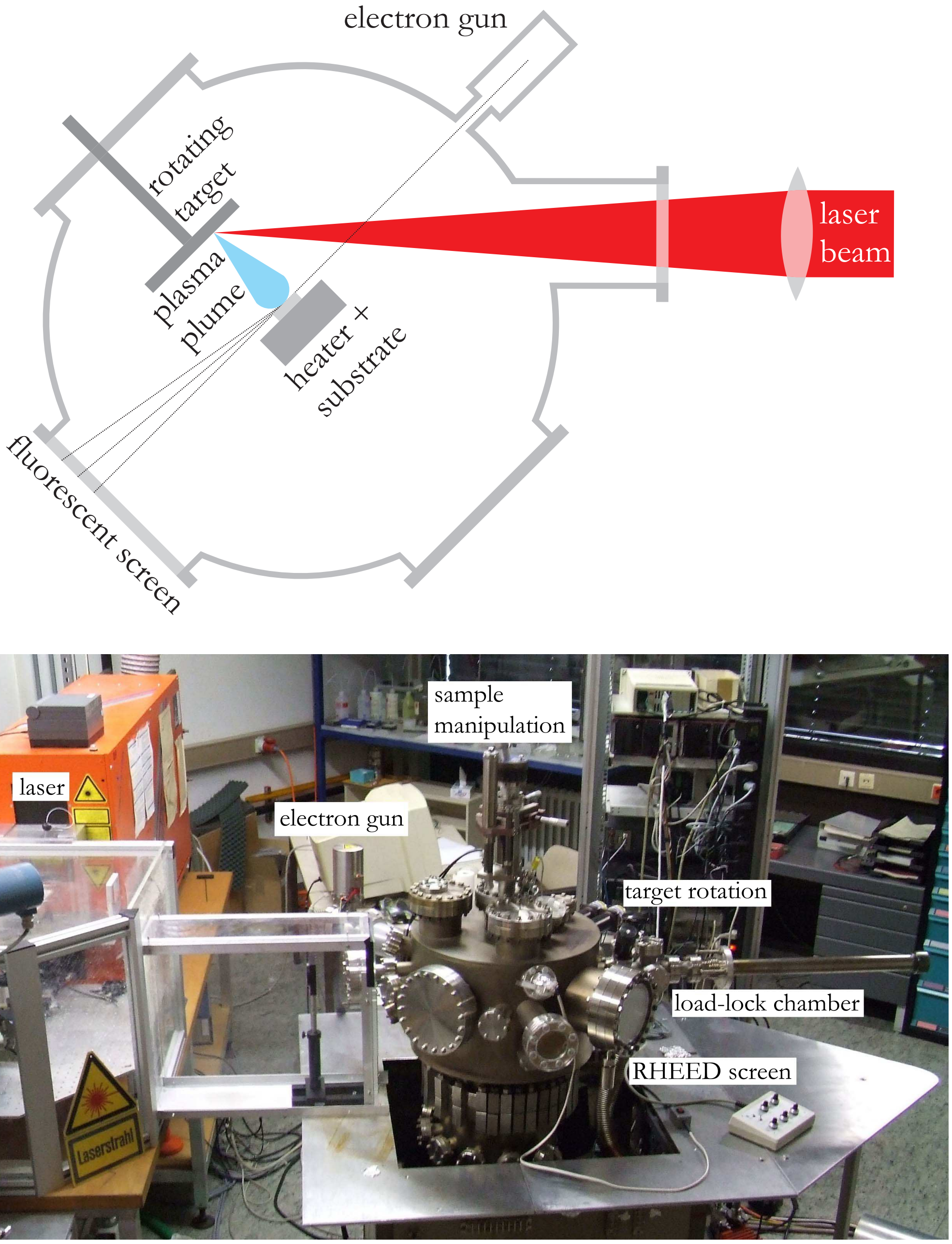

Figure 2.4: Top: Sketch of a vacuum chamber designed for pulsed laser deposition (top view). Bottom: Realization of the pulsed laser deposition system used in this work.

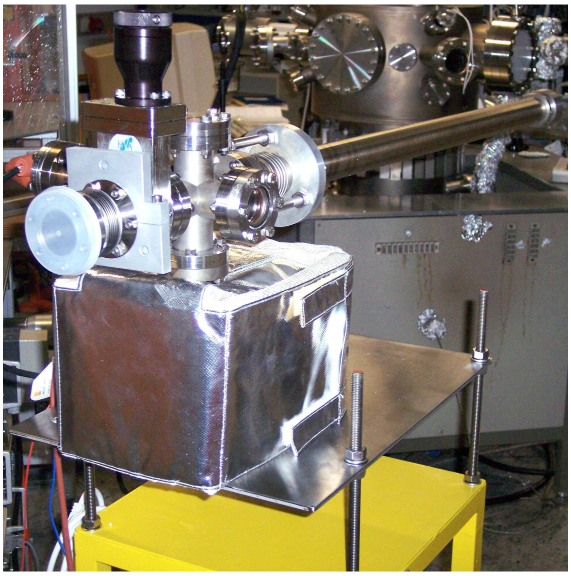

Figure 2.5: Photo of the mobile vacuum chamber. A battery powered ion getter pump allows sample transport at a pressure below 10^{-9} mbar.

Pulsed laser deposition is commonly employed for thin film preparation of oxidic materials, it was especially successful with high-T_C superconductors [120]. Its use in the deposition of metallic films is less common [121], mainly due to an excessive production of melt droplets. Nevertheless, successful epitaxial growth of Heusler films has been reported [46, 122].

For the deposition of the metallic Heusler alloys oxidation is highly undesirable. Therefore the improved ultrahigh vacuum system shown in figure 2.4 needed to be constructed at the beginning of this work. The main chamber was evacuated with an ion getter pump in conjunction with a Ti sublimator. After pumping down and baking out a base pressure between 1 and 2×10^{-10} mbar could be reached. The use of a separate load-lock chamber allowed the quick exchange of samples. Additionally the mobile vacuum system shown in figure 2.5 could be attached to the deposition chamber. It enabled the transport to external surface sensitive experiments such as photoemission spectroscopy or scanning tunneling microscopy without breaking the vacuum.

Again, targets with a diameter of 2.5 cm were cut from polycrystalline ingots. Several bulk materials were needed for thin film deposition: a buffer material, the Heusler compound and aluminum for capping. Therefore, a possibility to move different targets into the fixed laser focus was required. This was accomplished by the carousel shown in figure 2.6, which is based on the design by Clark and Weston

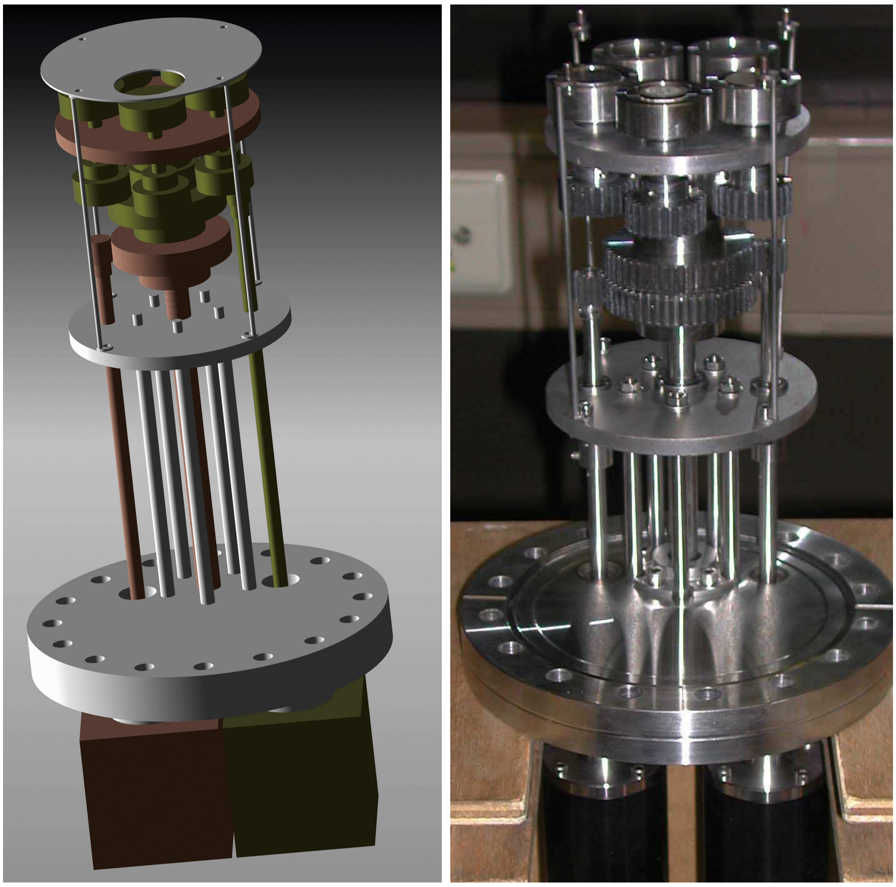

Figure 2.6: Target carousel for the pulsed laser deposition system. The different colors in the model indicate to which stepper motor the moving parts are coupled. The green motor drives the planetary gear, the brown one allows the selection of the desired target.

[123]. A planetary gear connected to a stepper motor allowed the rotation of the individual targets. In order to select the different targets a second stepper motor was used to rotate the whole disk onto which the "planets" are mounted. The two movements were decoupled by means of ball bearings. This setup not only allowed the choice of the required bulk materials. The combination of both rotations also enabled erosion of the whole target disk.

The movement of the stepper motors as well as the laser emission could be remotely controlled by a computer. This allowed the unattended change of different targets and therefore the fully automated growth of multilayer samples. More important is the fact that this introduced a high flexibility in film deposition, because the targets could now be switched as often as required without further need for manual attendance. It was therefore possible to deposit alternating sub-monolayers of Co_2FeSi and Co_2MnSi in order to create arbitrary $Co_2Mn_{1-x}Fe_xSi$ samples.

The laser pulses impact on the target with an angle of 45 ° to the surface. The rotation axis of the plasma plume is along the surface normal. Therefore, the substrates were positioned opposite the target carousel. The sample stages were transferred onto a heater block, which again could be heated resistively up to 700 °C. An electron gun and a fluorescent screen were mounted perpendicular to the substrate-target axis. This RHEED setup allowed *in situ* monitoring of the growth process (see also section 2.6 on page 31).

2.4 X-Ray Diffraction

The wavelength of X-ray light is comparable to the interatomic distances in a solid. Therefore, the analysis of diffraction patterns at these three-dimensional grids serves as the standard tool to identify crystal structures. In order to interpret the experimental diffractograms the von Laue formalism [124] was applied. Here the elastic scattering of the incident plane X-ray wave off single atoms is considered. The diffracted partial beams interfere with each other. The intensity is then found to be proportional to $e^{i\mathbf{d}_j\cdot\mathbf{K}}$ with the position $\mathbf{d}$ of the j^{th} atom in the unit cell and the difference $\mathbf{K}$ between incident and scattered wave vector. Summing over the unit cell and introducing element specific atomic form factors f_j yields a scattered intensity [124] of

$$I_{\mathbf{K}} \propto \left| \sum_{j=1}^{n} f_j(\mathbf{K}) e^{i\mathbf{K}\cdot\mathbf{d}_j} \right|^2 . \tag{2.1}$$

From the exponential factor it can be concluded that constructive interference occurs only if the change of the wave vectors $\mathbf{K}$ is a vector of the reciprocal lattice. This condition can be illustrated with the Ewald sphere construction as shown on the left hand side of figure 2.7. Since elastic scattering is assumed, incident and diffracted wave vectors both lie in a sphere of radius $|\mathbf{k}|$. Diffraction peaks will only be observed if $\mathbf{K}$ connects two points in reciprocal space lying on the sphere. An equivalent description in real space is Bragg's well-known law

$$2d\sin\theta = n\lambda. \tag{2.2}$$

It establishes a connection between the spacing d of the direct lattice planes perpendicular to $\mathbf{K}$ and the X-ray radiation with wavelength λ impacting under the angle of incidence θ.

Table 2.2: Scattered intensities of different reflections in the Heusler structure [40] as a function of the atomic form factors of the four sublattices A – D. Miller indices refer to the conventional cubic unit cell, the right column denotes the factor given by the right hand side of equation (2.1)

Reflection	Scattered intensity
(111)	$\left\|(f_A - f_C)^2 + (f_B - f_D)^2\right\|$
(200)	$\|f_A - f_B + f_C - f_D\|^2$
(220)	$\|f_A + f_B + f_C + f_D\|^2$

In order to interpret X-ray diffraction patterns of compound systems the form factors—defined as the Fourier transforms of the electron densities—of the individual elements have to be taken into account. Evaluation of equation 2.1 for the Heusler structure results in the expressions given in table 2.2 [40]. The form factors of the atoms in the Co-based Heusler compounds under investigation here are approximately $f_{\text{Co}} \approx f_{\text{Mn,Fe}} \approx 2f_{\text{Si,Al}}$ [125]. If all Miller indices of a reflection are even and if $h + k + l = 4n$ it can be seen from table 2.2 that the intensity is calculated from the sum of the individual form factors. These *principal reflections* are therefore independent of the short range ordering of the system. In the B2 case, the intermixing of the atoms on the B and the D sublattices causes a disappearance of those reflections whose Miller indices are all odd. A2 disorder will additionally extinct all-even reflections with $h + k + l = 4n + 2$. DO_3 disorder between Co and the main group element will weaken but not extinguish the scattered intensities of all save the principal reflections. Since the form factors of the transition metals are nearly identical it is not possible to explore DO_3 type disorder between Co and Fe or Mn in these samples by X-ray diffraction. In practice the exact intensity ratios for varying degrees of disorder have been calculated with PowderCell [126, 127] and compared with experimental results. This program takes into account the exact, **K**-dependent atomic form factors in order to simulate the diffractograms.

In order to vary **K** in this work the rotating crystal (or Bragg or ω–2θ) method was employed: the incident X-ray beam has a monochrome wavelength and a fixed direction. The investigated crystal and the detector are rotated to vary the angle of incidence ω and the detector position 2θ. A sketch of this experimental setup is presented in figure 2.8. In the reciprocal space picture, the tip of the incident wave vector and with it the Ewald sphere is rotated as indicated in the right hand side of figure 2.7. The X-ray sources in use emitted Cu $K_{\alpha 1}$ radiation with a wavelength of $\lambda = 1.54056$ Å. Additional contributions stemmed from $K_{\alpha 2}$, K_β as well as Mo and W impurities.

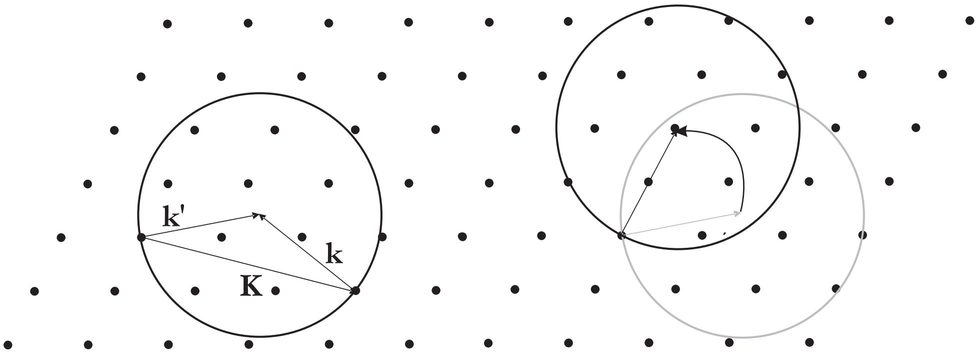

Figure 2.7: Left: The Ewald construction for a planar cut through reciprocal space. Right: Evolution of the Ewald sphere in a rotating crystal experiment.

In the ω-scan ("rocking curve") mode of operation 2θ is kept fixed on a lattice reflection and ω varied. In a perfect crystal a signal is obtained only if $\omega = \theta$. The variation of ω for a polycrystalline sample with a certain mosaic spread of the individual crystals will result in a Gaussian broadening of the intensity distribution around the maximum.

Two different machines were used in the characterization process. The fist one was a two circle diffractometer, which only allows the rotation along ω and 2θ, χ is kept fixed at 0 °. This method allows the fast access of the crystal planes parallel to the film surface. It can therefore be used to investigate the layer-by-layer crystal growth of the film on the substrate. If the obtained diffractograms showed a high quality, further studies of the crystal structure were carried out with a four-circle diffractometer. It allows the variation of all angles and therefore the access to arbitrary lattice planes.

2.5 X-Ray Reflectometry

In addition to structural analysis, X-rays can also be used to determine film thickness. This is achieved by examining reflection under glancing incidence. Below the critical angle θ_C of the topmost layer, total reflection of the incident light is observed. If θ_C is exceeded, a portion of the radiation may permeate the sample and will be reflected at the next interfaces. Interference of these partial beams results in the so-called Laue intensity oscillations. In the simplest approximation, their characteristics can be described with Bragg's law. In order to obtain a more precise picture, the different indices of refraction have to be taken into account [128, 129]. They determine θ_C, the decrease in intensity for $\theta > \theta_C$, and deviations in the Laue os-

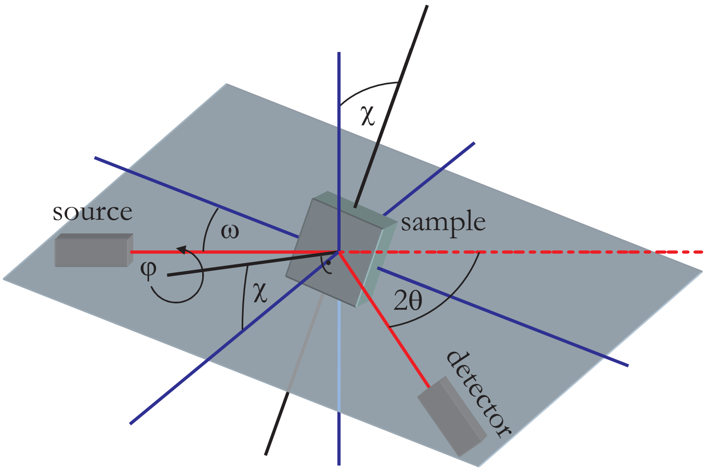

Figure 2.8: Geometry of a rotating crystal X-ray diffraction experiment. Please note that conventionally the angle of incidence is denoted with ω and the detection angle with 2θ (instead of 2ω) because they can be varied independently.

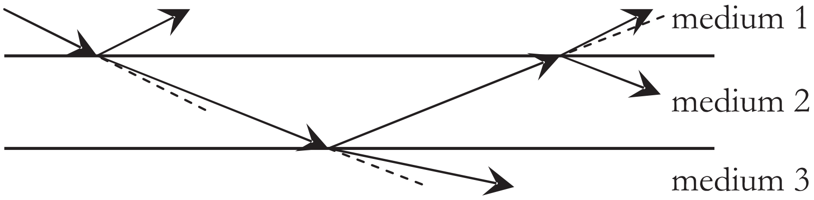

Figure 2.9: Optical path in an X-ray reflectometry experiment. The dashed lines indicate the progress without refraction.

cillations from Bragg's law. The last point is caused by a change of the optical path as shown in figure 2.9.[1] Finally, the interface roughness, which will cause a peak broadening, has to be considered. Model calculations accounting for these parameters were performed with PARRATT32 [129, 130] and compared with experimental data.

2.6 Electron Diffraction

In reflection high-energy electron diffraction (RHEED), electrons instead of electromagnetic waves are used to probe the crystal structure[107]. They are accelerated to energies of typically 10 – 20 keV and impinge the sample nearly parallel to its

---

[1] This deviation is also present in diffraction experiments, but it can be neglected for $\theta \gg \theta_C$.

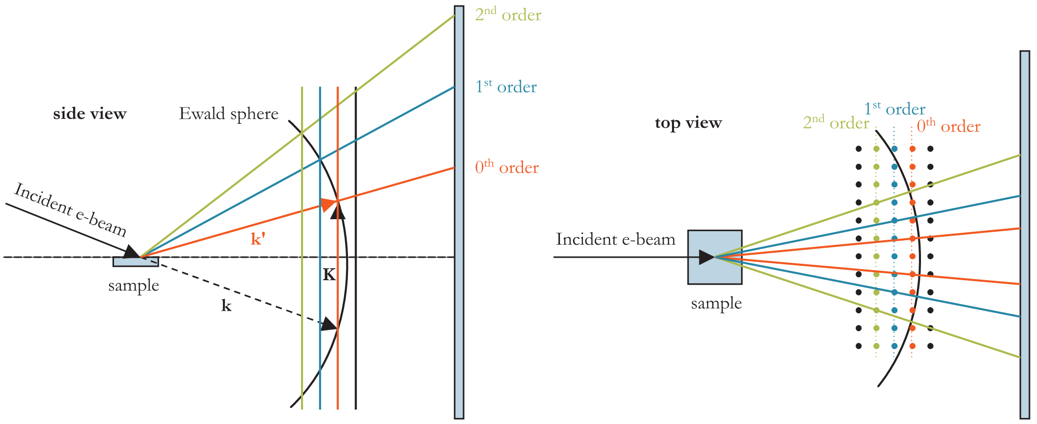

Figure 2.10: Ewald sphere construction for a RHEED experiment.

surface. This flat angle of incidence results in a very small **k** component normal to the surface. Therefore, these electrons probe only a few atomic layers below the surface [131] and the sample can be approximated by a two-dimensional crystal. The points in reciprocal space degenerate into one-dimensional rods, which is sketched in figure 2.10. The intersection of the Ewald sphere with these rods causes a nonvanishing diffracted contribution, which is detected with a fluorescent screen. It can be seen from the illustration that one obtains several orders of reflections, which are arranged as concentric rings on the screen. Since the Ewald sphere is almost flat ($k = 785\ \mathrm{nm}^{-1}$ for 20 keV) compared with the reciprocal lattice ($\approx 1\ \mathrm{nm}^{-1}$), the intersections of the extended reciprocal rods with the Ewald sphere become streaks instead of points.

Although not evaluated quantitatively in this work, RHEED played an important role in sample characterization. The existence of a diffraction pattern indicates good crystalline quality of the sample, whereas an overall diffuse signal is the result of a disordered surface. RHEED is an *in situ* technique, and the alignment of the beams parallel to the sample surface allows monitoring of the crystal growth during deposition. For the deposition of Heusler compounds this is very beneficial, because it allows examining the surface quality of substrate and buffer layer directly before film deposition.

A second method of surface sensitive electron diffraction can be attained if a beam of low energetic ($E \lesssim 150$ eV) electrons is directed normal to the surface. The probing depth of this setup is comparable to RHEED, so again diffraction off a two-dimensional grating has to be considered. In such low energy electron diffraction (LEED) experiments [132], backscattered electrons are registered on a fluorescent screen. This setup prohibits real-time monitoring of the growth processes, because electron source and detector need to be placed opposite of the sample surface. The main difference to RHEED stems from the fact that now Ewald sphere and reciprocal space have comparable dimensions. Only a few diffracted beams appear and the reflections are no longer line- but point-like.

2.7 Bulk Magnetometry

For the detection of the magnetic properties two techniques were used which both exploit the electromagnetic induction caused by a movement of a magnetized sample. In order to eliminate contributions from external magnetic field the sensing coils are formed as gradiometers. In a vibrating sample magnetometer (VSM) [133] the sample is driven with a vibration of constant frequency. This results in an oscillating magnetic flux through the sensing coils. Since the induced voltage alternates with the same frequency as the driver, the induction voltage can be measured with a lock-in technique. The magnitude of this signal is proportional to the magnetic moment of the sample. It is also dependent on the frequency of the vibration. However, it is not possible to increase arbitrarily, because of parasitic vibrations in the setup. The low-frequency regime is limited by the sensitivity of the voltage measurement. For an optimized frequency the root mean square noise floor of the system in use was 1.5×10^{-9} Am^2.

The second machine in use was a SQUID magnetometer [134, 135]. In principle, it can be considered as a low frequency VSM, as the sample is moved linearly through the pickup coils. The induced current is converted into measurable voltage signals by one or more superconducting quantum interference devices, which exploit the Josephson effect in a superconducting loop [136]. Additional sensitivity is gained if the linear sample transport is replaced with a low-frequency sinusoidal movement, which reduces thermal noise. For the latter case, the sensitivity of the SQUID magnetometer used in this work was one order of magnitude better than the VSM. The downside of this second method is that it is vastly slower in hysteresis measurements. Since the sensitivity of the VSM is already well below the expected signals from the Heusler compounds, it was used as the standard tool.

Both VSM and SQUID experiments were located within variable temperature insets (VTIs) of liquid helium cryostats. This enabled the controlled variation of the sample temperature between 2 K and room temperature. The magnetometry setups were primarily used to measure hysteresis loops at constant temperatures. The films were mounted with the surface parallel to the external field, which allowed the determination of the saturation and remanent magnetization as well as the coercitive field. Rotation of the sample along the film normal was used to estimate the angular dependence of the in-plane magnetocrystalline anisotropy. The last technique was limited by the lack of a precise method of alignment or rotation. Finally, the temperature dependence of the magnetization at a fixed external field could be investigated.

Before interpreting the measured data, it has to be kept in mind that the underlying substrates and buffer layers give additional contributions, which first need to be subtracted. Furthermore, the shape of the samples is an important factor in quantitative analysis. The machines had been calibrated with spherical bulk samples. Such references have an isotropic demagnetization field and the stray field has the same form as an ideal magnetic dipole [137]. The thin film geometries have a vastly different form, which are expected contribute to a systematic error of up to 20 %. The machines therefore had to be recalibrated with plate-like references.

2.8 Transmission Electron Microscopy

As in RHEED, a transmission electron microscope (TEM) makes use of the wave character of the electron [138]. The limiting factor for TEM resolution is not the electron wavelength—the model in use has an accelerating voltage of 300 kV, which corresponds to $\lambda = 2$ pm—but the quality of the electron optics. Nevertheless, information on the atomic scale can be obtained. As its name implies, most information is gathered from electrons passing through a very thin specimen. The interaction of the incident electron with sample matter causes in the transmitted beam a variation in intensity as well as angular distribution. The former effect is used for imaging the spatial distribution of the atoms, the latter allows the recording of diffraction patterns.

2.9 Nuclear Magnetic Resonance

The concept of nuclear magnetic resonance (NMR) spectroscopy is based on the magnetic properties of the nuclei [139]. The nuclear magnetic dipole moment is given by $\mu = \hbar \gamma I$, with the isotope specific gyromagnetic moment γ and the nuclear spin quantum number I. If an external magnetic field $\mathbf{B}_0$ is present the $2I + 1$ fold energy degeneracy will be lifted by Zeeman splitting and the spins will precess around the field direction. The energy splitting is probed in most cases by applying a radio frequency field perpendicular to $\mathbf{B}_0$.

In solids in thermal equilibrium the ensemble of nuclear moments creates a net magnetization along the $\mathbf{B}_0$ direction. After applying a $\pi/2$ pulse this magnetization precesses freely in the plane perpendicular to $\mathbf{B}_0$, which can be measured with an inductive pickup coil. In ferromagnetically ordered samples the local field of a nucleus is dominated by the hyperfine field $\mathbf{B}_{\mathrm{hf}}$ [140]. It describes the interaction of the nuclear magnetic moment with the spin and orbital magnetic moments of the surrounding electrons. The main contribution in transition metals is caused by a hybridization of d electrons from the nearest neighbor atoms with on site s orbitals. This is the source of a finite spin polarization at the nucleus. Therefore, NMR is well suited to investigate atomic ordering in ferromagnets: a change of the nearest neighbor configuration changes the spin polarization and will therefore alter the investigated hyperfine field.

2.10 Morphology

In scanning electron microscopy (SEM) electrons are accelerated to energies of several hundred eV and focused on a spot of down to 1 nm. Being detected are low-energy secondary electrons generated by inelastic processes. The emission characteristic is symmetric around the surface normal, so intensity variations can be used to create a plastic image of the surface. The parallel incident beam and the nature of the secondary electrons allow for images with a very high depth of field. The SEM electron source could also be used for energy dispersive (EDX) spectroscopy. Here the electrons are accelerated to 20 keV and used to ionize the material. The resulting characteristic radiation can be used to determine the film stoichiometry.

Atomic Force Microscopy (AFM) maps the sample morphology by investigating the forces between a probing tip and the surface atoms. In noncontact operation, a cantilever is driven into oscillations. If the tip approaches the surface, the amplitude will change. In contact mode, the bending of the cantilever is directly observed. This allows in principle for atomic resolution, put in reality it is limited by mechanical distortions.

CHAPTER 3

HEUSLER THIN FILMS

In the first two chapters it has been exposed what is considered a “high quality” Heusler compound and how one can expect to create thin films possessing the desired properties. As a consequence from these discussions, the main focus of film growth was a reproducible, well-defined growth of epitaxial thin films with a high degree of $L2_1$ order and a magnetic moment compatible with the Slater-Pauling rule. Furthermore, the effects of the substrate on the film needed to be minimized. Strained growth or impurities had to be avoided. This chapter now details the execution of the sample preparation process. It will be shown how the different deposition techniques and a systematic variation of the other growth parameters affect the film properties of interest.

3.1 Sputter Deposition of $Co_2Cr_{0.6}Fe_{0.4}Al$

With the sputter deposition system described in section 2.2 it had been possible to grow epitaxial thin films of $Co_2Cr_{0.6}Fe_{0.4}Al$ on heated $(11\bar{2}0)$-cut Al_2O_3 substrates prior to this work [65]. However, although the long-range crystallographic quality of such films was excellent, the $\{111\}$ and $\{311\}$ superstructure reflections could not be found. Additionally, the magnetization value of 2.5 μ_B/f. u. was drastically reduced compared with 3.8 μ_B/f. u. expected from the Slater-Pauling rule [61] and with bulk samples, for which a value of 3.5 μ_B/f. u. was reported [55]. This hints toward a significant amount of A2 disorder in these samples [52]. Similar results had been published for $Co_2Cr_{0.6}Fe_{0.4}Al$ films deposited on MgO (100) substrates [105].

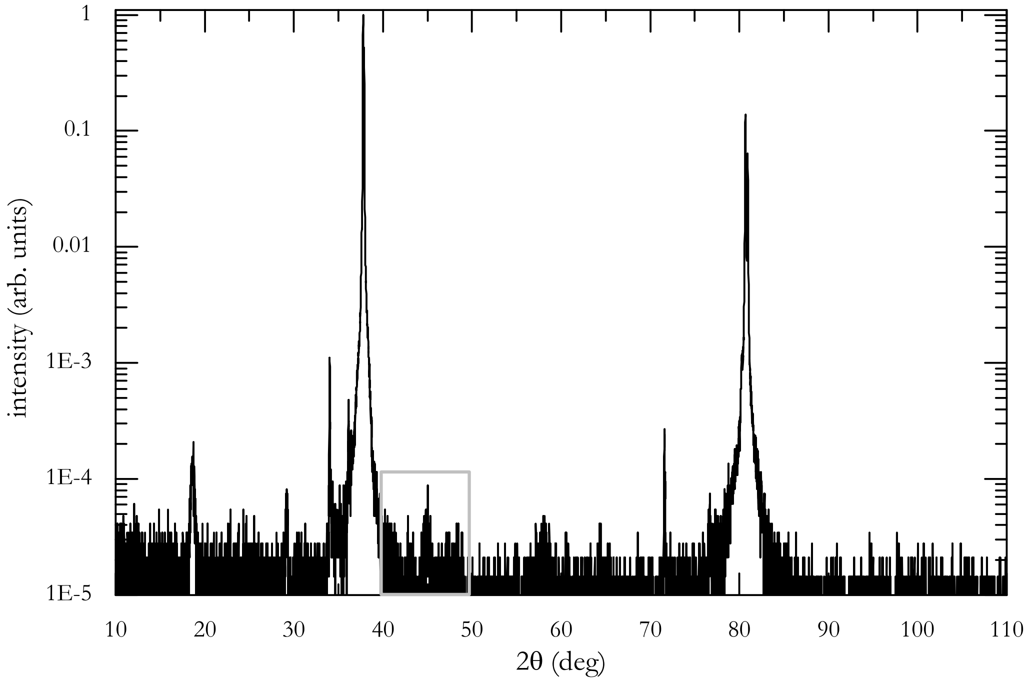

Figure 3.1: ω–2θ scan of a $Co_2Cr_{0.6}Fe_{0.4}Al$ film deposited on Al_2O_3 at room temperature. The (220) film reflection is expected to be located at 44.6 °. The frame indicates the region shown in figure 3.2

As a first attempt to improve film quality the liquid nitrogen cold trap and titanium getter system as described in section 2.2 were fitted to the recipient. The resulting pressure decrease at both low and high temperatures of roughly one order of magnitude yielded a more reliable deposition process. Prior to this installation, the $Co_2Cr_{0.6}Fe_{0.4}Al$ films showed signs of surface oxidation [111]. For samples deposited during this work, XMCD experiments did not detect oxygen [141]. However, neither diffraction nor magnetometry showed improved sample quality. It seems therefore that oxidation is confined only to a small fraction of the films.

In order to overcome these problems, an approach first reported for Heusler thin films by Kämmerer *et al.* was employed [32]. The films were deposited at room temperature, structural and magnetic properties were improved by a post-annealing step. For the needs of $Co_2Cr_{0.6}Fe_{0.4}Al$ thin film deposition, the Al_2O_3 and MgO substrates were first vacuum-annealed, as explained in section 2.1. After cooling down to ambient temperature, first the Heusler material and afterward an Al cap layer were deposited. As a final preparation step, the films were heated in vacuum for one hour at a fixed temperature.

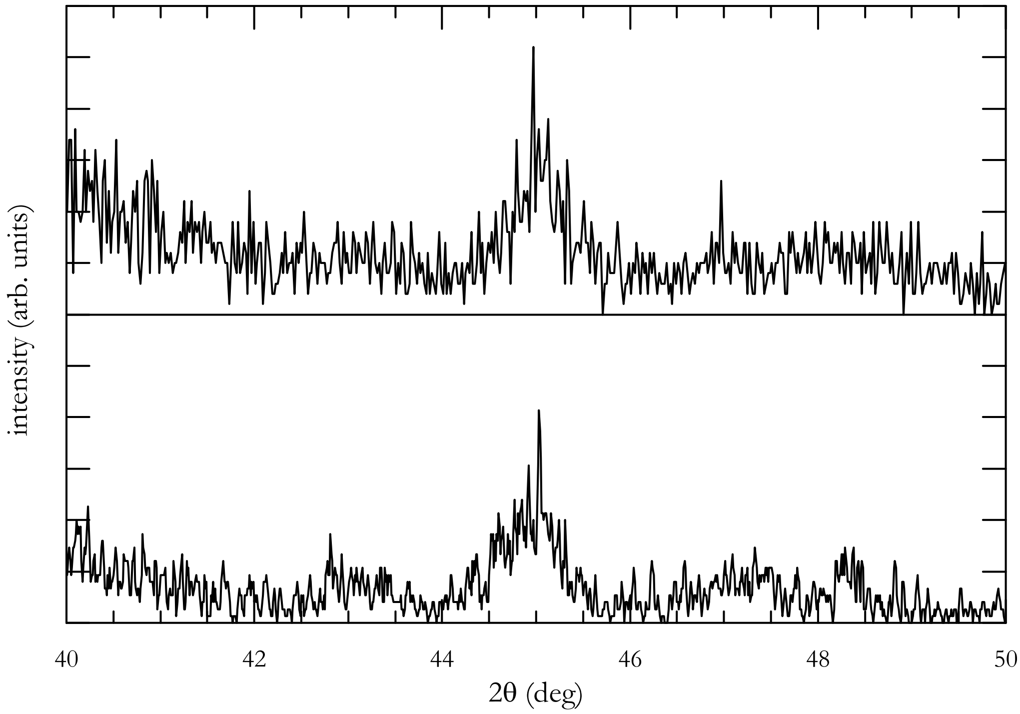

Figure 3.2: Area of interest from figure 3.1 of the $Co_2Cr_{0.6}Fe_{0.4}Al$ film after deposition at room temperature (bottom) and after annealing for 1 h at 400 °C (top).

Figure 3.1 shows an example of a Bragg scan of a $Co_2Cr_{0.6}Fe_{0.4}Al$ / Al_2O_3 film after deposition at room temperature; the results for $Co_2Cr_{0.6}Fe_{0.4}Al$ / MgO samples are similar. It can be seen that at the expected position of the (220) reflection at $2\theta = 44.6$ ° hardly any scattered intensity is recorded. All other peaks visible in this diffractogram are substrate reflections. This is consistent with earlier findings [65]. To examine the effect of the annealing process, a magnified view of figure 3.1 is shown at the bottom half of figure 3.2. A scan of the same sample after one hour of annealing at 400 °C is shown at the top. It is obvious that this procedure does not improve the long-range crystal quality. In contrast, the thermal treatment seriously alters sample magnetization (see figure 3.3). The maximum values were obtained after annealing at temperatures of 300 to 400 °C. Here the magnetization clearly exceeds the values obtained for epitaxial films grown at high substrate temperature. It can also be seen that the temperature dependence of the magnetization is much less pronounced for these optimized annealing conditions.

This discrepancy between magnetic and structural properties can be resolved by transmission electron microscopy. The diffraction pattern of a film deposited

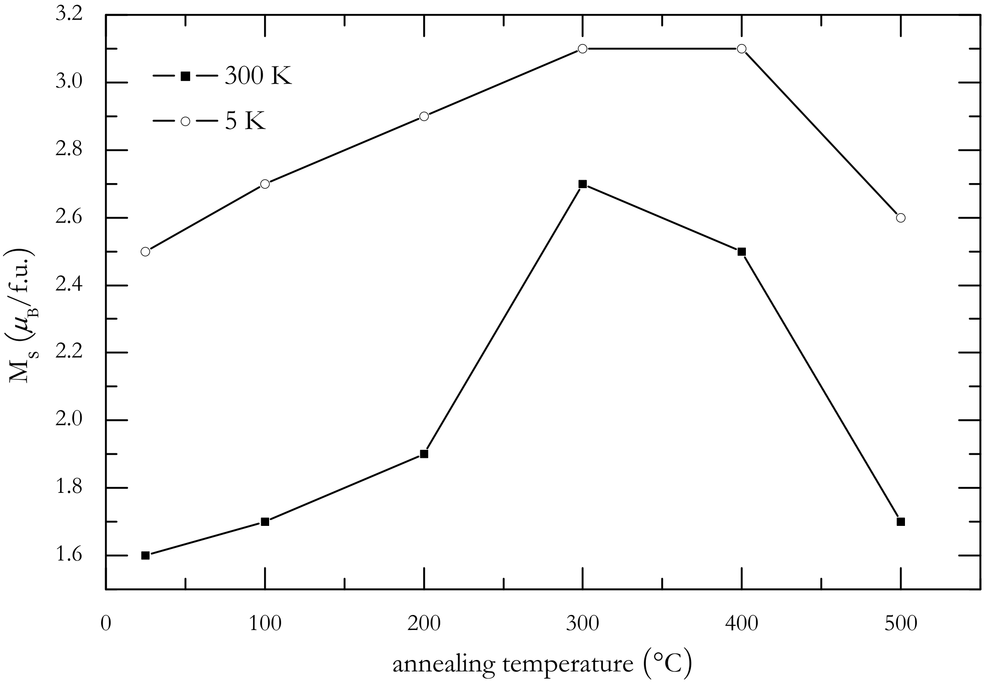

Figure 3.3: Dependence of the saturation magnetization (measured at room temperature and at 5 K) on annealing temperature. This plot shows the data for a single film, which was deposited at room temperature on Al_2O_3 and then annealed at subsequently higher temperatures for one hour each.

at room temperature is shown in figure 3.4. The occurrence of diffraction rings shows that this film is not completely amorphous but consists of randomly oriented crystallites. Their size is too small to be resolved by X-ray diffraction. It is therefore possible that the annealing process causes an increase of the short-range ordering within these nanocrystallites. On the other hand, it does not induce coalescence of the crystallites and the long-range order remains low. The drop of the magnetization at higher temperatures probably originates from interdiffusion between Al cap and Heusler film as well as the formation of paramagnetic CoAl clusters [143].

As noted in section 2.1, the non-epitaxial growth at room temperature is likely a result of the differences in crystal structure of substrate and film. Therefore it was attempted to deposit a metallic buffer layer before film growth. However, neither on Al_2O_3 nor on MgO it was possible to grow epitaxial Fe or Cr layers, even though successful sputter deposition on MgO has been reported [76]. The most plausible reason for this failure is the high base pressure of the deposition system. From classical kinetic gas theory [144] it can be estimated that at 5×10^{-8} mbar it takes

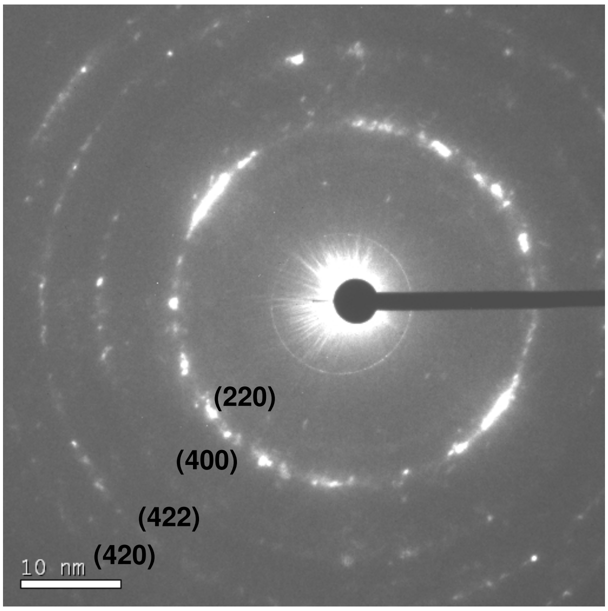

Figure 3.4: Transmission electron diffraction pattern of a $Co_2Cr_{0.6}Fe_{0.4}Al$ / Al_2O_3 film deposited at room temperature [142].

30 seconds until the substrate surface is covered with a monolayer of residual gas atoms. The heater in use needed approximately 2 hours to cool down from the initial cleaning process. Therefore, it is to be assumed that at the beginning of the deposition process at room temperature no longer a well-ordered surface is present.

3.2 Sputter Deposition of Co_2FeSi

Co_2FeSi thin film deposition by DC magnetron sputtering turned out to be more problematic than for $Co_2Cr_{0.6}Fe_{0.4}Al$. Instead of a clearly defined plasma ring, only a diffuse cloud was visible. The cause of this problem seems to be the higher saturation magnetization of Co_2FeSi, which prevents the magnetron field from penetrating the target. The results were a low deposition rate and a poor structural quality compared with $Co_2Cr_{0.6}Fe_{0.4}Al$ films grown under similar conditions. To overcome this issue, sputter deposition was carried out with an RF power supply. The first attempts in film growth were again carried out with heated Al_2O_3 $(11\bar{2}0)$ and MgO (100) substrates.

Co_2FeSi films RF sputter deposited on the former substrate show (110) oriented growth, as evidenced in the Bragg scan shown in figure 3.5. The (220) and (440) film

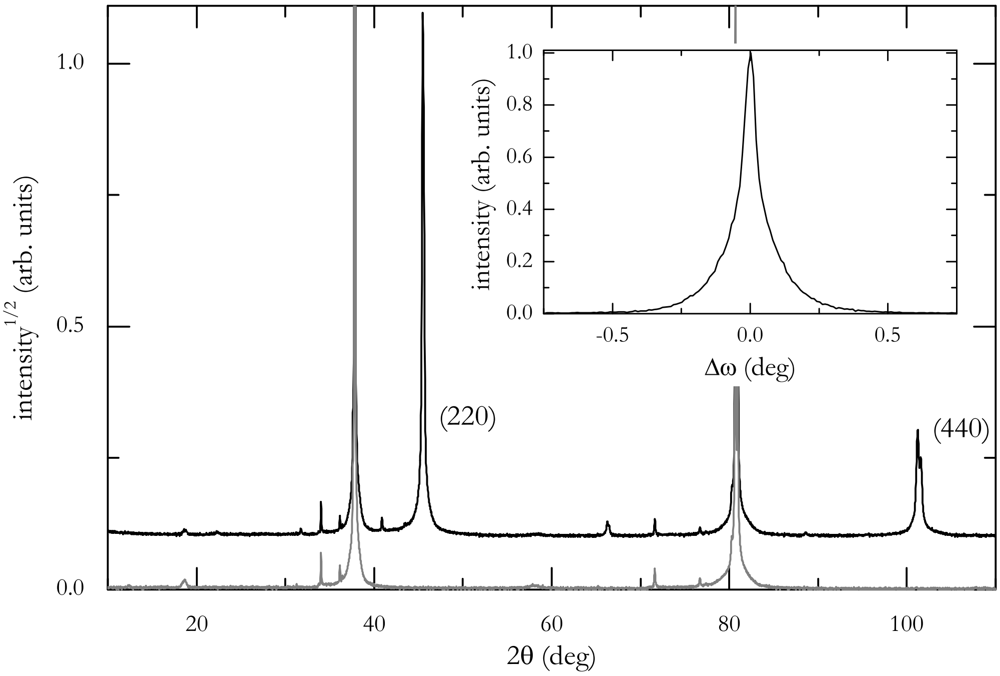

Figure 3.5: ω-2θ scan of an uncoated Al_2O_3 substrate (gray) and of a sputter deposited Co_2FeSi / Al_2O_3 sample (black). The two curves are shifted vertically for better visibility. The inset shows an ω scan of the (220) film reflection. Film thickness is 100 nm, deposition was carried out at a substrate temperature of 700 °C.

reflections have a very high intensity and a small width. The double peak structure of the (440) signal is a consequence of the Cu K_α hyperfine splitting. Two small peaks in addition to the distinct film reflections can be observed. The first contribution at 40.9 ° is caused by a small Cu K_β impurity of the incident X-ray beam. The second reflection is located at 66.5 ° and corresponds to the (400) plane of Co_2FeSi. Comparing the integrated intensities of the (220) and the (400) signal with the calculated values reveals that less than 0.5 % of the film show this deviant orientation.

The ω scan of the (220) peak shown in the inset of figure 3.5 can be represented as the sum of a Lorentzian and a Gaussian contribution. The former line is caused by resonant diffraction from ordered areas of the samples. It has a FWHM of 0.05 °, which is comparable to the instrumental resolution. The Gaussian contribution originates from a random tilting of other parts of the sample. It has a FWHM of 0.2 °, which is a significantly better value compared with reports for similar Heusler films [65, 105, 145]. All these characteristics observed so far signify an extremely well ordered layer-by-layer growth on Al_2O_3. Further information from

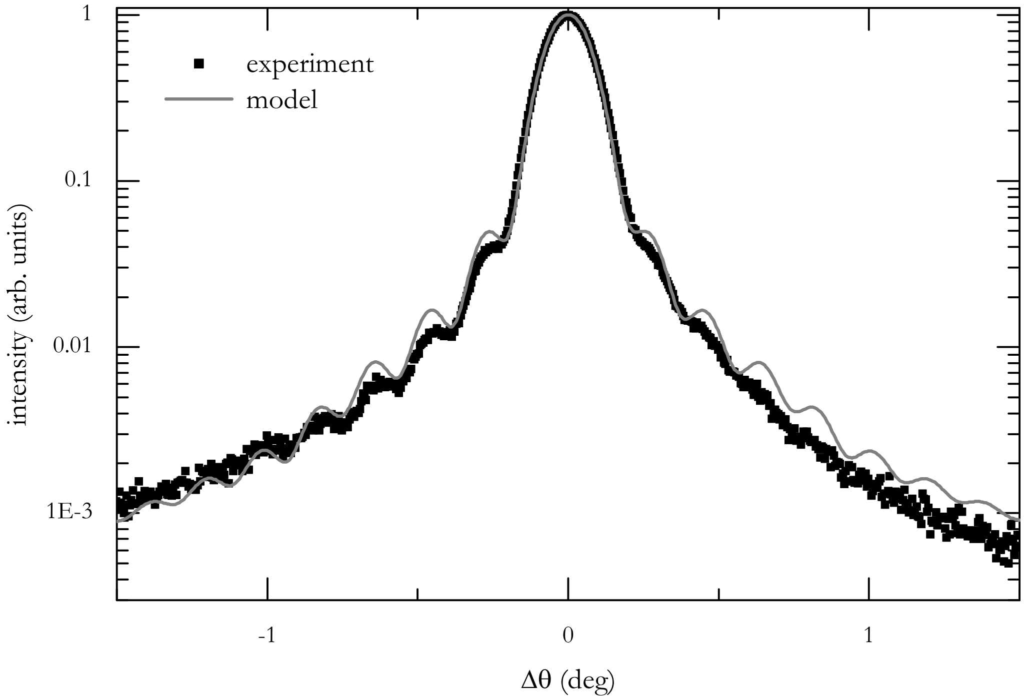

Figure 3.6: Bragg scan of the (220) reflection of a Co_2FeSi film. For the model curve a film thickness of 24 nm, a resolution in 2θ of 0.05 °, and an RMS roughness of 1 nm was assumed.

these diffractograms can be acquired if the shape of the film reflections is analyzed in more detail.

The intensity distribution in the vicinity of a Bragg reflection can be modeled analogous to the interference of light at an optical grating [144, 146]. The intensity I scattered from a film with finite thickness, consisting of N lattice planes spaced at intervals of d can then be described as

$$I \propto \left(\frac{\sin N\Delta\varphi/2}{\sin\Delta\varphi/2}\right)^2, \quad \Delta\varphi = 2\left|\mathbf{k}\right| d\cos\theta_{\text{Bragg}}\sin\Delta\theta. \tag{3.1}$$

The width of the central maximum can be approximated with the Scherrer formula

$$t \approx \frac{0.9\lambda}{\Delta(2\theta)\cos\theta}, \tag{3.2}$$

which establishes a correlation between the size t of an arbitrarily shaped particle and the FWHM $\Delta(2\theta)$ of a Bragg reflection located at angle θ [146, 147].

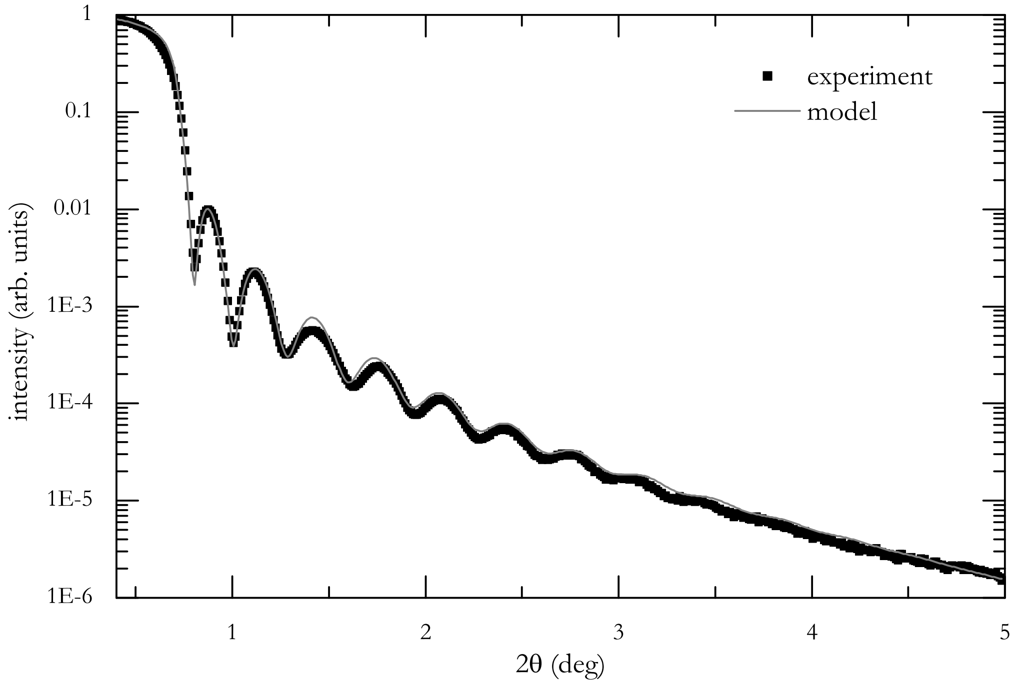

Figure 3.7: X-ray reflectivity of the Co_2FeSi / Al_2O_3 sample presented in figure 3.6. The model calculation was performed with the same parameters as before.

For a quantitative analysis with equation (3.2), the diffractometer resolution was estimated from the peak broadening of the substrate signals. Here it was assumed that the substrate is a perfect single crystal and hence that the peak width is only caused by the finite instrumental resolution. This contribution was then subtracted from the experimental width of the signal. For the film presented in figure 3.5 X-ray reflectometry yields a thickness of 100 nm. Equation (3.2) estimates a crystallite size of 92 nm perpendicular to the surface. This signifies that the film consists of a single crystallographic domain over the complete film thickness.

For films with a thickness of less than 40 nm additional satellites appear in the vicinity of the film reflections, as shown in figure 3.6. This behavior can be reproduced very well with the exact finite size formulation of equation (3.1). For this example the best agreement between experimental data and model was found for a film thickness of 24 nm. This value can be confirmed with X-ray reflectometry—the corresponding data for the same sample is shown in figure 3.7. Furthermore, the Scherrer equation gives an approximate value of 30 nm. In thick films, these finite size oscillations could not be observed. Their intensity drops more rapidly and their peak distance falls below the resolution limit of the diffractometer. Their presence

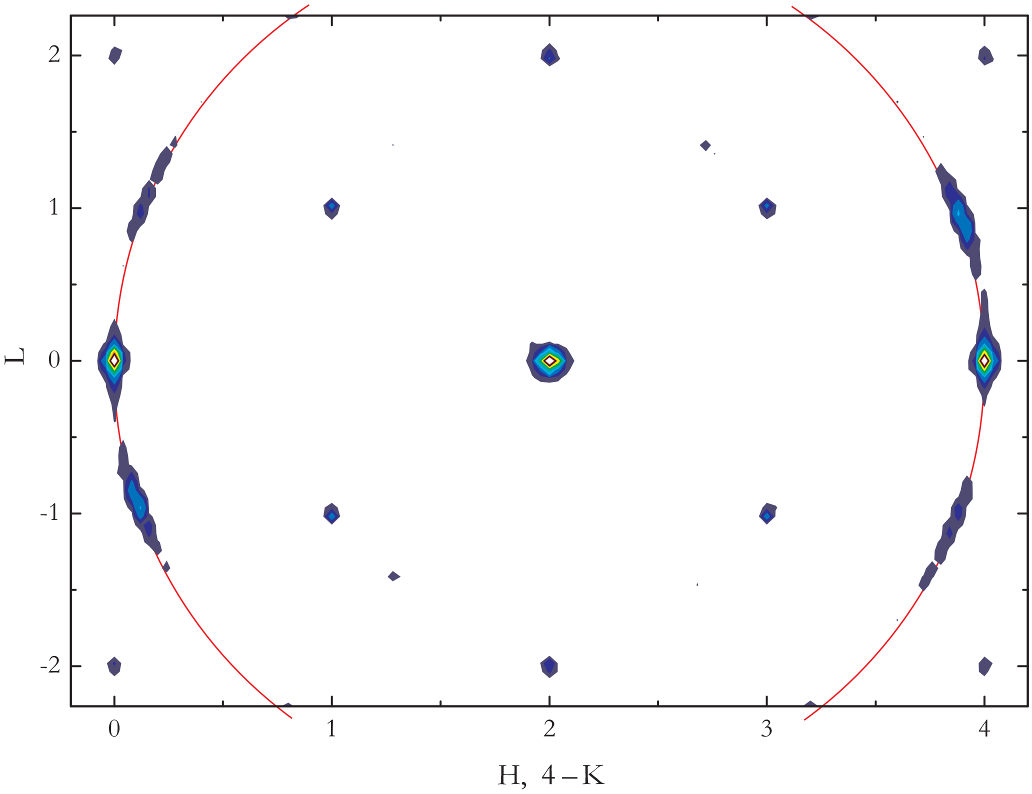

Figure 3.8: Scan of a plane in reciprocal space perpendicular to the specular (220) reflection of a Co_2FeSi / Al_2O_3 film. For better visibility, a constant background has been subtracted. The color scale indicates the square root of the measured intensity, the red circle shows the evolution of the φ-scan in figure 3.9.

again indicates a high quality out of plane growth. Additionally, it signifies a flat surface morphology, because otherwise the broadening of the side maxima will disable their observation.

Compared with the stacking of individual layers, in-plane growth is considerably less well ordered. This is illustrated in figure 3.8. The specular (220) reflection in the center is well defined and has a high peak intensity, as expected from the previous investigations. For the in-plane reflections, it can be seen that the scattered intensity is not confined to points in reciprocal space. Instead, the reflections tend to form concentric circles. The radial intensity distribution is reasonably well defined also in this case. This circular intensity distribution can readily translated into real space. It occurs if φ is varied and the other angles are fixed. Figure 3.9 shows a φ scan of the same sample along the circle in reciprocal indicated in figure 3.8. It can be seen

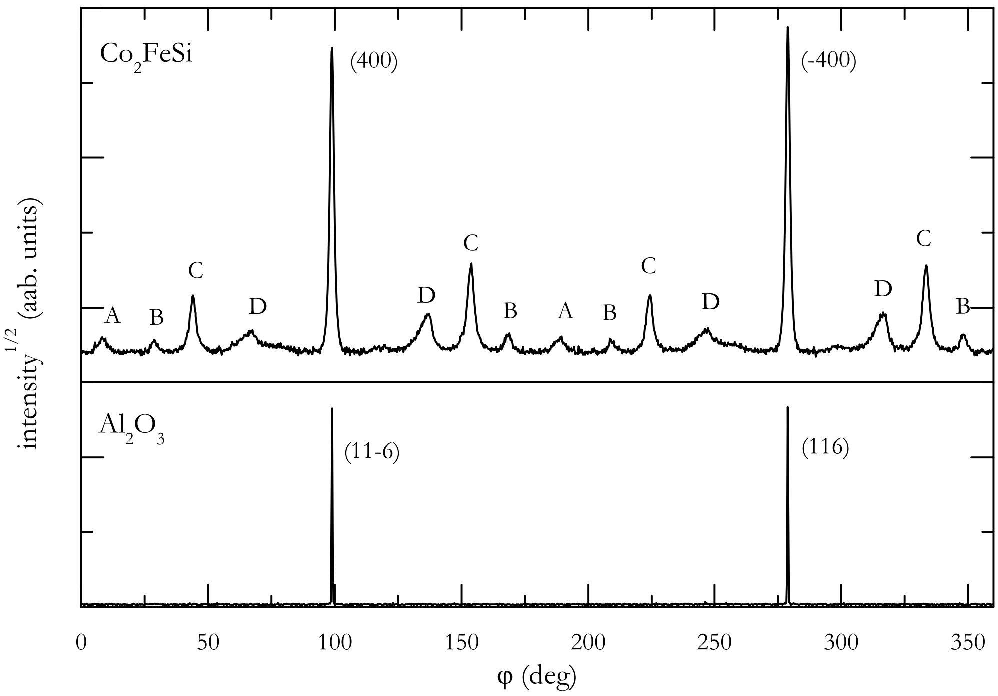

Figure 3.9: φ-scans of a sapphire substrate and the Co_2FeSi film deposited on top. The most intense film reflections have been labeled (400) and ($\bar{4}00$). A – D mark equivalent secondary peaks.

that the scattered intensity is distributed over several domains. The reflections with the highest intensities have been assigned (400) and (040).

A comparative scan of the underlying substrate (shown in the lower part of figure 3.9) reveals that the ($1\bar{1}0$) planes of the film are parallel to the (0001) planes of the substrate. At first glance, this is somewhat surprising. As shown in the upper left part of figure 3.10 the lattice constants at the interface differ by a large amount in both directions. One would rather expect that the film grows rotated by 90 °. As illustrated in figure 3.10, the crystal structure at least along the [$1\bar{1}0$] film direction fits very well to the substrate surface. But contrary to this simple picture, only a small fraction of the film grows in that orientation, which causes the additional reflections marked with A in figure 3.9.

In order to understand this discrepancy, a more detailed comparison of the position of film and substrate atoms is required. In this case it can be noticed that film atoms tend to be located on top of oxygen substrate atoms for the favored orientation $(1\bar{1}0)_{\mathrm{film}}||(0001)_{\mathrm{substrate}}$. Such behavior is much less pronounced for the A

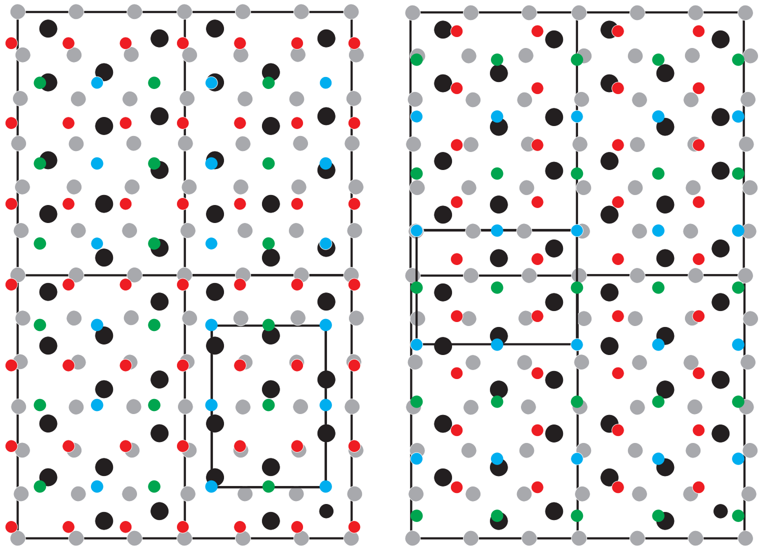

$(400):(1\bar{1}0)_{\mathrm{film}}||(0001)_{\mathrm{substrate}}$ A: film rotated by 90 °

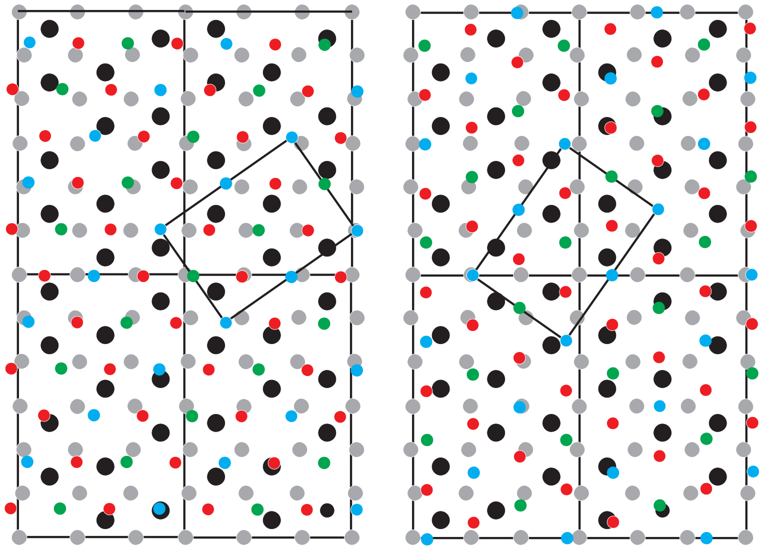

C: film rotated by 55 ° D: film rotated by 35 °

Figure 3.10: Projection of Co_2FeSi (110) on Al_2O_3 $(11\bar{2}0)$. Black discs represent Al, gray discs O atoms. Co atoms are colored blue, Fe and Si are red and green, respectively. Black lines show the contours of the unit cells. The lettering below the images corresponds to the labels in figure 3.9.

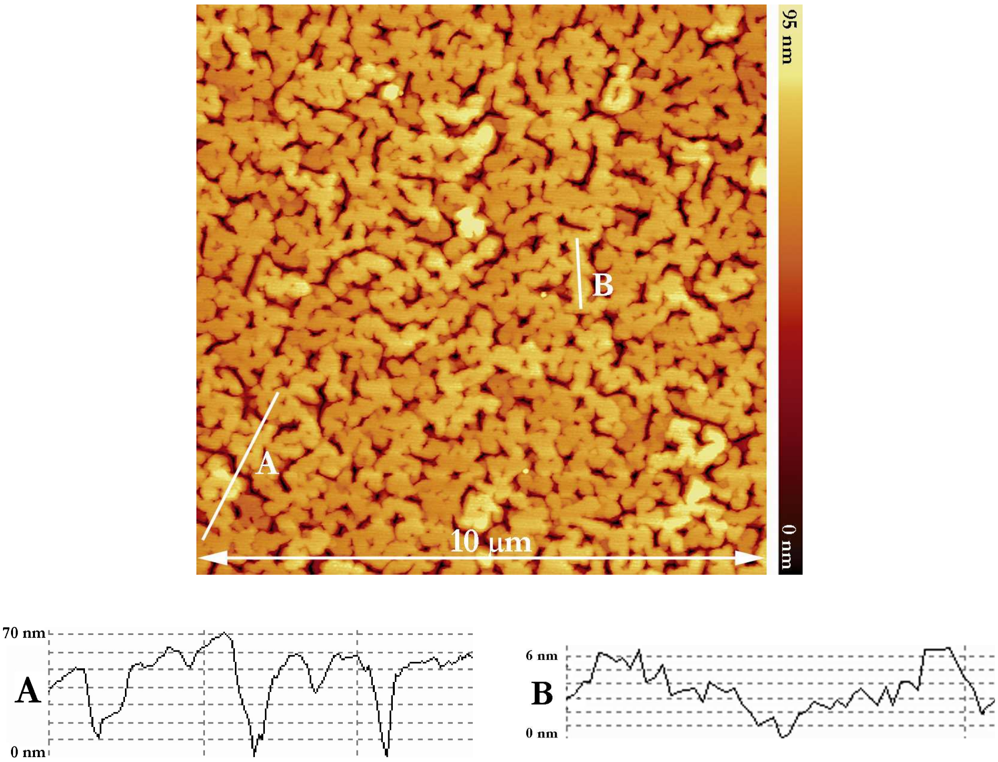

Figure 3.11: Top: AFM image of the surface of a Co_2FeSi / Al_2O_3 (100 nm) sample. Bottom: Depth profiles along the lines indicated above.

alignment. It seems therefore that the energy gain due to these metal-oxygen bonds outweighs the increased stress imposed on the film due to the larger lattice mismatch. The appearance of further reflection families marked with B – D is also connected to similar atom matching. The integrated contribution of the secondary reflections accounts for typically 10 – 15 % of the total intensity, depending on the deposition parameters. Despite the non-perfect growth, it is therefore possible to measure orientation dependent properties.

Summing up the crystallographic properties so far, an extreme case of island film growth seems to be present. Layer-by-layer growth of Co_2FeSi on Al_2O_3 is nearly perfect. On the other hand, the very large differences in the crystal structure of film and substrates stimulate several epitaxial in-plane domains. This assumption is supported by the surface morphology of these samples. It can bee seen in the AFM images shown in figure 3.11 that the overall flat film surface (line B) is pervaded by deep trenches (line A). It may be possible in this scenario that large crystallites of different orientation can coexist without forming a common interface. It should

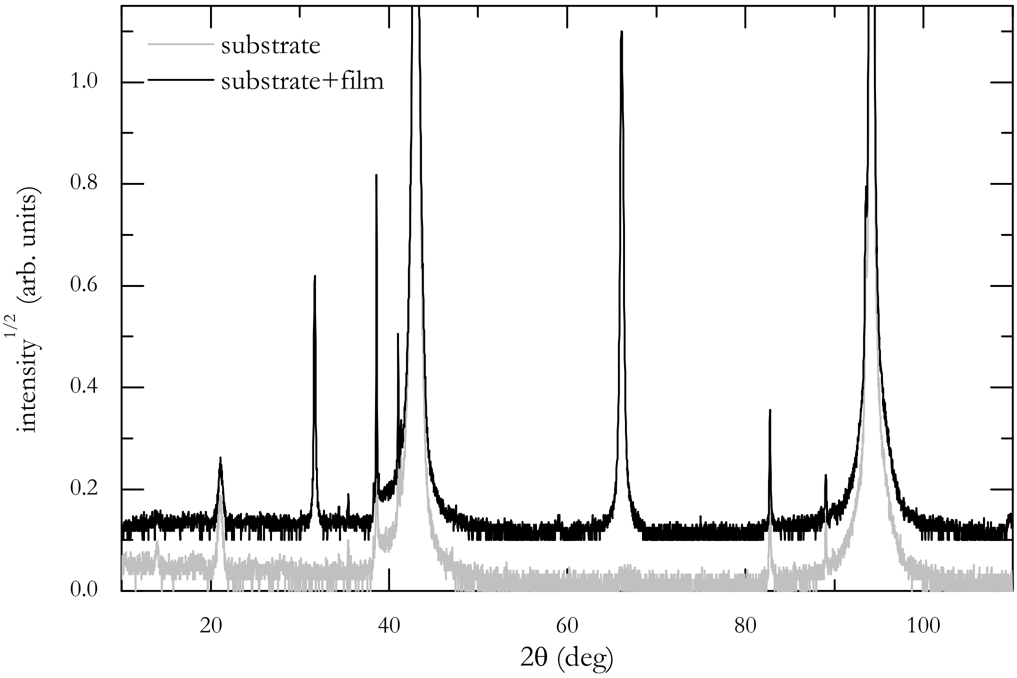

Figure 3.12: Bragg scan of an MgO substrate before and after film deposition. Film thickness is 70 nm Co_2FeSi, deposition temperature was 700 °C. The two curves are shifted along the ordinate for better visibility.

further be noted that the AFM findings do not contradict the more indirect evidence from X-ray diffraction and reflection, because a large portion of these films is indeed flat. In this case, the roughness cannot be described with a normal distribution. This is assumed in the models presented earlier, however.

High temperature deposition on MgO (100) substrates yields a different growth orientation, as shown in figure 3.12. Here the (200) and (400) diffraction signals can be detected. No additional signals and therefore no impurity phases are observed. The crystal size estimated with the Scherrer formula is approximately half of the film thickness, the ω scan of the (400) reflection has a FWHM of 0.35 °. Thus, the crystal size is smaller and the angular spread of the crystallites larger than in Co_2FeSi / Al_2O_3 films. Nevertheless, reported values for Co_2FeSi and comparable Heusler films are considerably larger [67, 105, 108, 145].

Furthermore, the in plane growth has a very high quality. The φ scan presented in figure 3.13 shows that only the expected fourfold symmetry of the {220} Heusler reflections is observed. Therefore, it can be concluded that truly epitaxial growth is realized for Co_2FeSi / MgO. The additional φ scan of the substrate shows that

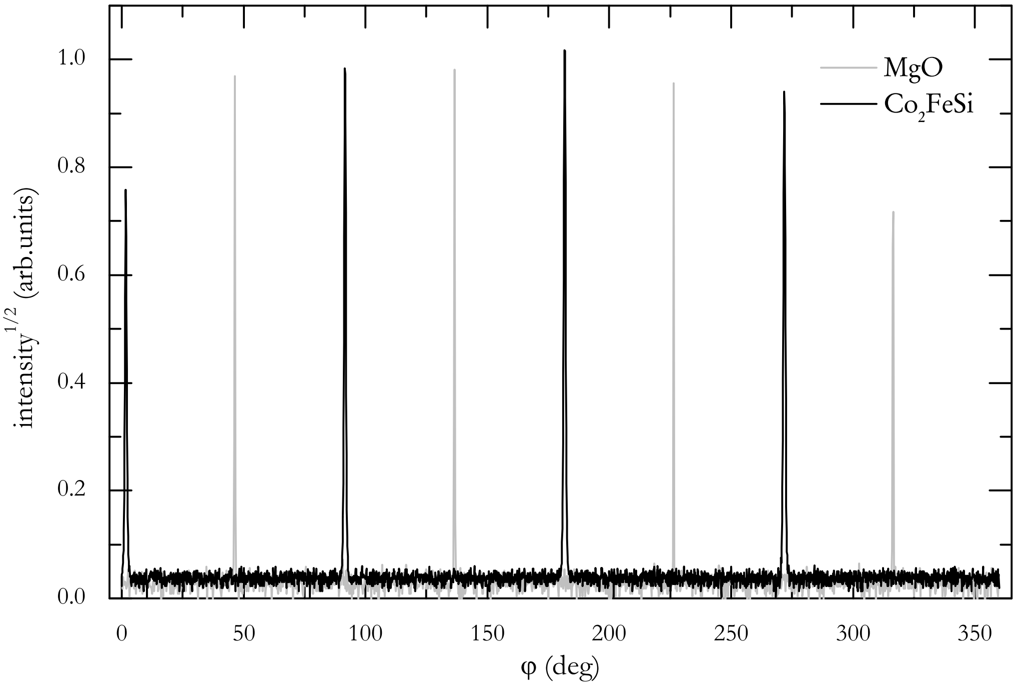

Figure 3.13: φ-scans of the {220} reflections of an MgO substrate and the Co_2FeSi film deposited on top.

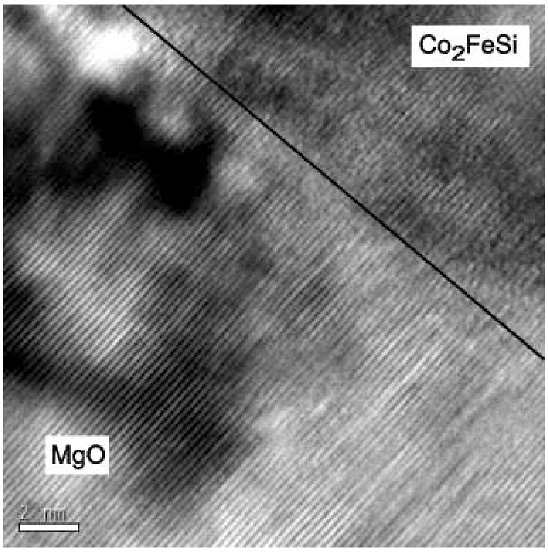

Figure 3.14: HRTEM image of an MgO-Co_2FeSi interface.

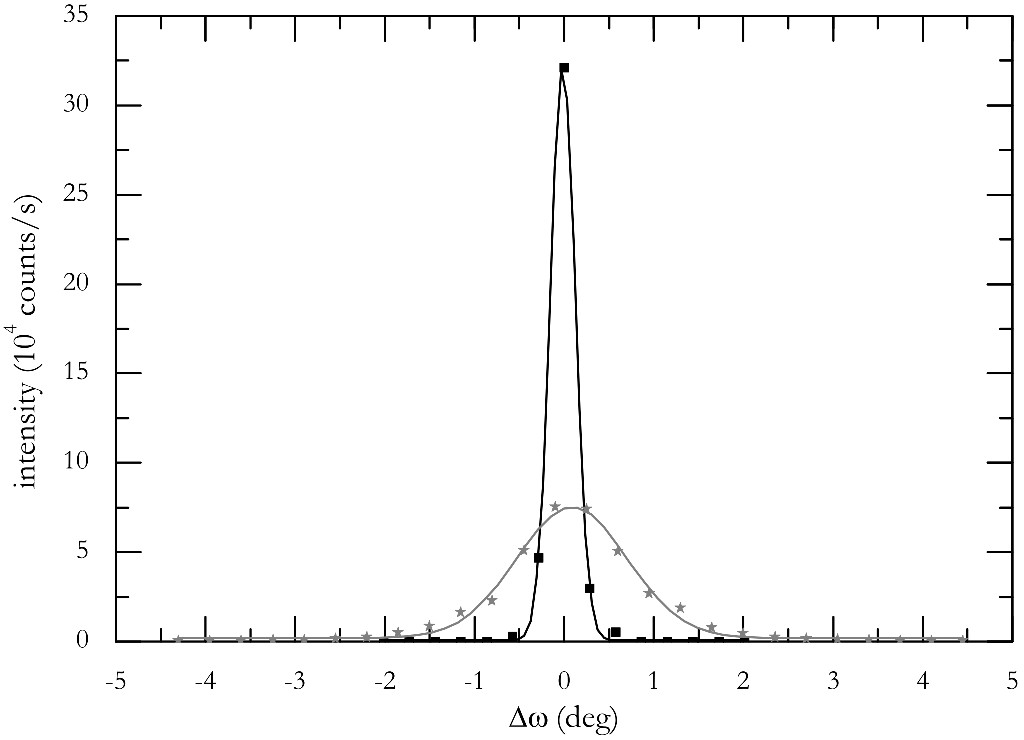

Figure 3.15: ω scans of the specular (220) (black) and the off-specular (202) (gray) reflection of a Co_2FeSi / Al_2O_3 sample. Icons mark experimental intensities, lines Gaussian fits. Despite the different line widths, the integrated intensities differ by less than 1 %.

the unit cells of both systems are rotated by 45 ° around the [100] axis. Despite a relatively large misfit of 5.6 % the interface between film and substrate is very well ordered as shown in the transmission electron micrograph of figure 3.14.

In order to estimate the atomic ordering in these samples, their peak intensities were analyzed as described in chapter 2.4. For this purpose ω scans of all accessible reflections were performed and their integrated intensities were compared. Summing over the total scattered intensities allowed the comparison of reflections with different line shapes, which occurred in Co_2FeSi / Al_2O_3 samples (see figure 3.15). Figure 3.16 compares the calculated values for different degrees of Co-Si disorder with the experimental intensities obtained for a sputtered Co_2FeSi / MgO film. It is noticeable that the experimental intensity of the (400) reflection is reduced by a factor of two compared with the expected value.

It should be recalled that the relative intensity of the principle (400) signal is independent of the details of the stoichiometry. This highlights the fact that the

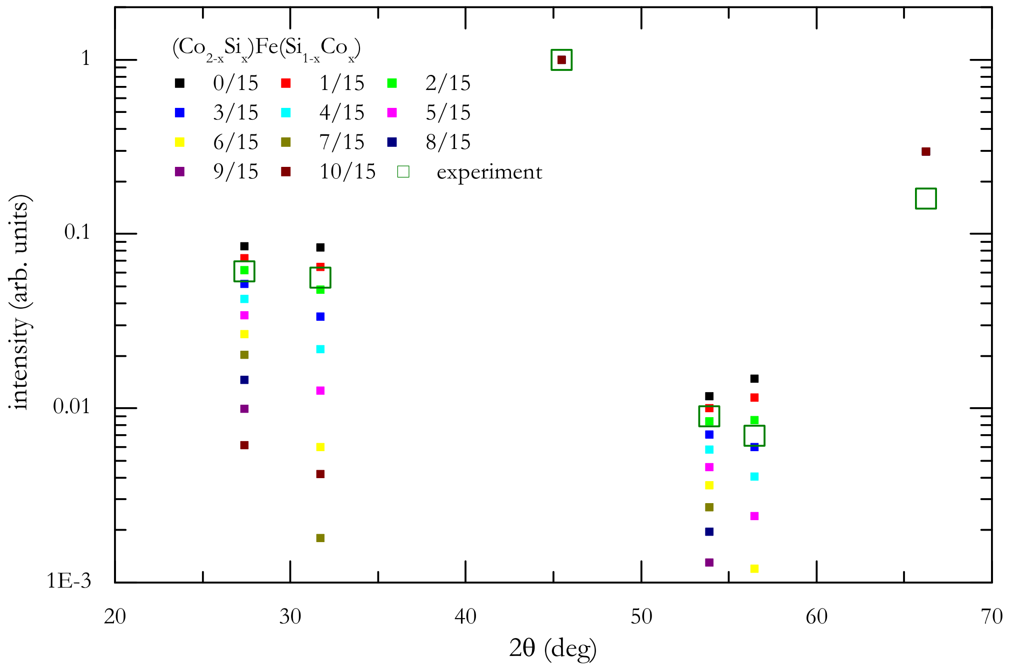

Figure 3.16: Relative X-ray intensities of a Co_2FeSi / MgO film. Open squares show the measured data. Filled squares show the calculated values for random Co-Si disorder.

simulated data obtained for powdered samples cannot readily be compared with thin film samples. As discussed above, the films show a pronounced columnar growth. Therefore, film thickness may be large compared with the lateral size of a crystallite, leading to a pronounced finite size broadening. In addition, the diffracted intensity of a thin film depends on the illuminated area, which is only approximately known. Despite these shortcomings and the obvious discrepancy of the (400) reflection it can be seen that the intensities of the other reflections are quite consistent. Their relative intensities can best be described with a disorder of 10 – 20 % Si atoms on Co sites and vice versa. It is noteworthy that this type of disorder is expected to be energetically unfavorable [53]. On the other hand, the kinetic energy of sputtered atoms is high enough to overcome this barrier. A second reasonable interpretation of the measured intensity ratios is the existence of an off-stoichiometry in the films. Figure 3.17 shows the intensities in case of an iron excess at the expense of silicon. In this case best agreement is obtained for a Si deficiency of 10 – 20 %.

In order to narrow down the possibilities, further structural investigations on these samples were performed by ^{59}Co spin echo NMR spectroscopy [58]. The recorded spectra show a distinct multiplet structure. This can be attributed to dif-

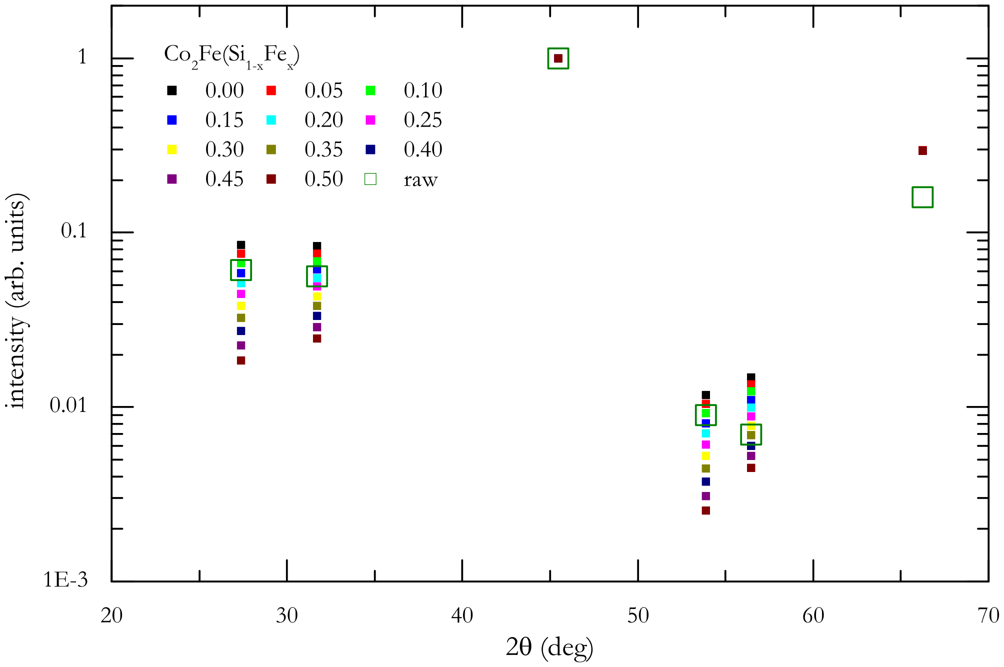

Figure 3.17: Relative X-ray intensities for the sample as in figure 3.16. Filled squares now represent Fe excess on Si sites.

ferent nearest neighbor configurations. All satellite peaks lie on the high frequency side of the main peak. Applying a simple statistical model and comparison with bulk samples shows that the composition of these samples is $Co_2Fe(Si_{0.9}Fe_{0.1})$. Other forms of disorder could not be detected. From these results, it can be seen that the analysis of scattered X-ray intensities may deliver a reasonable approximation of the short range ordering in the Heusler samples.

This deviation from the ideal $L2_1$ structure manifests itself in the magnetometry data presented in figure 3.18. From the hysteresis loops it can be seen that the saturation magnetization at 5 K does not exceed 5 μ_B/f. u.. Interestingly, despite this reduced value the temperature stability is better in the investigated temperature region than for bulk samples. The film magnetization scales with $T^{3/2}$, whereas the bulk curve may be described with a $T^{1.8}$ law. However, this might rather be the consequence of sample geometry than sample quality. Decrease in magnetization is commonly ascribed to spin-wave excitations. For $T \ll T_C$ only low-energetic magnons contribute to this change. In thin films, the formation of excitations with large wavelengths normal to the surface is not possible [148]. Further magnetic properties, especially the magnetic anisotropy, will be discussed in chapter 5.1.

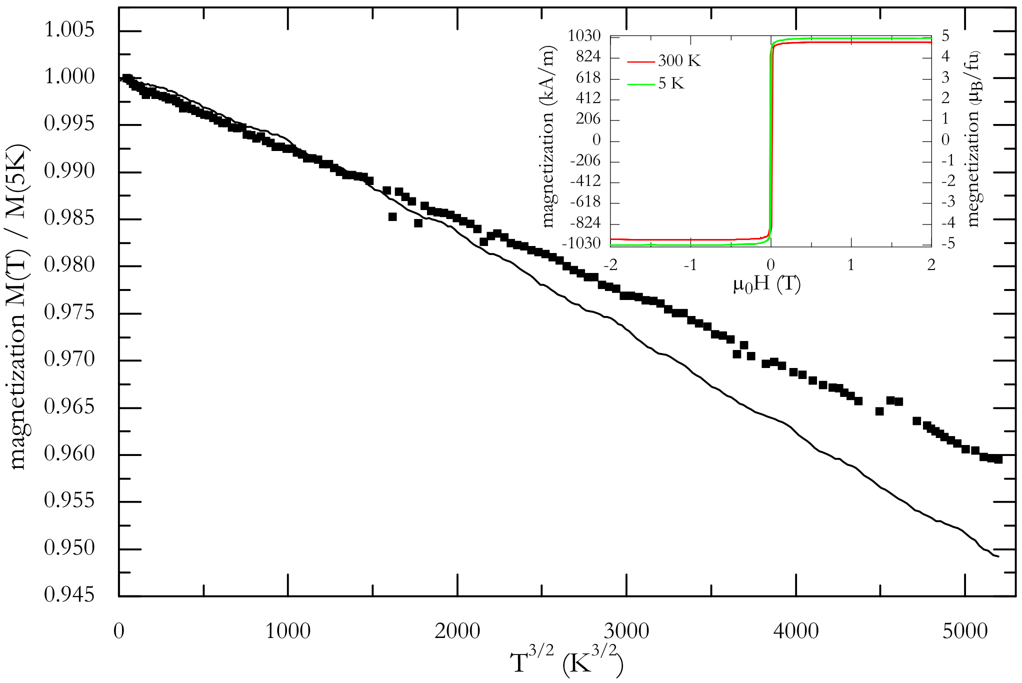

Figure 3.18: Temperature dependence of a Co_2FeSi / Al_2O_3 thin film (points) and a bulk sample (line) magnetization. The two curves are normalized to their low temperature values. The inset shows thin film hysteresis loops at different temperatures.

The sputter deposition at high temperatures reported so far yields the best quality Co_2FeSi films. It can be seen in figure 3.19 that for $T \gtrsim 650$ °C long-range crystal growth and magnetic moments are independent of deposition temperature. For lower substrate temperatures, these properties clearly deteriorate. Below 300 °C no long-range ordering can be observed. The evolution of the short-range order could not be quantified. Due to the peak broadening the low-intensity superstructure reflections are difficult to evaluate. However, the coinciding decrease of the saturation magnetization gives evidence that these low-temperature films veer further away from the optimal Heusler structure [52].

Thin film deposition at room temperature combined with a post-annealing step as described on page 38 for $Co_2Cr_{0.6}Fe_{0.4}Al$ yields similar results for Co_2FeSi. Again, no long range ordered growth could be induced by the heat treatment, but the magnetization values could be improved. Again the maximum value was obtained at 400 °C. In contrast to $Co_2Cr_{0.6}Fe_{0.4}Al$, it was not possible to improve the magnetic quality compared with the high-temperature samples. The best annealed samples also show a magnetization value of 5 μ_B/f. u..

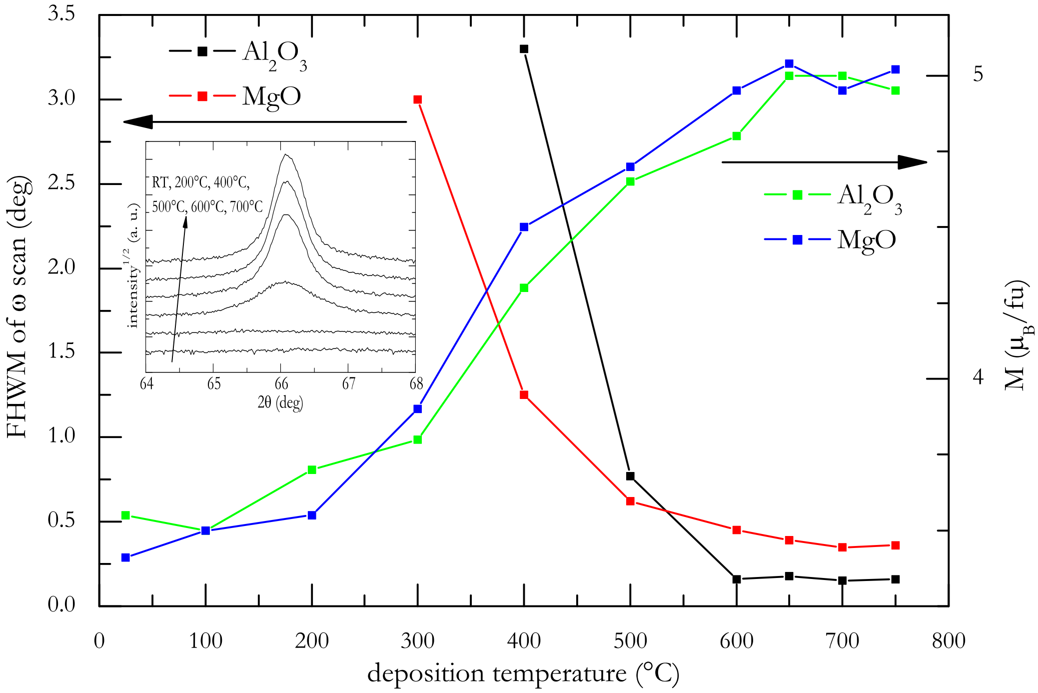

Figure 3.19: Dependence of structure and magnetization on deposition temperature. For $T < 300$ K no diffraction was observed. The magnetic moments were measured at 20 K. The inset shows the corresponding ω–2θ scans for Co_2FeSi / MgO films.

3.3 Pulsed Laser Deposition of $Co_2Mn_{1-x}Fe_xSi$

The data presented so far suggest that it is not possible to optimize sputter deposition of $Co_2Cr_{0.6}Fe_{0.4}Al$ and Co_2FeSi with respect to all properties desired of a Heusler thin film. Either epitaxial growth can be induced with high deposition temperatures, at the cost of a rough surface. Alternatively, a smooth, yet nanocrystalline film is obtained if sample preparation is carried out at room temperature. All films show noticeably reduced magnetic moments. It was pointed out in section 2.1 that these issues are likely to be resolved if a buffer layer is deposited between substrate and film. However, the results obtained hitherto as well as the data gathered from further publications [68, 149] demonstrate the need for better vacuum conditions.

This was the main reason for the development of a pulsed laser deposition process. As outlined in chapter 2.3, this technique allows dispensing with mechanical pumps as well as background gas during deposition. The base pressure of the UHV deposition chamber set up for this purpose could therefore be lowered to values

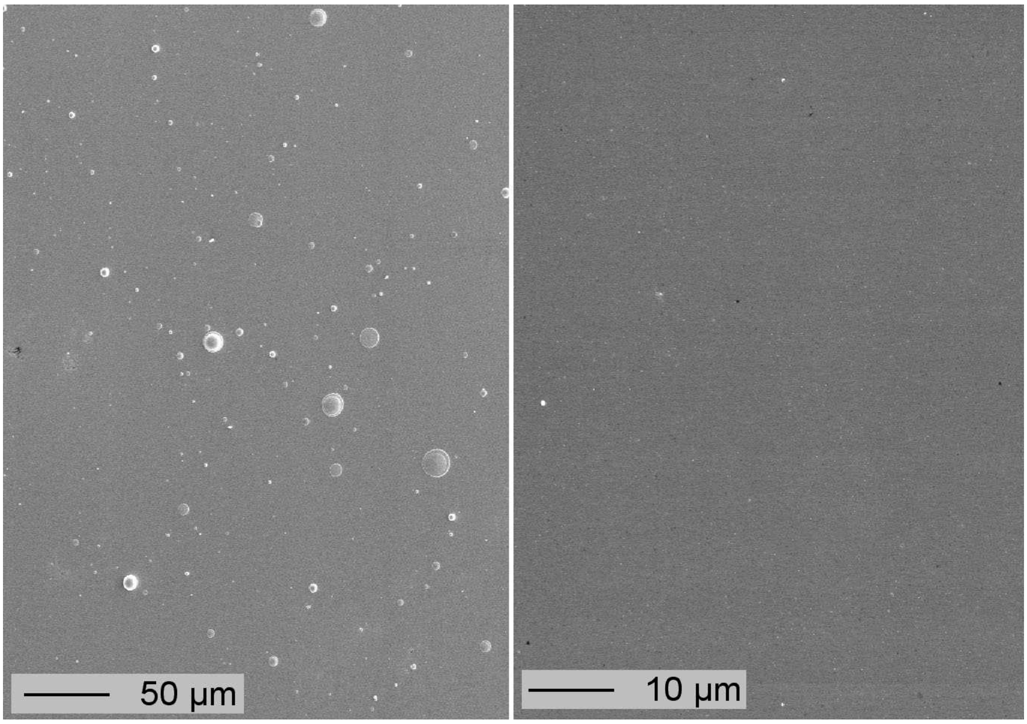

Figure 3.20: SEM images of Co_2FeSi film surfaces grown with PLD. The left sample was deposited with a pulse energy of 700 mJ, the other one with 300 mJ. Both films have a thickness of 40 nm and were deposited at room temperature.

of typically $1 - 2 \times 10^{-10}$ mbar, during heating phases it was possible to keep the pressure below 1×10^{-8} mbar.

As a first proof of concept, Co_2FeSi films were deposited with parameters comparable to their sputtered counterparts: again Al_2O_3 $(11\bar{2}0)$ and MgO (100) substrates were heated to 700 °C and the films grown directly on the crystals. The deposition rate could be adjusted by changing either the laser pulse frequency or the pulse energy. The former parameter could be set between 1 and 10 Hz, the latter one between 300 and 900 mJ. The resulting film growth rate was between 0.2 Å/min and 20 Å/min.

The main challenge with this deposition method is the aforementioned formation of melt droplets from the target material. The left SEM image in figure 3.20 shows indeed a large number of droplets at high pulse energies. This poses a major problem for volume integrating experiments. Assuming hemispherical particles, it can be estimated from the micrograph that the volumes of the droplets and of the film are of the same order of magnitude. Even though EDX spectra show that the composition of the droplet material approximates the Heusler stoichiometry, the nature of the microstructure remains in the dark [119]. Finally, the morphology at hand prohibits the fabrication of magnetic tunneling junctions.

On the other hand, in surface integrating experiments this contribution constitutes only a minor source of error. Even in the worst cases the surface coverage is less than 5 %. Since this value is well below the percolation threshold of the particles, transport experiments with the current flowing in the film plane are also unproblematic.

Deposition at low pulse energies just above ablation threshold proved the best method to suppress the formation of these droplets, as evidenced in the right hand part of figure 3.20. The downside of this method is the very low deposition rate of 0.2 Å/min. Further methods of droplet reduction have been presented in literature [119, 150]. However, they were not suitable in the situation at hand. Mechanical filters are based on the different velocities of plasma and particulates. This approach is not practicable, because the required quickly moving mechanical parts are impossible to realize under UHV conditions. Other methods exploit the different masses of the species. A high background pressure will cause the plasma to move diffusively while the heavy particulates continue to move in a straight line. This approach is not possible in a UHV setup either. Finally, the angular spread is higher for the plasma than for the droplets. So in order to improve film quality the substrate should be placed off center. This led indeed to a reduction of particulates, but the cost in deposition rate was even higher compared with the energy reduction technique.

Structural properties of these films are similar to the respective sputtered samples: (110)-oriented growth with several in-plane domains on Al_2O_3, (100)-oriented, fully epitaxial films on MgO. A change in deposition rate and therefore in droplet density has no observable influence on the diffractograms. For both growth orientations, the crystal quality of the samples yet increased. An improved long-range order is evident from better-defined reflections. In addition, the atomic ordering increased, since the relative intensity of the superstructure reflections is enhanced compared with the sputtered samples. For the laser deposited samples the approximate values of both Co-Si disorder and Fe excess respectively reduces to 5 – 15 %. These enhancements should result in an increased magnetization. Due to the melt droplets, meaningful values could only be acquired for Co_2FeSi deposited at low pulse energies. With a value of 5.9 ± 0.1 μ_B/f. u., these films are compatible with the Slater-Pauling rule. Disregarding droplets, the surface morphology for samples deposited on heated substrates is comparable for sputtered and laser ablated films. The loss of long-range order accompanied with a surface smoothing is also observed here.

These results demonstrate the potential of the newly installed pulsed laser deposition system for the deposition of Heusler films. In conjunction with improved vacuum conditions, this method allows the fabrication of Co_2FeSi films, whose quality is superior to the sputter deposited samples. However, not all issues could be resolved with this technique yet. Foremost, epitaxial growth with a smooth surface is still not achievable. Hence, the deposition of multilayered samples was attempted in order to induce crystallographic order at room temperature.

As a first step the elemental buffer layer was deposited at room temperature and annealed at 700 °C for both structural and morphological improvement. On Al_2O_3 substrates no epitaxial growth could be realized—most likely due to the differences in structure. The use of MgO substrates resulted in the desired formation of epitaxial, (100)-oriented buffer films with a smooth, crystalline surface. On these layers, Co_2FeSi was grown by laser ablation, yet again at room temperature.

Even without further treatment, these films showed ordered growth, which can be seen from the RHEED image on top of figure 3.21. The line shaped reflections indicate a smooth surface. An annealing treatment at 400 – 500 °C results in higher RHEED intensities of the first order reflections, also second order reflections are weakly visible. This shows an increase of the structural quality in these samples. Further treatment at even higher temperatures leads again to a loss in intensity (see figure 3.22). Similar to the nanocrystalline Heusler films this reduction is correlated with a diffusion of the buffer layer material into the film [151].

The bulk structural properties of films annealed in the optimal temperature range are exemplified in figure 3.23. Film growth is (100) oriented, impurity phases are not present. The FWHM of the ω scans is with values between 0.8 and 1.0 ° considerably higher than for the high-temperature samples. For Heusler films sputter deposited under similar conditions comparable values have been published [49, 108]. In-plane φ scans show epitaxial growth, the $\{111\}$ reflections are present. The large width combined with the small intensities of the $L2_1$ superstructure reflections results in a low signal to noise ratio which prohibits a quantitative analysis of the relative peak intensities.

These results demonstrate that the pulsed laser deposition system in use is well suited not only for the high temperature fabrication of epitaxial thin films. Also low temperature growth of Co_2FeSi on buffer layers yields highly ordered samples with the desired flat surface. Therefore, in a next step the pulsed laser deposition technique was extended to the quaternary alloy series $Co_2Mn_{1-x}Fe_xSi$.

In order to obtain a higher flexibility, deposition was not carried out with different targets for different Fe concentrations. Instead, one semi-disc of each Co_2FeSi and Co_2MnSi were mounted onto a single target holder. The stepper motor controlling the target rotation and the laser pulse trigger were synchronized in such a way

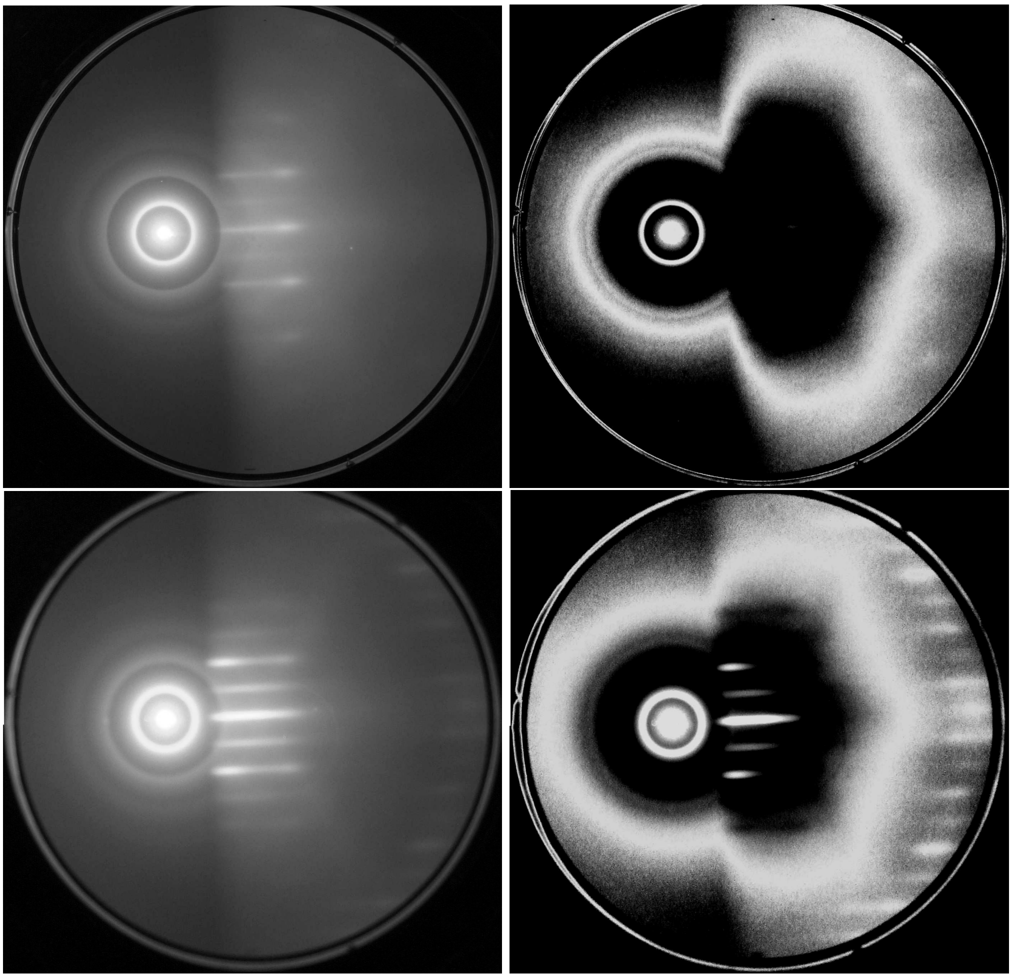

Figure 3.21: RHEED patterns a Co_2FeSi / Cr / MgO film after deposition at room temperature (top) and after annealing at 450 °C (bottom). In order to highlight the presence or absence of darker features in the images, discolored versions of the photos have been placed on the right hand side.

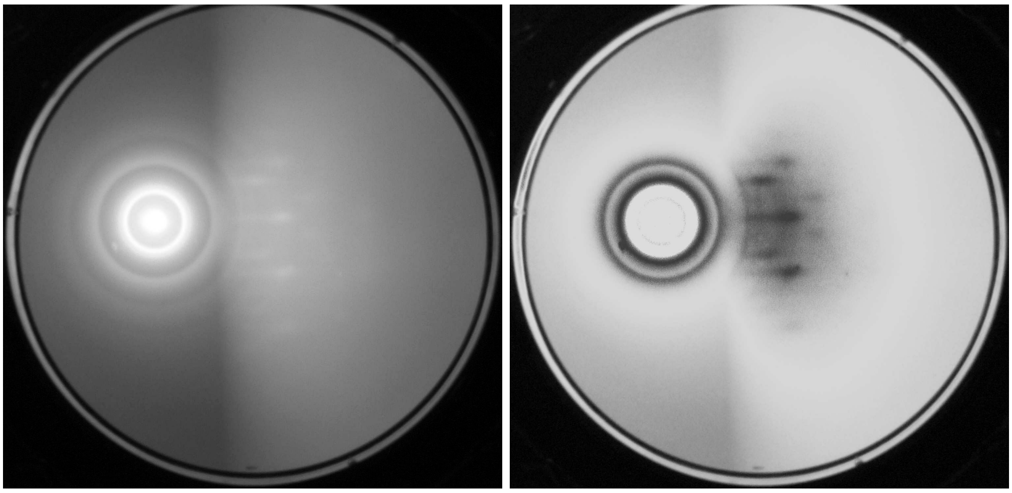

Figure 3.22: RHEED pattern of the same sample as in figure 3.21 after annealing at 700 °C. The left hand part shows the original photo, the right hand one a discolored version.

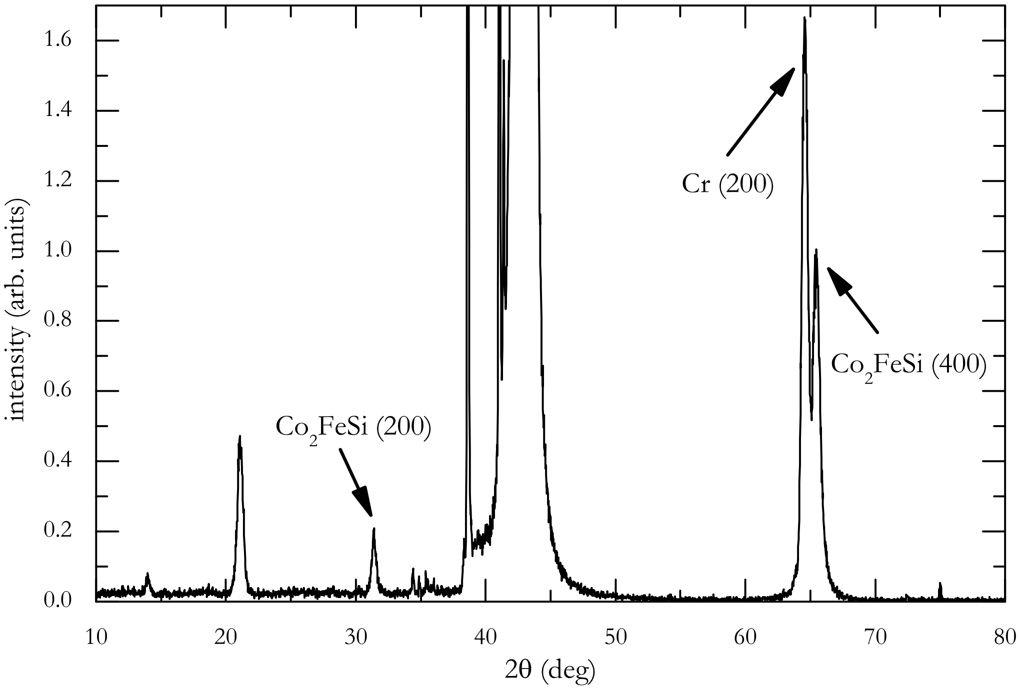

Figure 3.23: Bragg scan of a Co_2FeSi (30 nm) / Cr (40 nm) / MgO film annealed at 400 °C.

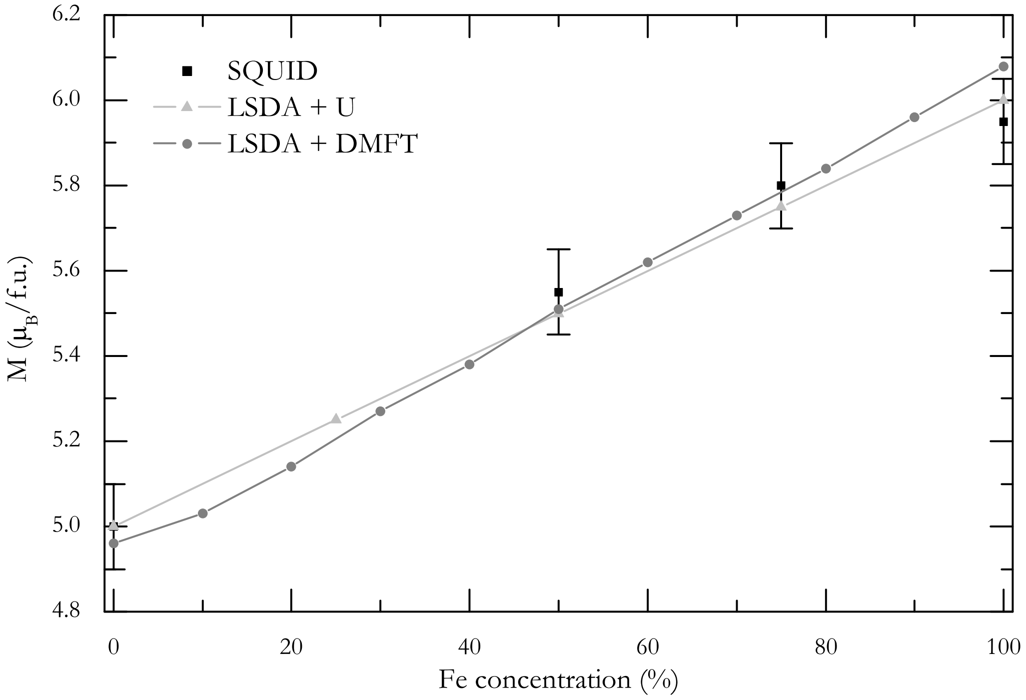

Figure 3.24: Magnetometry data of $Co_2Mn_{1-x}Fe_xSi$ for varying x. For comparison, the values from LSDA+U (which coincide with the Slater-Pauling rule) and LSDA+DMFT calculations are included.

that the film stoichiometry could be adjusted by varying the number of pulses on the respective ternary bulk targets.

Again, first samples were deposited on heated MgO substrates. Structural properties over the whole concentration range were comparable to both the respective bulk samples and the Co_2FeSi thin films. Epitaxial (100) oriented growth in the ordered $L2_1$ structure was seen for all values of x. The bulk magnetization increased linearly with increasing Fe content and was within errors compatible with the Slater-Pauling rule as well as LSDA+DMFT calculations, which predict a deviation from the Slater-Pauling line due to spin-orbit coupling. Finally, also the deposition of $Co_2Mn_{1-x}Fe_xSi$ films on a buffer layer was attempted. This technique proved also succesful. The fabricated samples show a similar behavior to the corresponding Co_2FeSi samples presented previously. Again, $L2_1$ order was observed for all concentrations of x. The magnetization seems to follow the predicted values, even though the presence of a buffer layer is an additional source of error, because it impedes the precise determination of the film thickness.

Since $Co_2Mn_{1-x}Fe_xSi$ has a practically unchanging structure and since a linear dependence of the magnetization on the iron concentration is to be expected, it is difficult to rule out the formation of Co_2FeSi and Co_2MnSi clusters instead of complete interdiffusion. However, it has been shown that a high deposition or annealing temperature is the source of interdiffusion and alloying [143]. Additional XMCD experiments on a series of $Co_2Mn_{1-x}Fe_xSi$ samples rule out larger contributions from ternary clusters as well [152]. EDX spectra, which sample over an area of several μm^2 and the whole film thickness, did not show any large-scale variations.

The succesful epitaxial growth of $Co_2Mn_{1-x}Fe_xSi$ shows that pulsed laser deposition is a flexible method for the deposition of high quality Heusler alloy thin films: The detection of the L21 crystal structure as well as the adherence of the Slater-Pauling rule for Heusler alloys are consistent with half-metallicity. The successful growth of the whole quaternary series directly on dielectric Al_2O_3 or MgO substrates opens the possibility to perform systematic investigations of their transport properties. Additionally, the use of metallic buffer layers led to epitaxial samples with a very smooth surface. This allows the performance of further experiments such als Brioullin Light Scattering or spin-polarized tunneling.

CHAPTER 4

ELECTRONIC TRANSPORT

In the preceding chapter, the successful growth of $Co_2Mn_{1-x}Fe_xSi$ directly on insulating substrates has been presented. This class of samples allows the application of an electrical current in the film plane. Such samples can therefore be used to probe the isothermal magnetoresistance and the Hall effect. It is well known that the electronic transport phenomena in solids are almost entirely determined by electrons near the Fermi energy. A systematic study of the transport behavior can therefore be used to gain insight into the properties of the Fermi surface. In this work, the interpretation of the experimental data is in most cases based upon the framework of the Boltzmann equation [153]. This formalism allows neither the direct quantification of the spin polarization nor a mapping of the electronic density of states. But in contrast to tunneling or photoemission experiments, only a comparatively simple experimental setup is required and the results are quite robust with respect to surface degradation.

Despite this ostensible simplicity, some experimental details relevant in the context of this work have to be clarified first. They are discussed in the first part of this chapter. Afterward, the acquired experimental data are presented and the relevant theoretical interpretations are introduced. The results are then discussed with respect to the predicted electronic properties of $Co_2Mn_{1-x}Fe_xSi$.

4.1 Experimental Considerations

In isotropic systems, Ohm's law states that that the electrical current is proportional to the drop of the electrostatic potential along its path. In order to eliminate the geometry of the samples it is conventionally formulated as a relation between current density and field: $\mathbf{E} = \rho \mathbf{j}$. The scalar nature of the resistivity ρ signifies that that the two vectorial quantities are parallel.

Anisotropy can be induced in isotropic solids with the application of an external magnetic field or the presence of a nonzero sample magnetization. In this situation $\mathbf{j}$ and $\mathbf{E}$ are no longer necessarily parallel. Therefore, Ohm's law assumes the generalized form $E_i = \sum_k \rho_{ik}(\mathbf{B},\mathbf{M}) j_k$, with the resistivity ρ_{ik} now a second-rank tensor. From symmetry considerations [154] it can be shown that for a system magnetized in z direction the tensor has the form

$$\left(\rho_{ik}\right) = \begin{pmatrix} \rho_{xx,\perp}(\mathbf{B},\mathbf{M}) & -\rho_{xy}(\mathbf{B},\mathbf{M}) & 0 \\ \rho_{xy}(\mathbf{B},\mathbf{M}) & \rho_{xx,\perp}(\mathbf{B},\mathbf{M}) & 0 \\ 0 & 0 & \rho_{xx,||}(\mathbf{B},\mathbf{M}) \end{pmatrix}. \tag{4.1}$$

The diagonal elements $\rho_{xx,||}$ and $\rho_{xx,\perp}$ describe the Ohmic resistivities for the current components parallel and perpendicular to the magnetic field. In situations where the direction relative to the magnetic field is not relevant, the indices || and ⊥ are omitted. The off-diagonal quantity is the Hall resistivity. The electronic transport in samples with cubic crystal symmetry behaves like in an isotropic system. Therefore, the resistivity tensor also assumes the form of equation (4.1) [155, 156]. Consequently, for the transport experiments in this work the current direction relative to the crystal orientation is not relevant. The symmetry considerations so far only explain the existence of the different galvanomagnetic effects. Their dependence on external parameters and their microscopic origin will be discussed later.

Experimentally the different tensor elements are all probed by four-contact measurements. A DC current source is used to deliver a defined current density through the sample. The voltage drops caused by the different effects can be determined by appropriately placing the sensing contacts with respect to the primary current and the external field. These geometries are sketched in figure 4.1, along with a definition of the relevant physical quantities. The longitudinal and transversal resistances $R_{xx,||}$ and $R_{xx,\perp}$ are calculated with Ohm's law. The Hall resistance R_{xy} is defined as U_{xy}/I.

Even though it is possible to approximate both Ohmic and Hall resistivities of arbitrarily shaped samples with the van der Pauw method [157], measurements on samples with well-defined current leads allow a better reproducibility and more homogeneous field conditions. This was realized by a standard photolithographic process in combination with ion beam etching. The method is briefly illustrated in appendix A.

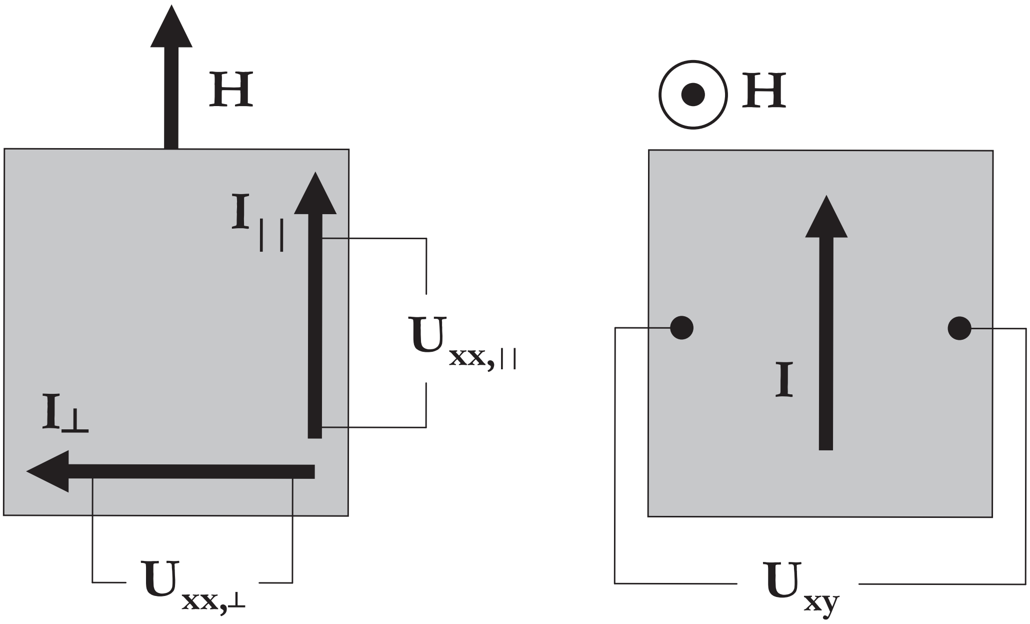

Figure 4.1: Sketch and denotation for the magnetoresistance (left) and Hall (right) experiments.

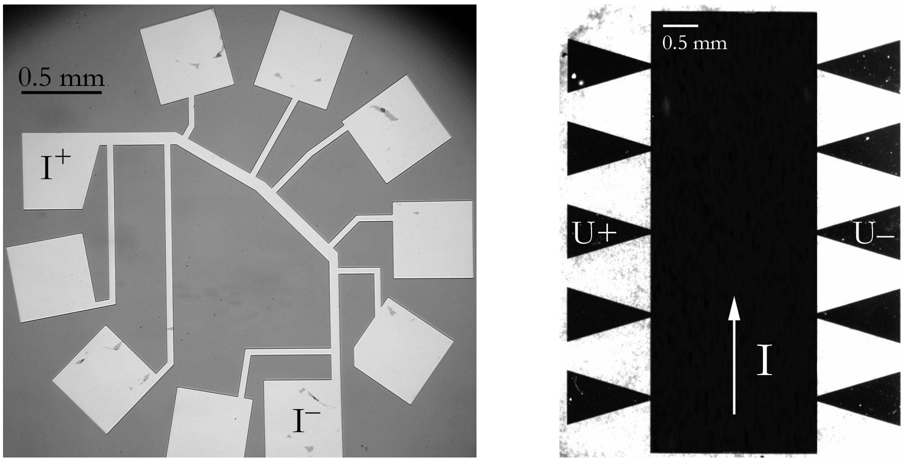

Figure 4.2: Film patterns for transport measurements. The left structure was used for magnetoresistance, the right one for Hall effect experiments.

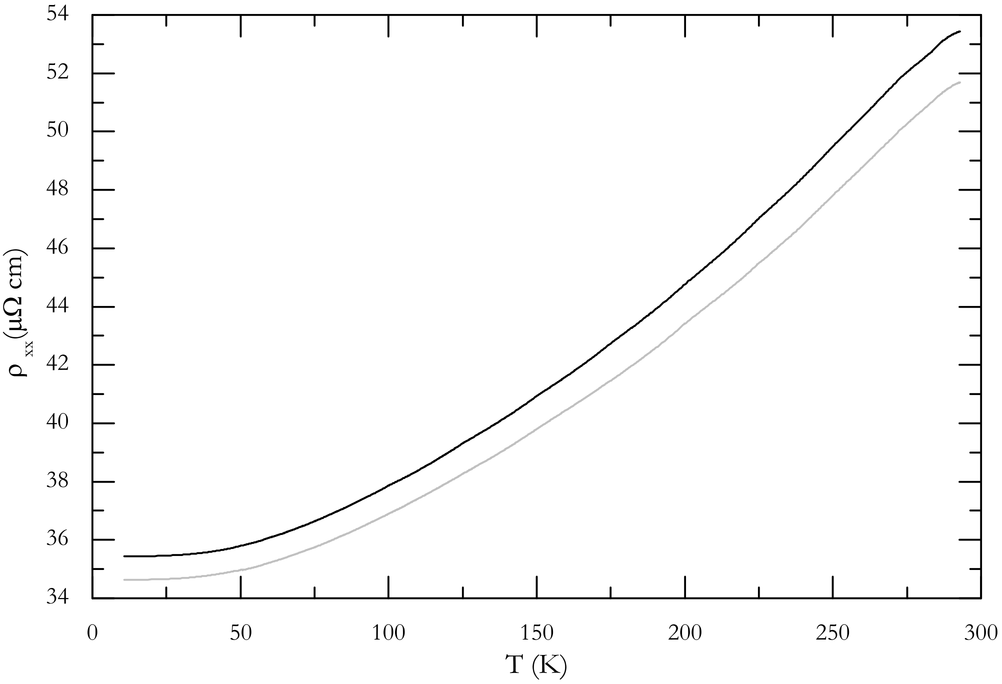

Figure 4.3: Temperature dependent resistivity of sputtered Co_2FeSi thin films with (gray) and without (black) Al protection layer. All other parameters remained unchanged.

For the measurement of the anisotropic magnetoresistive properties the structure shown on the left hand side of figure 4.2 was employed. The DC current was applied along the central lead, the directed voltage drops were measured along the piecewise straight parts. Depending on the film resistivity, a current density between 1000 and 2000 A/m^2 was applied through these samples.

For the Hall experiments the structure shown in the right hand part of figure 4.2 was used. The Hall voltage depends on the sample thickness t and the current I as

$$U_{xy} \propto \frac{I}{t}. \tag{4.2}$$

It is independent on sample width, therefore a broad central bar has been used [158] in order to maximize the transmitted current. For this reason, the applied current *densities* were reduced by approximately one order of magnitude compared with the magnetoresistance experiments.

In all transport experiments, voltage contributions caused by temperature gradients needed to be eliminated. This was realized by performing two measurements with antiparallel current direction and subsequent averaging of the two results. A non-perfect alignment of the contacts is a source of error in the Hall experiments. The resulting additional Ohmic contributions to the measured voltage was eliminated by antisymmetrizing the branches for opposite magnetic field directions.

Samples were placed inside a variable temperature inset of a ^{4}He cryostat. With this setup sample temperature could be varied between 2 and 300 K. Magnetoresistance and Hall effect were measured by sweeping the magnetic field generated by superconducting coils at fixed temperature. The sample normal could be positioned either parallel or perpendicular to the external field.

As mentioned in the previous chapters, the thin film samples were routinely protected with a thin aluminium capping layer. For transport measurements, this presents a potential source of error. Since aluminium forms a passivation layer, it is possible that not all of the material is oxidized. The remaining metallic film can distort the measurements of the Heusler samples. An uncoated film on the other hand will be impaired due to oxidation. In order to estimate the influence of these two effects, transport experiments for both sample types were compared. Figure 4.3 shows the temperature dependent resistivity of two samples whose only difference is the presence or absence of the aluminium cap layer. It can be seen that the two resistivity curves are shifted by 2 %. Otherwise, no discrepancies were observed. Additionally, the properties of an uncoated sample immediately after deposition and after exposure to ambient conditions over a period of 6 months were compared. A measurable change of crystal structure or magnetic properties could not be detected. It can therefore be concluded that the Heusler compounds also form a passivation layer at the surface, which protects the bulk of the samples from further degradation.

Another issue related with sample preparation is the surface morphology. It was shown in figure 3.11 on page 48 that epitaxial film growth is accompanied by a rough surface. This raises the question of the influence on the transport experiments. It can be seen from the AFM image that despite this pronounced roughness connected paths over the sample exist. Therefore, electrical conductivity could usually be observed also in the epitaxial samples. The films were only insulating under two circumstances. The first class of samples was very thin. In this case, the individual islands had not yet coalesced into a cohesive film. Electrical insulators were also produced if the substrate temperature during sputter deposition clearly exceeded 700 °C. This effect is independent of the film thickness. However, as presented in figure 3.19 on page 55, these films showed no structural or magnetic differences to the samples deposited between 600 and 700 °C. It is therefore possible that in this case the high temperature causes oxidation especially at the crystallite grain boundaries.

Finally, before the experimental data are presented, it should be recalled from section 3.3 that the presence of melt droplets on laser ablated films poses no obstacle for transport experiments either. Less than 5 % of the surface was found to be covered with particulates, which is far from the percolation limit. Additionally, their stoichiometry is comparable to the film composition, which should lead—to a first approximation—to the same transport behavior.

4.2 Zero-Field Resistivity

A metal with a perfectly periodic lattice has a vanishing electrical resistance. In real materials, several contributions cause a deviation from this ideal case and therefore a finite resistivity value. These mechanisms can approximately be regarded as independent of each other. The total value can then be calculated as the sum of the individual processes [153]. In non-magnetic materials, the scattering of electrons from impurities and phonons has to be taken into account. The former case is temperature independent. In the temperature range investigated in this work the latter contribution is the source of the Bloch-Grüneisen T^5 behavior.

For conventional ferromagnets, the dominant mechanism is the coherent one magnon scattering [159]. In this scenario the spins of the conduction electrons are exchange coupled with the localized moments, which themselves are ferromagnetically aligned at $T = 0$. At finite temperatures, the directions of the localized spins fluctuate and form spin waves. This thermally induced “spin disorder” causes the conduction electrons to scatter from the now imperfect exchange potential. The interaction between one conduction electron and one magnon causes the spin of the electron to flip. This scattering process gives rise to a T^2 dependence of the resistivity. Incoherent one magnon scattering is expected to contribute as $T^{3/2}$ [160, 161] to the resistivity.

For half-metallic ferromagnets, the one magnon mechanism $|\mathbf{k}_{\uparrow\downarrow}\rangle \rightarrow |\mathbf{k}'_{\downarrow\uparrow}\rangle$ is not possible due to the complete absence of one spin direction at the Fermi edge. In this case, the spin conserving two-magnon scattering is the process which yields the most dominant contribution. This results in a higher exponent of the temperature dependence. In a rigid band model it was predicted that $\rho_{xx} \propto T^{9/2}$ [162]. The influence of spin fluctuations at finite temperatures is claimed to reduce this temperature dependence in half-metals to T^3 [163].

It can be seen from figure 4.3 that the sputtered Co_2FeSi films exhibit the expected metallic behavior over the investigated temperature range. At low temperatures a resistivity of $\rho_{xx}(5\,\mathrm{K}) = 35\ \mu\Omega\mathrm{cm}$ is observed. It signifies a noticeable number of impurity scattering centers, in line with disorder found by X-ray analy-

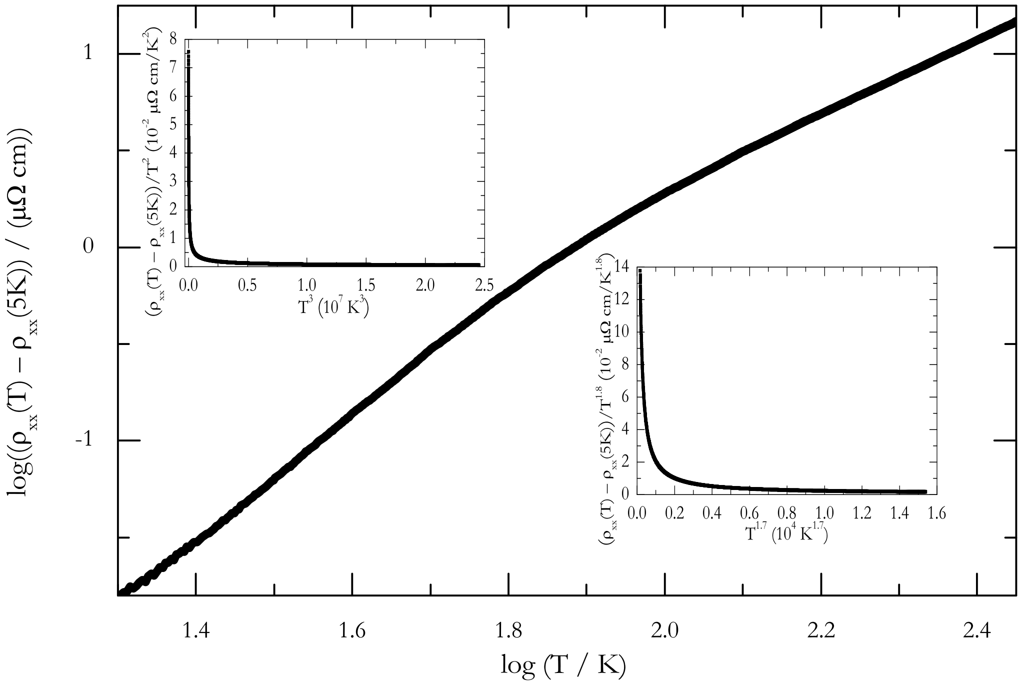

Figure 4.4: Double logarithmic plot of the T-dependent resistivity of the uncapped sample in figure 4.3. The insets show replots for an assumed $\alpha T^2 + \beta T^5$ (upper left) or $\alpha T^{1.8} + \beta T^{3.5}$ (lower right) behavior.

sis. Consequently, the residual resistivity ratio $\rho_{xx}(300\text{ K})/\rho_{xx}(5\text{ K})$ has a low value of 1.5. It shows that even at room temperature the contribution from impurity scattering plays a more dominant role than thermally induced processes. Nevertheless, these values are better compared with transport experiments on other Heusler films [100, 164, 165]. This again proves that despite the known shortcomings the crystal structure of Co_2FeSi has a higher quality than previously reported thin Heusler films.

All scattering processes presented above cause the resistivity to vary as T^α, with the value of α dependent on the actual mechanism. In order to identify the microscopic origin of the temperature dependence, the data shown in figure 4.3 is replotted on a double logarithmic scale in figure 4.4. This curve does not show a linear behavior over the investigated temperature interval. The resistivity can therefore not be described by a single power law. Instead, it was found that the data is best modeled by distinguishing between a high- and a low-temperature regime. For $100\text{ K} \lesssim T \leq 300\text{ K}$ the resistivity scales with a constant α of 1.8. If the temperature is lowered below 100 K, the exponent of $\rho_{xx}(T)$ gradually increases until it reaches again a stable behavior of $T^{3.5}$ below 50 K. Qualitatively similar crossovers between high-temperature and low-temperature exponents have been reported for other Heusler compounds as well [165, 166]. In these publications, the resistivity also shows a strong temperature dependence at low temperatures that weakens if the sample is heated up.

An alternative possibility to describe the evolution of the resistivity is to consider the combined effect of multiple scattering processes over the whole temperature interval. For this purpose it has to be checked whether the resistivity can be described as the sum these contributions. However, it is exemplified in figure 4.4 that this approach does not describe the measured data satisfactorily. The inset in the upper left part assumes that the resistivity is caused by phonon- and magnon-scattering. In this case the resistivity should follow $\rho_0 + \alpha T^2 + \beta T^5$, a plot of $(\rho_{xx} - \rho_0)/T^2$ against T^3 must therefore show a linear behavior. Similarly the lower right inset tests for the relation $\rho_{xx} = \rho_0 + \alpha T^{1.8} + \beta T^{3.5}$. Both graphs—and all other plots generated in an analogous fashion—show a clearly nonlinear behavior.

From these observations, it can be concluded that the relative contributions from different mechanisms are not fixed. Instead, with increasing sample temperature an additional scattering channel is opening up. This results in a weaker temperature dependence of the resistivity. It is, however, difficult to identify the relevant processes involved. Not only are available theoretical models unable to reproduce the exact experimental exponents. In addition, the accuracy of the calculations mentioned above is debatable. They are all based on simplified assumptions of the Fermi surface and on a single exchange-split band. Additionally, yet unknown or poorly understood processes may contribute to the zero-field resistivity. Here a possible candidate is the formation of non-quasiparticle states (see also page 11). Consequently, even though the evolution of the zero-field resistivity does not contradict half-metallicity in the investigated samples, it is no proof. Therefore, additional experiments have to be performed in order to decide on this question.

The $\rho_{xx}(T)$ behavior of a nanocrystalline Co_2FeSi film is illustrated in figure 4.5 for several annealing temperatures. A high degree of disorder in the untreated sample is the cause of a high residual resistivity and a weak temperature dependence. Additionally, the behavior is no longer metallic at low temperatures. At $T \approx 60$ K the curve assumes a minimum and with further cooling the slope $d\rho_{xx}/dT$ becomes negative. Similar resistance minima occur frequently in alloys and disordered compounds. They originate from incoherent impurity scattering, which causes a spatial localization of the previously extended Bloch electrons [167]. After annealing at 400 °C, these localization effects disappear and the residual resistivity drops to a value comparable to epitaxial samples. A further heat treatment at even higher temperatures causes this value to increase again.

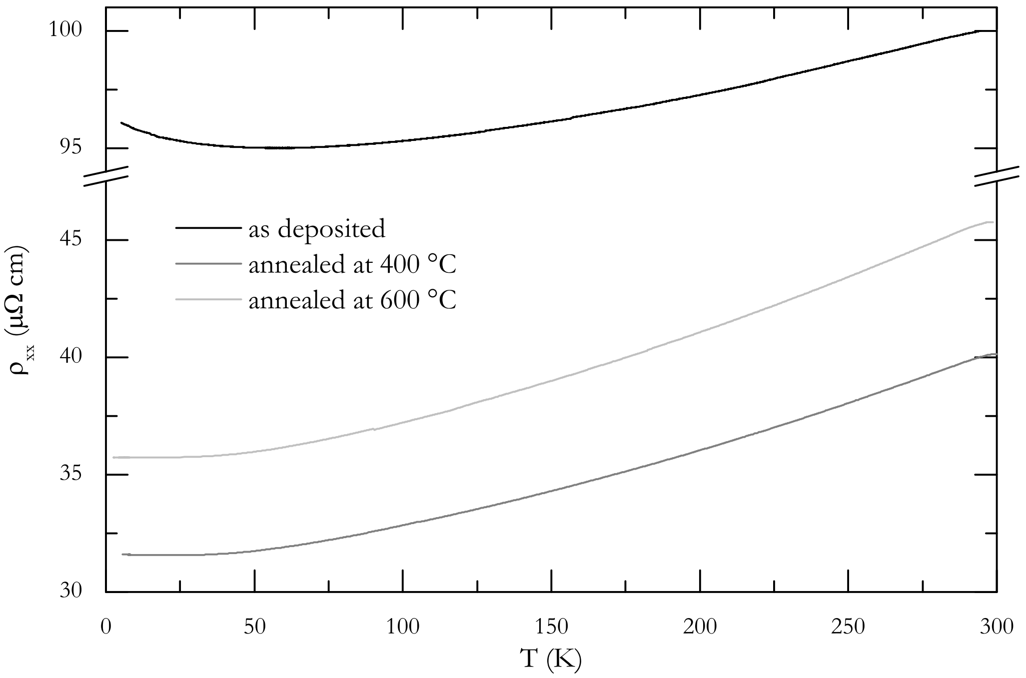

Figure 4.5: Temperature dependent resistivities of a nanocrystalline Co_2FeSi film annealed at various temperatures.

This behavior is in line with the findings from magnetometry. The high degree of disorder in nanocrystalline Co_2FeSi films not only decreases the sample magnetization but also derogates the transport properties. The increase of the short-range crystal order results in a magnetization value comparable to the single crystalline films, signifying an increase of $L2_1$ order. The same change of the atomic order is now responsible for the improvement of the low-temperature transport properties. The much higher fraction of grain boundaries compared with the epitaxial films seems to play only a negligible role. Similarly, the rise of the low-temperature resistivity coincides with the renewed reduction of the magnetization due to alloying between film and capping layer.

4.3 Magnetoresistance

Figure 4.6 shows the magnetic field dependence of the resistivity in a sputter deposited Co_2FeSi sample at a fixed temperature of 4 K. Two effects are visible in this image. The first one is a small resistance difference depending on the orientation

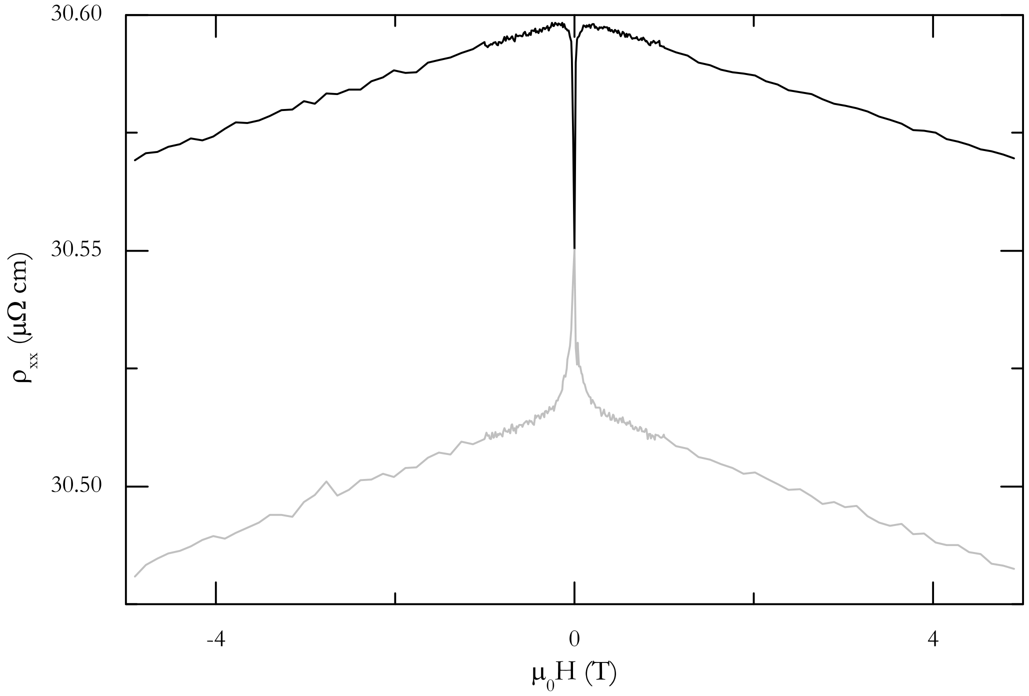

Figure 4.6: Magnetoresistance of a sputtered Co_2FeSi film measured at 4 K. The black line represents $\mathbf{j} \perp \mathbf{H}$, the gray line $\mathbf{j} \,||\, \mathbf{H}$.

of the current relative to the external field. This is the anisotropic magnetoresistive (AMR) effect, which is expressed by the different diagonal components $\rho_{xx,||}$ and $\rho_{xx,\perp}$ of the resistivity tensor (4.1). In this work, the relative magnitude of this spontaneous resistivity anisotropy is defined as

$$\mathrm{AMR} = \frac{\rho_{||} - \rho_{\perp}}{1/3\rho_{||} + 2/3\rho_{\perp}}. \tag{4.3}$$

The values $\rho_{||}$ and $\rho_{\perp}$ are obtained by extrapolating the high-field behavior of $\rho_{xx,||}$ and $\rho_{xx,\perp}$ to $\mathbf{H} = 0$. The different weights for the two current directions in the denominator are chosen because of their unequal representation in the magnetoresistivity tensor [168].

The AMR ratio for the sample at hand is -0.3 %, the absolute difference of the two branches is 0.08 $\mu\Omega$cm. The latter quantity is nearly independent of sample temperature. Since $\rho_{||} \approx \rho_{\perp} \gg |\rho_{||} - \rho_{\perp}|$, the temperature dependence of the relative anisotropy is dominated by the increase of the zero-field resistivity. Consequently, the AMR ratio reduces to -0.2 % at room temperature.

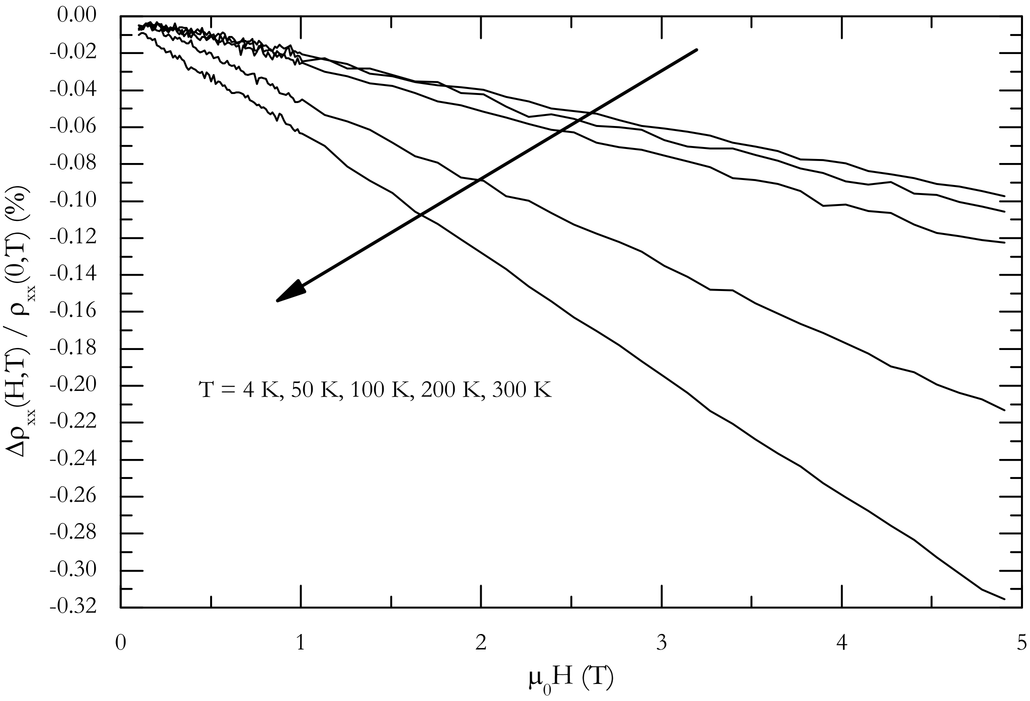

Figure 4.7: Temperature dependence of the high-field magnetoresistance in Co_2FeSi. The curves shown here represent the case $\mathbf{j} \perp \mathbf{H}$.

The occurrence of the AMR effect is commonly attributed to the scattering of itinerant *s* band electrons into localized *d* orbitals [169, 170]. The presence of spin orbit interaction lifts the degeneracy of the *d* orbitals, causing different scattering rates for electrons flowing parallel or perpendicular to the sample magnetization. For the films investigated here, this interpretation has two consequences. First, it reveals the presence of spin orbit interaction in the samples. Second, it shows the presence of unsplit *s*-bands at the Fermi edge. The latter point signifies that the spin polarization of these samples is less than 100 %. It is, however, not possible to quantify the reduction of the spin polarization solely from the data obtained here. Nevertheless, it should be noted that the effect is weak compared with conventional binary transition metal alloys. These materials can exhibit low temperature anisotropy ratios of more than 20 % [169].

The second feature of interest in figure 4.6 is the magnetoresistance above technical saturation. It can be seen that the resistance decreases linearly with higher applied fields. With increasing sample temperature, the slope increases, as shown in figure 4.7. The “normal” magnetoresistive behavior, present at low temperatures

Table 4.1: Magnetoresistive properties of pulsed laser deposited $Co_2Mn_{1-x}Fe_xSi$. Sample temperature in all cases was 4 K.

Material	resistance anisotropy (%)	high-field slope ($\mu\Omega$cm/T)
Co_2MnSi	−0.25	−0.0055
$Co_2Mn_{0.5}Fe_{0.5}Si$	−0.2	−0.0045
$Co_2Mn_{0.25}Fe_{0.75}Si$	−0.2	−0.0050
Co_2FeSi	−0.3	−0.0060

in high purity metals, is a positive quadratic dependence on the applied field. This effect—caused by the Lorentz force acting on the charge carriers—is suppressed in the Heusler samples at hand due to a short electron mean free path [169]. The "anomalous" linear decrease is observed in magnetically ordered samples. In the case of conventional ferromagnets, the behavior is explained with a suppression of spin disorder scattering. As discussed in the previous section, this is the main source of electrical resistance in these materials. The application of an external magnetic field forces the spins back into a parallel configuration and thus enlarges the mean free path between electron-magnon scattering events. Since the amount of spin disorder increases with higher temperatures, the resistivity decrease becomes more pronounced.

Again, this interpretation of the high-field behavior as a consequence of spin disorder reduction signifies a spin polarization of less than 100 %. Comparison with experimental data for elemental ferromagnets [171] shows an effect of similar magnitude, in contrast to the resistivity anisotropy. Unfortunately, as for the zero-field resistivity, theoretical descriptions of this phenomenon are only fragmentary. It was already discussed that the spin disorder picture relies on a simplified model of the electronic structure. A more detailed model is presented in reference 171, but it depends on a large number of parameters, for example the effective masses of s and d electrons. Most of these quantities are known neither theoretically nor experimentally for the Heusler compounds. It is therefore not possible to quantify the electronic properties in this case. Additionally, no comparative studies on the general magnetoresistive behavior of half-metals exist.

For laser deposited $Co_2Mn_{1-x}Fe_xSi$ films, a similar picture emerges. Both the low-field anisotropy and the linear high-field decrease of the Ohmic resistivity are also present in these samples. Thus, the same conclusions drawn for the sputtered samples apply here as well. It can, however, be seen from table 4.1 that the magnitude of the effects varies with stoichiometry. The values tend to be somewhat

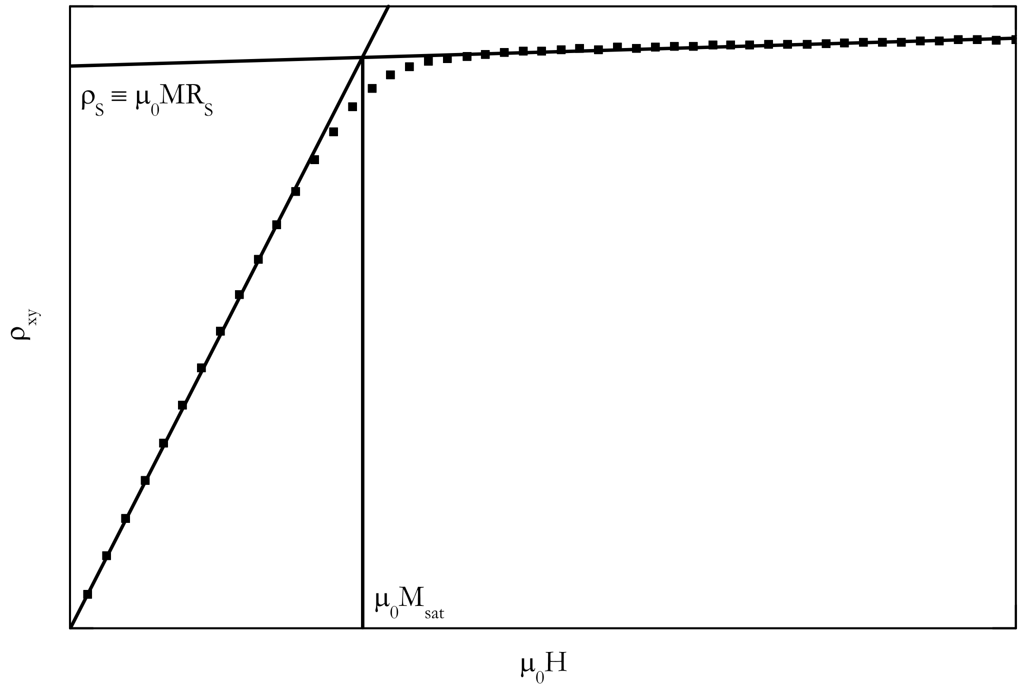

Figure 4.8: Schematic behavior of the Hall resistivity in a ferromagnet.

smaller for the intermediate compounds. This might indicate a higher spin asymmetry in these cases, as expected from band structure calculations.

4.4 Hall Effect

In a nonmagnetic metal the Hall resistivity ρ_{xy} shows the well-known linear dependence on the magnitude of an applied magnetic field. This "normal" Hall effect is caused by the Lorentz deflection of the conduction electrons. In ferromagnets there appears a second "anomalous" Hall effect, as illustrated in figure 4.8. This ferromagnetic contribution causes a steep linear increase of the resistivity until magnetic saturation is reached. The total dependence on the external field is then empirically described as the sum of these contributions:

$$\rho_{xy}(B,M) = R_0 B + \mu_0 R_S M \equiv R_0 B + \rho_S. \tag{4.4}$$

Here the slope of the high field evolution is given by the accustomed normal Hall coefficient R_0. The anomalous Hall coefficient R_S is obtained by extrapolating the normal branch to $\mathbf{H} = 0$, M denotes the magnetization perpendicular to the film surface.

The traditional interpretation of the normal Hall coefficient is based upon the Drude model of metals. This assumption of a classical electron gas results in the relation $R_0 = 1/ne$. Upon closer inspection, this dependence of the normal Hall effect exclusively on the average charge carrier density holds only in special cases. One possibility occurs in the case of an uncompensated metal, if the condition $\omega_C \tau \gg 1$, with the cyclotron frequency ω_C and the collision time τ, is fulfilled [172]. This classical high-field limit—i. e. additionally the condition $\hbar\omega_C < k_B T$ is met—can be reached with clean samples at low temperatures and high fields. Under these circumstances, impurity scattering is a negligible perturbation compared with the influence of the magnetic field.

For the films investigated in this work, a different situation is present. Here the samples satisfy the condition $\omega_C \tau \ll 1$. In this low-field limit, the time between collisions is small compared with the time needed to complete a cyclotron orbit. In this case the traditional interpretation of R_0 is problematic [172]. For a more precise description of the low-field Hall effect, the Boltzmann transport theory is employed [153]. In its original formulation, it treated Boltzmann-distributed gases of classical particles. This method can be extended to weakly coupled, weakly disordered quantum mechanical systems, where excitations can still be treated as wave packets. For a high degree of disorder—when the mean free path is smaller than the extent of a wave packet—localization effects will occur, which cannot be described within this formalism. An example for this deviation is the electronic transport in the nanocrystalline Heusler films presented in the preceding section.

The Boltzmann equation is a differential equation which balances different external influences on the electron distribution f. External fields drive the electrons away from their equilibrium distribution f^0. This is counteracted by scattering processes. Neglecting other contributions, the Boltzmann equation can be written as

$$-e\mathbf{E} \cdot \mathbf{v} \frac{\partial f_k^0}{\partial \varepsilon_k} = \left(-\dot{f}_k\right)_{\text{scatt}} + \frac{e}{\hbar} (\mathbf{v} \times \mathbf{B}) \cdot \frac{\partial f_k}{\partial k}.$$

Solving this equation [153] yields the seemingly familiar relation

$$E_y = -\rho_{xy} j_x = -R_0 B_z j_x,$$

if $\mathbf{B} \perp \mathbf{j}$. However, in contrast to the kinematic Drude theory the Hall coefficient is no longer simply proportional to $1/ne$. Instead, it is given by [172]

$$R_0 = \frac{e^3}{4\pi^3 \hbar} \int \left\{ \tau^2 (\mathbf{k}) \left[v_x^2 M_{yy}^{-1} - v_x v_y M_{xy}^{-1} \right] \right\} \frac{dS_F}{v} \cdot \rho_{xx}^2. \tag{4.5}$$

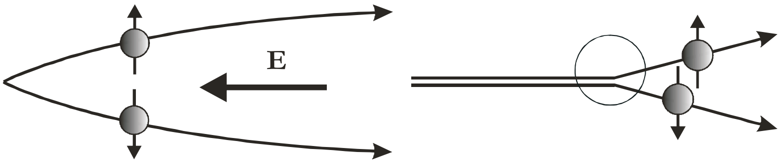

1. Intrinsic effect 2. Skew scattering

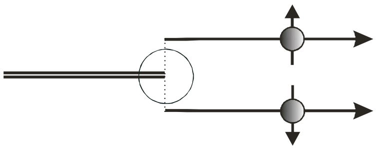

3. Side-jump

Figure 4.9: Illustration of the main contributions to the anomalous Hall effect.

This equation shows that the traditional interpretation of the Hall coefficient is in many cases an oversimplification. Instead, the Hall voltage is governed by the anisotropic scattering time τ as well as the area and the curvature of the Fermi surface, contained in the effective mass tensor M_{xy}. The classical interpretation is regained if effective mass and scattering time are isotropic [172].

Equation (4.5) poses a serious challenge for the interpretation of the normal Hall effect. It is difficult to obtain the necessary values either experimentally or theoretically. Nevertheless, it could be shown in some cases that parameters obtained from *ab initio* calculations [173] or angular resolved photoemission spectroscopy [174] yield the same normal Hall coefficients as the corresponding transport experiments.

The anomalous contribution to the Hall effect in ferromagnets is only indirectly connected to the external field. The increase of the magnetic field causes a growth of the sample magnetization until saturation is reached. As indicated in figure 4.8, the anomalous contribution is clearly dominant over the normal Hall effect. It is therefore obvious that the change in **B** due to the alignment of the magnetic domains cannot be the main source of the low-field increase of the Hall voltage. Additionally, the magnitude of the anomalous resistivity shows a strong temperature dependence, which is absent in the normal Hall effect.

Experimentally the proportionality between the anomalous Hall effect and the sample magnetization was recognized early. On the other hand, the microscopic origin of the proportionality factor R_S has been the source of major controversies [175] and is still not fully understood today. Historically three distinct contributions have been postulated that sum up to the total anomalous Hall effect: an intrinsic effect, and the extrinsic "skew scattering" and "side-jump" mechanisms. All three sources originate from the presence of spin orbit interaction. The differences lie in the details of the coupling mechanisms and their theoretical treatment. The processes are sketched in figure 4.9.

The intrinsic contribution was proposed by Karplus and Luttinger in the earliest attempt to explain the origin of the anomalous Hall effect [176]. As its name implies, the effect is determined entirely by the interaction of the conduction electrons with a perfect crystal. The spin orbit coupling between the periodic crystal potential and the exchange-split conduction electrons was identified as the source of the effect. Treating the applied electric field as a perturbation of the Hamilton operator yields a nonvanishing asymmetrical “anomalous electron velocity” perpendicular to both **B** and **E**. This model predicts a quadratic dependence of the anomalous Hall coefficient on the Ohmic resistivity. A finite resistivity in a periodic crystal can exist here because of the presence of a magnetic vector potential, which lifts the periodicity of the Hamiltonian [177].

The main criticism with the intrinsic theory has been the negligence of impurity scattering. An external mechanism has been first proposed by Smit [178, 179]. Here the conduction electrons are assumed to form simple Bloch bands without intrinsic spin orbit coupling. The source of the anomalous Hall effect is a localized, asymmetric spin orbit interaction with the lattice defects. Since impurity scattering is the source of the anomalous voltage, the extraordinary Hall coefficient should be linearly dependent on the Ohmic resistivity. In contrast to the quantum mechanical treatment by Karplus and Luttinger, the calculations here were performed within the Boltzmann formalism.

A second external mechanism was identified by Berger [180]. Here the spin orbit coupling between impurity atoms and conduction electrons is the source of a lateral displacement of the electron wave package—the so-called side-jump. Although the origin of this process is again an interaction with impurities and although the transport properties are again calculated within the Boltzmann formalism, the anomalous voltage is independent of the defect concentration, resulting in $R_S \propto \rho_{xx}^2$.

The experimental situation has been equally unsatisfying. To begin with, it is not possible to distinguish the intrinsic from the side-jump effect in DC Hall experiments due to their identical dependence on ρ_{xx}. Actual measurements of magnetically ordered systems did show a power law behavior. The reported exponents had values between 1 and 2 [172, 178, 181].

In order to clarify the situation, in recent years an attempt toward a unified theory of the anomalous Hall effect has emerged. At the heart of this idea is a topological interpretation of the intrinsic mechanism, analogous to the quantum Hall effect [182]. It was shown that a quantum mechanical wave function can acquire a geometrical phase—today known as Berry’s phase—if it evolves adiabatically on a

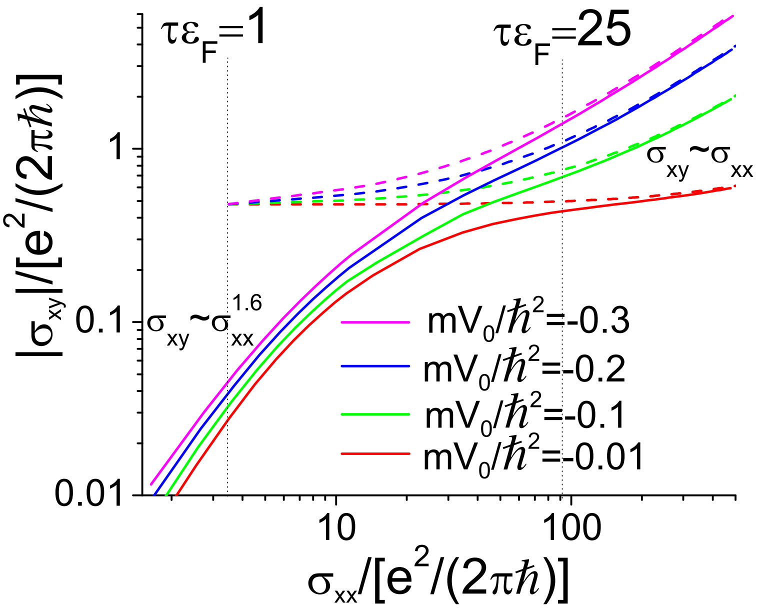

Figure 4.10: Scaling behavior of the anomalous Hall conductivity [186] in the presence of an attractive impurity potential. The solid lines represent numerical, the dashed lines analytical results.

closed path in the parameter space of a Hamilton operator [183]. Within this formalism, it was demonstrated that the Hall conductivity of a 2-dimensional electron gas can be expressed in terms of the "Berry curvature" in momentum space.

Starting from these results, the topological concept was extended to magnetically ordered solids. It could be shown for these systems that a Berry phase is accumulated from the quasiparticle movement on an exchange-split Fermi surface [184]. At this point, the question arises in what way the appearance of this geometrical phase can be the source of the measurable anomalous Hall effect. The physically most transparent picture is an extension of the semiclassical theory of transport [185]. In this case, the Berry curvature in momentum space appears as an additional velocity term in the equations of motion. In ferromagnets this term is identical to the "anomalous velocity" contribution found by Karplus and Luttinger. However, at this point the intrinsic contribution still needs to be viewed as a separate source of the anomalous voltage.

More systematic but less intuitive results could be obtained with rigorous approaches based on Green's function techniques [187, 188]. These formalisms were applied to several simplified models, most notably the ferromagnetic Rashba Hamiltonian [189]. Despite its simplicity, it contains all relevant properties of a real fer-

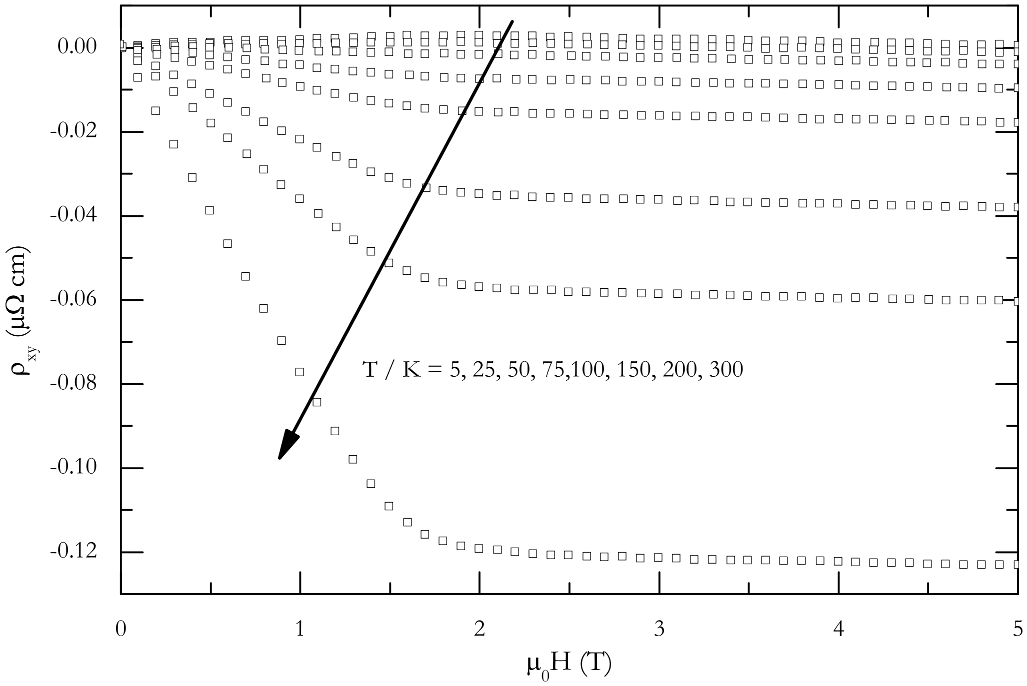

Figure 4.11: Hall resistivity of a sputtered Co_2FeSi sample.

romagnet. The main result is a transition between different scaling regions, depending only on the diagonal resistivities of the respective materials, as illustrated in figure 4.10. The linear skew scattering behavior should be observed in ultraclean materials[1]. In an intermediate region the anomalous Hall effect is dominated by the intrinsic mechanism, the side-jump is claimed to be suppressed by two orders of magnitude. A third, hitherto disregarded scaling behavior is proposed for dirty materials. A lifetime broadening of the quasiparticle energies results in $\rho_{xy} \propto \rho_{xx}^{1.6}$. Figure 4.10 was obtained for a two-dimensional Rashba system. However, it is believed that these results also apply for real three-dimensional ferromagnets, if instead of the conductivity the conductivity per lattice constant is considered. A comparison of this predicted generalized behavior with several experimental publications for different materials [190] seems to back up this hypothesis (see also figure 4.17 on page 88).

---

[1] Please note that in this figure as well as in figures 4.17 and 4.18 σ_{xy} has been defined by the authors as the zero-field extrapolation of the normal Hall conductivity, and not as the experimental Hall conductivity. In this work σ_S will be used for the extrapolated values—analogous to the definition of the anomalous Hall resistivity in equation (4.4).

The experimental findings for sputtered Co_2FeSi samples are presented in figure 4.11. The normal Hall coefficient has a value of $R_0 = -8.4 \cdot 10^{-4} \mu\Omega\text{cm/T}$ and is independent of sample temperature. Assuming an isotropic one-band system, this corresponds to a charge carrier density of 33 electrons/f.u. Since this value is larger than the valence electron count per formula unit, it can be concluded that this picture is too simple. As a next step, an isotropic two-band model can be applied to this problem. If the charge carriers of these subsystems have opposite signs, the two Hall contributions will cancel out each other. The Hall coefficient is then given by [172]

$$R_0 = \frac{1}{n^* e} = \frac{\mu_+^2 n_+ - \mu_-^2 n_-}{(\mu_+ n_+ + n_- \mu_-)^2} \frac{1}{e}. \tag{4.6}$$

Equation 4.6 shows that even in this rather simple case the effective charge carrier density n^* is no longer dependent solely on the individual charge carrier concentrations $n_\pm$ but also on their mobilities $\mu_\pm$. A more quantitative analysis of this situation will be presented below for the laser ablated samples. For now, it suffices to notice that the shallow slope of the normal Hall effect hints toward a complicated multiband system with contributions from both electron- and hole-like charge carriers.

The anomalous Hall effect shows an unusual behavior: In most cases, the anomalous coefficient R_S approaches a minimum absolute value for sample temperatures close to zero, since the electron-phonon scattering rate and with it the diagonal resistivity diminishes. Here on the other hand, the anomalous resistivity changes its sign at approximately 50 K and increases again in magnitude if the sample is cooled further down. Similar characteristics have been seen only in a few cases [191–193].

The most straightforward explanation of this behavior is the presence of two separate scattering mechanisms. The first one causes a small, temperature independent and positive contribution. The second one is the source of a negative AHE. It is strongly temperature dependent and vanishes at low temperatures. The nature of this second contribution can be deduced from figure 4.12. Here the anomalous Hall coefficient R_S is plotted as a function of the Ohmic resistivity. The linear dependence suggests that the temperature dependent contribution is caused by an extrinsic skew scattering mechanism. The origin of the positive effect is at this point difficult to determine. As with the normal Hall effect, its nature will be discussed in the following presentation of the laser ablated $Co_2Mn_{1-x}Fe_xSi$ series.

The field dependence of the Hall effect in pulsed laser deposited Co_2FeSi samples is illustrated in figure 4.13, the behavior of the whole alloy series is presented in figure 4.14. The normal Hall coefficient of Co_2FeSi effect stays qualitatively unchanged. A somewhat steeper slope corresponds to an effective charge carrier con-

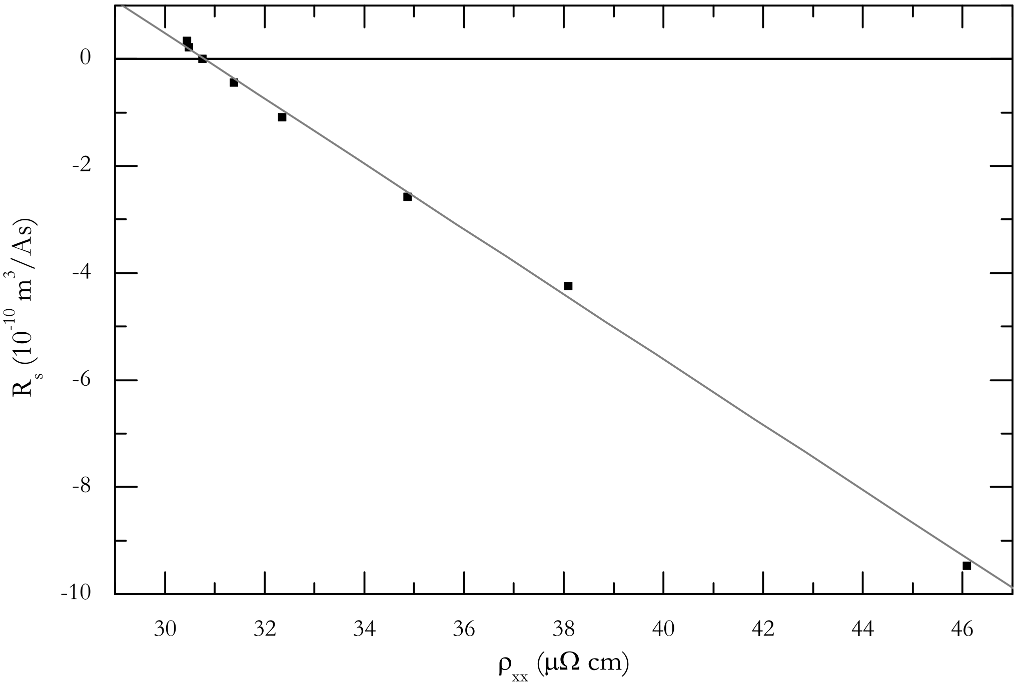

Figure 4.12: Dependence of the anomalous Hall effect on the sample resistivity. In order to compensate for the changing sample magnetization, the plot shows the evolution of the anomalous Hall constant instead of the Hall resistivity. The values were obtained by extrapolation of the high-field data of figure 4.11. The gray line represents a linear fit of the data points.

centration of 25 electrons/f.u. In addition, the small positive anomalous signal at low temperatures seems to be consistent with the sputtered samples. The temperature dependence of the anomalous Hall effect shows a clearly differing behavior. It increases with higher temperatures, the anomalous voltage therefore remains positive over the complete investigated temperature region. Taken together, the anomalous effect now apparently behaves as in most other ferromagnets. A closer inspection, however, shows that this similarity might be a coincidence. Figure 4.15 shows a plot of $R_S\left(\rho_{xx}\right)$ analogous to figure 4.12. From the Co_2FeSi data it can be seen that for $\rho_{xx} \to 0$ the anomalous effect can be extrapolated to a large negative value. So *mathematically* there exists a nonvanishing R_S at zero resistivity in both sputtered and laser ablated Co_2FeSi films. For most other ferromagnets reported in literature, this extrapolated value is close to zero. But although it seems possible that this transition could be observed in cleaner laser ablated samples, it must be stressed here that no such transition was observed experimentally.

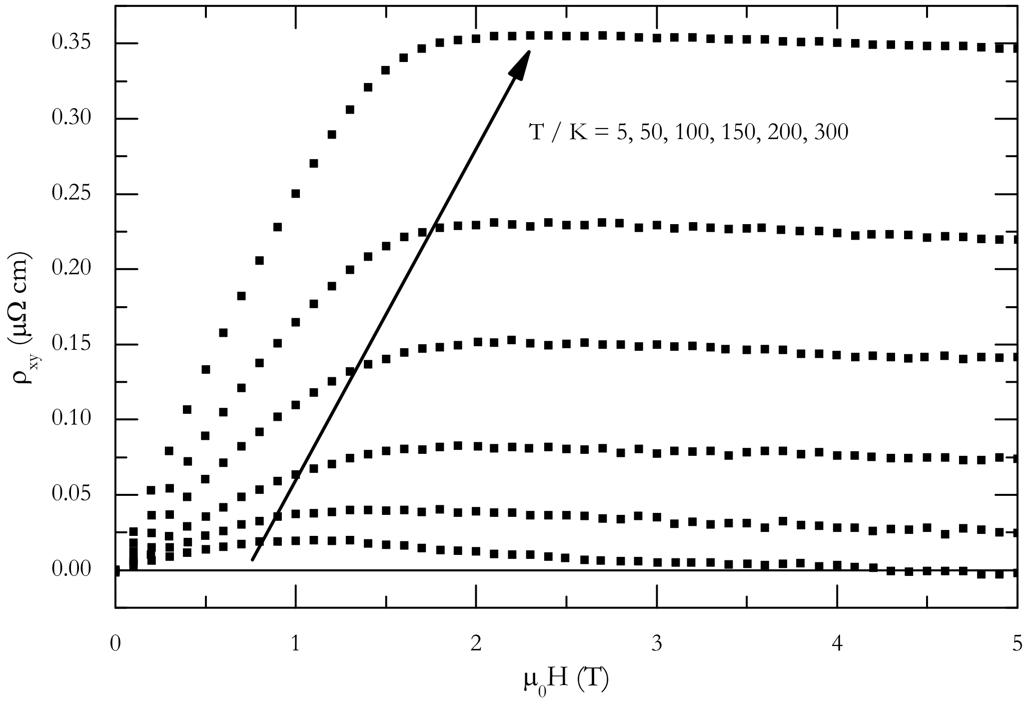

Figure 4.13: Temperature dependent Hall resistivities for a laser ablated Co_2FeSi film.

In order to explain this discrepancy between the observations in sputtered and laser ablated samples, the presence of two temperature independent scattering mechanisms is proposed. These two unequal channels are caused by different types of impurity or intrinsic scattering, which result in anomalous voltages with opposing sign. Their relative contributions are different in the two types of Co_2FeSi films. Therefore, the low-temperature AHE can be positive or negative, resulting in the observation or absence of a sign change.

As mentioned earlier, the small and negative slope of the normal Hall effect indicates a partial compensation of hole-like and electron-like sheets of the Fermi surface, with a preponderance of the electron contribution. In figure 4.14 it can be seen that with increasing Mn content the absolute value of the normal Hall coefficient decreases even further and assumes the opposite sign for the Mn rich compounds. The positive slope of the Co_2MnSi data yields $n^* \approx 5$ holes/f.u. At first glance, this is a somewhat surprising behavior. The system Co_2MnSi has 29 valence electrons, which constitute nearly filled bands. The valence electron count of Co_2FeSi is 30, being even closer to a completely filled shell. From this argument, a more hole-like behavior in Co_2FeSi is to be expected.

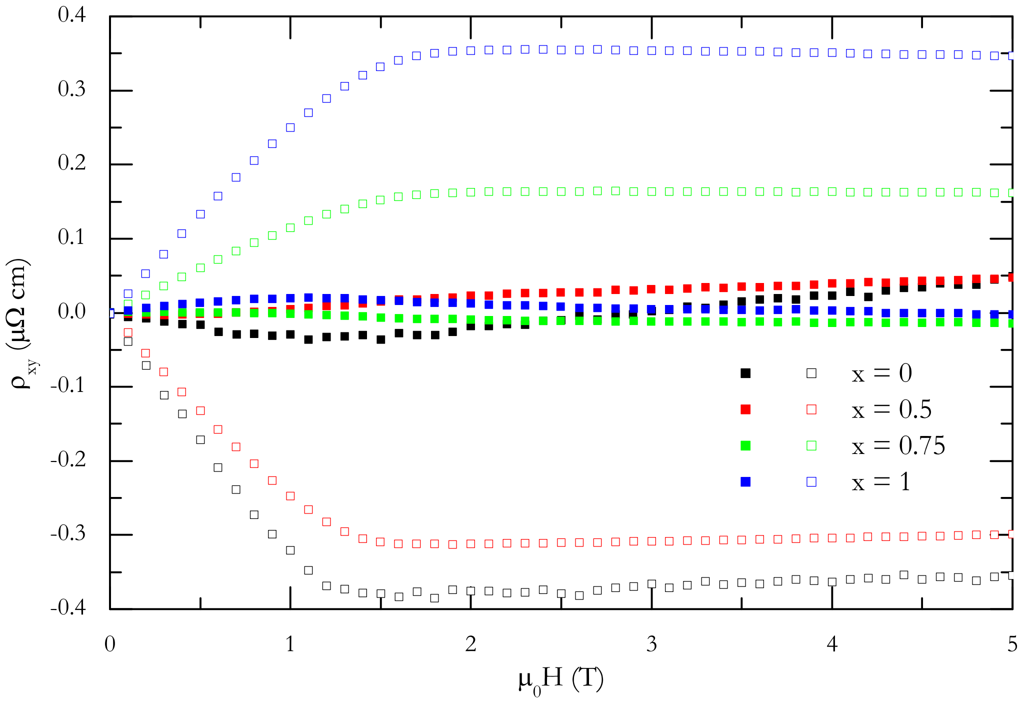

Figure 4.14: Temperature dependent Hall resistivities for laser ablated $Co_2Mn_{1-x}Fe_xSi$ films. Full (open) symbols represent data at 5 K (300 K).

For a more substantiated understanding of the normal Hall effect, the data is compared with calculations of the electronic structure as shown in figure 4.16. They have been generated with the LSDA+DMFT technique presented in section 1.3. The same parameters that have already been used to calculate the integrated density of states (figure 1.4) and the magnetic properties (figure 1.5) of $Co_2Mn_{1-x}Fe_xSi$ were employed. The left hand part shows the band dispersions near the Fermi energy from the center of the Brillouin zone (the Γ point) along the [110] direction to the M point at the edge of the Brillouin zone. The right hand side of the image shows planar cuts through the Fermi surfaces, perpendicular to the [100] direction.

For the case of Co_2MnSi—shown in the top part of figure 4.16—it can be seen that at the center of the Brillouin zone both majority and minority bands are located above the Fermi energy . They cross E_F with increasing $|\mathbf{k}|$, which means that the states enclosed by the Fermi surface are unoccupied. Therefore, the sheets of the Fermi surface have hole-like character [194]. For $Co_2Mn_{0.5}Fe_{0.5}Si$, the minority states are shifted completely below the Fermi energy—it is a true half metal. Again, the majority states are occupied outside of the Fermi surface, indicating predom-

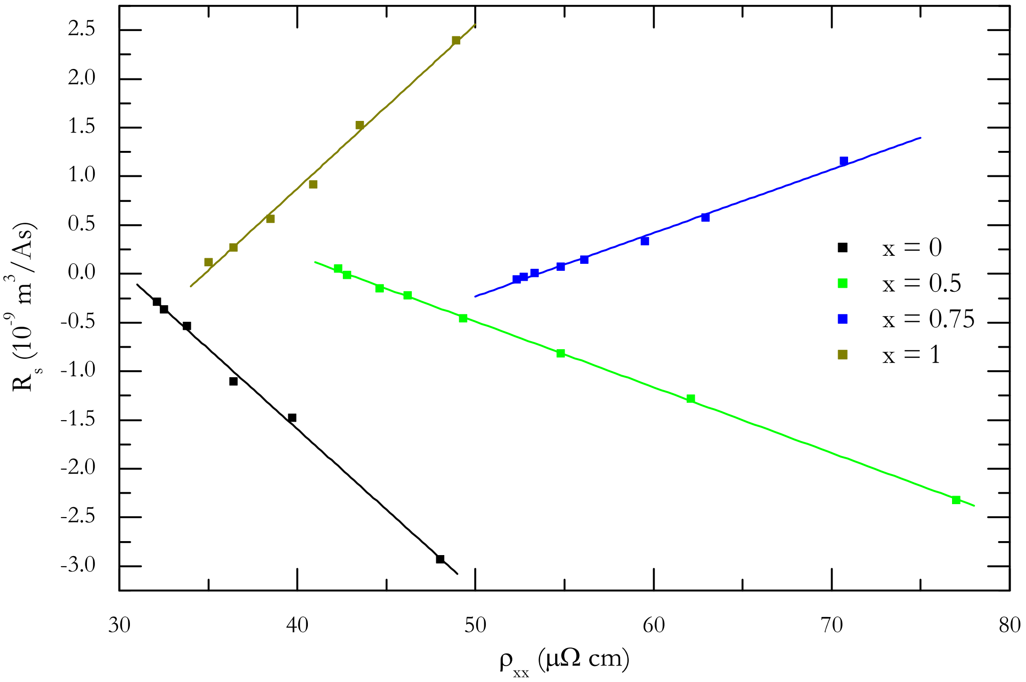

Figure 4.15: Anomalous Hall coefficients of $Co_2Mn_{1-x}Fe_xSi$ plotted against resistivity. Straight lines indicate linear fits.

inantly hole like charge transport. In the final case Co_2FeSi, the minority bands cross the Fermi level near the M point. Again, the states with higher $|\mathbf{k}|$ values are occupied. However, in this situation the curvature of the minority Fermi surface and therefore the orientation of motion is opposed to the previous cases. These states therefore have electron like behavior. If additionally the local properties of the Fermi surfaces are considered, it can be seen that the asymmetry of the majority surface increases with higher Fe content, resulting also in an increase of the electron like contribution.

The calculated cases therefore show qualitative agreement between theory and experiment. This is most obvious for the minority states, which evolve from holes in Co_2MnSi to electrons in Co_2FeSi. With the calculations available at present, it is difficult to gain a more detailed interpretation. As shown in equation (4.5), the effective mass tensor has to be known, i. e. the second derivatives $\partial^2\varepsilon\left(\mathbf{k}\right)/\partial k_i \partial k_j$ have to be calculated. This task has yet to be performed.

According to the respective theories, all anomalous scattering mechanisms are dependent on the sign of the charge carriers. The change from hole like to electron like transport should therefore also be reflected in a corresponding change of

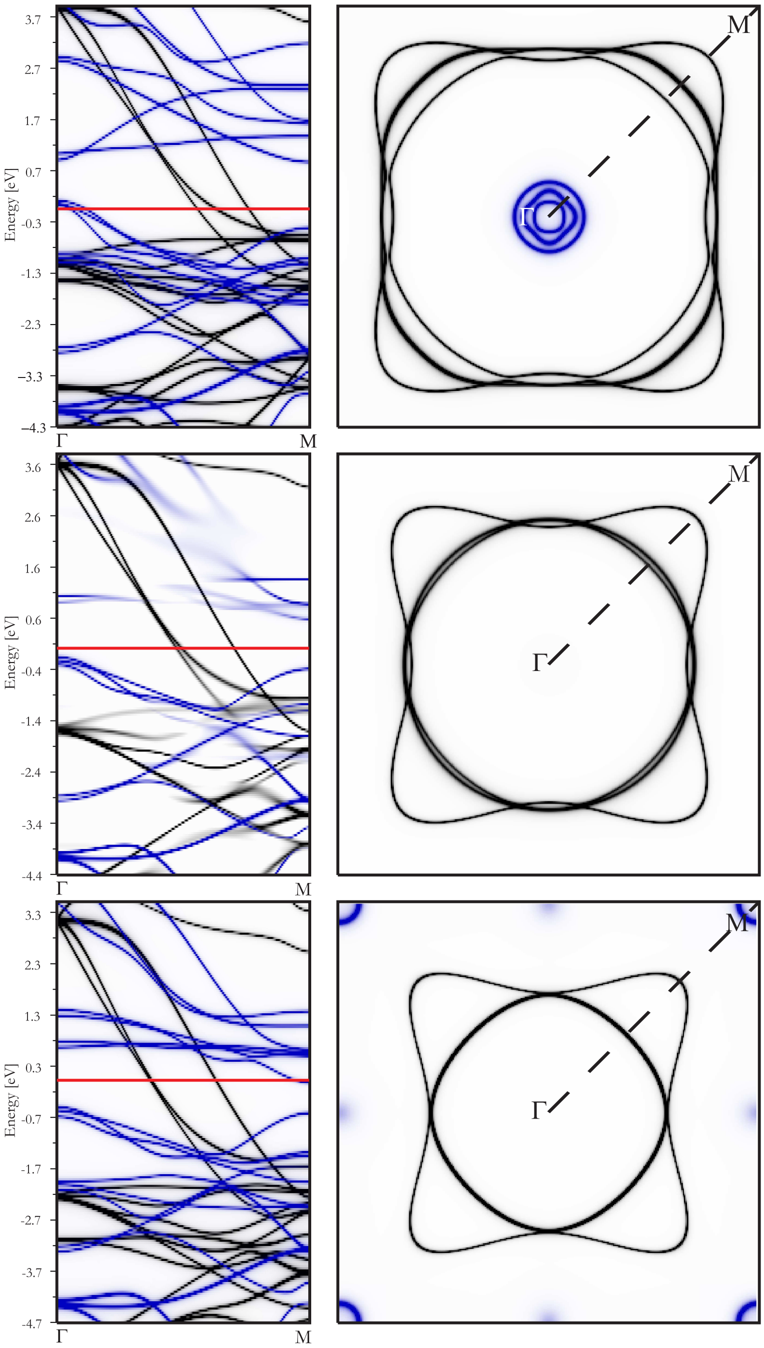

Figure 4.16: Dispersion relations (left) and Fermi surfaces (right) of Co_2MnSi (top), $Co_2Mn_{0.5}Fe_{0.5}Si$ (middle), and Co_2FeSi (bottom). Black lines correspond to majority states, blue lines to minority states.

R_S in $Co_2Mn_{1-x}Fe_xSi$. It can indeed be seen in figures 4.14 and 4.15 that both the temperature dependent contribution and the extrapolated anomalous coefficient reverse their behavior accordingly. It is also eye-catching that in the intermediate compounds a sign change of the anomalous Hall effect is observed—analogous to the sputtered Co_2FeSi films. This reversal is absent in the ternary compounds. This supports the hypothesis of two temperature independent contributions. Not only they seem to be affected by disorder in one compound, as demonstrated with the sputtered and laser ablated Co_2FeSi samples. The results obtained for the quaternary series suggest that the same effect can also be manipulated by doping.

It is now discussed how the observed scaling behavior performs in comparison with the topological theory of the anomalous Hall effect. Figure 4.17 shows a plot of the anomalous Hall conductivity as a function of σ_{xx} for a number of materials [190], which seem to follow the predicted behavior reasonably well. In contrast, the inversion of the experimental resistivities gathered in this work result in a strongly deviating behavior. Instead of showing a constant anomalous conductivity as expected for the observed Ohmic resistivity, σ_S decreases by approximately two orders of magnitude with increasing conductivity.

Mathematically, this difference is caused by a large value of $R_{S0} = R_S\left(\rho_{xx} \to 0\right)$. It is shown in appendix B that in the absence of this contribution R_S and ρ_S can be described with $\alpha\rho_{xx}^{\beta}$. Then it follows that $\sigma_S \propto \sigma_{xx}$ for $\beta = 1$ and $\sigma_S = \text{const.}$ for $\beta = 2$. These relations are indeed observed in materials with small values of R_{S0}. This behavior changes drastically if R_{S0} is large. It is also shown in appendix B that in this case the skew scattering mechanism results in an anomalous conductivity with a positive linear and a negative quadratic term.

These calculated functions are plotted in figure 4.17 as thin black lines. The Hall data gathered in this work lies on the negative quadratic branch, extrapolation to higher impurity concentrations seems to be more in line with the general Hall behavior. In this context it is also noteworthy that in figure 4.17 a similar downturn of the Hall conductivity might be present in $La_{1-x}(Sr,Ca)_xMnO_3$ and Co. Since figure 4.17 is a plot of the absolute value of the anomalous conductivity, all Heusler samples investigated in this work show a qualitatively similar behavior. It does not matter whether the anomalous conductivity is positive or negative or whether a sign change is actually observed.

The most plausible explanation for the observed behavior was given in a very recent paper, which looks in more detail into the effects of impurities on the anomalous Hall effect [186]. The authors use in principle the same calculational techniques as in older works. With the same parameters they obtain similar results—for example figure 4.10 was taken from the article under discussion. These results were obtained with the assumption of an attractive impurity potential. However, there

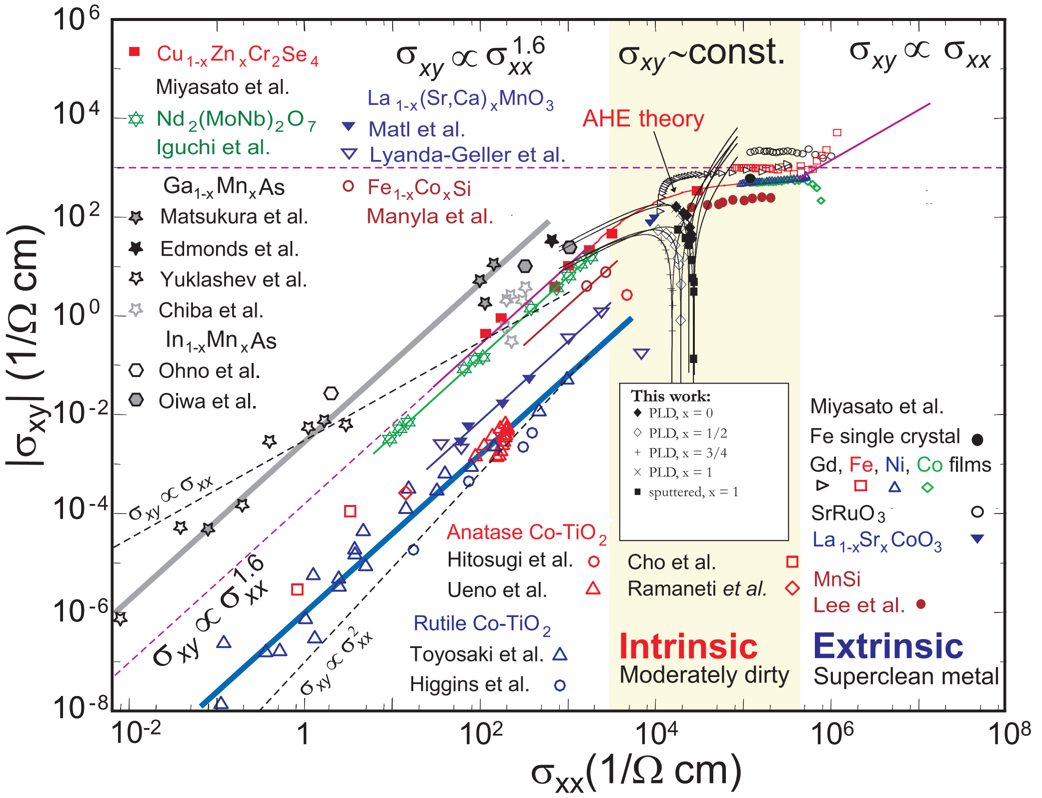

Figure 4.17: Empirical scaling behavior of the anomalous Hall conductivity and comparison with theoretical predictions. In addition to the findings reported in reference 190 this plot also contains the experimental data obtained in this work. The data points of the laser ablated samples are the same as in figure 4.15, the data of the sputtered sample are the same as in figure 4.11. The black solid lines are inversions of the linear fits in the respective figures. The functions were calculated according to equation (B.7) on page 114. Please note that the vertical lines separating the different scaling regions are not identical to figures 4.10 and 4.18.

are no reasons why the potential needs to be necessarily negative. Therefore, in figure 4.18 the calculated results for repulsive impurity potentials are presented.

A comparison with the experimental data shows good agreement. Hence, in the Heusler compounds under investigation it seems that the intrinsic mechanism and the skew scattering have opposing effects on the anomalous Hall voltage. The increase of the latter effect leads in some cases even to an observable change of sign. In the double logarithmic plots of figures 4.17 and 4.18 they appear as cusps in the graphs. These findings confirm the conclusions drawn already in the discussion of figure 4.12. At that point, the nature of the temperature independent contribution was left open. It can now be seen that it is of intrinsic origin, caused by the Berry curvature of the Fermi surface. The scaling behavior of other samples that show a sign reversal of the anomalous Hall coefficient [191, 192, 195] seems also to be in line with the predictions of reference 186.

Even though it seems that the experimental data can be adequately described by the presence of a repulsive impurity potential, the limitations of the theoretical model as well as the experimental techniques have to be envisioned. First, it has to be discussed whether or not the Rashba model is expandable to three-dimensional ferromagnets. The published calculations require a spin orbit interaction energy that is at least of the same magnitude as the exchange energy. This is in contradiction to the situation in both conventional ferromagnets and Heusler compounds [196, 197]. In the Rashba model, this would lead to a strong suppression of the intrinsic effect. On the other hand, calculations for bcc iron suggest that the absence of a strong spin orbit coupling might still result in a large contribution from the Berry curvature [198].

Furthermore, the theoretical models—historical and contemporary alike—consider the effect of changing impurity concentrations on the Hall effect at low temperatures. The influence of electron-magnon or electron-phonon scattering at high temperatures has not been investigated thoroughly. So far it seems that these inelastic interactions lead to a T^2 behavior of the anomalous Hall effect [199, 200]. However, it is unclear if this applies for the $Co_2Mn_{1-x}Fe_xSi$ system, because investigations were carried out well below Curie and Debye temperature. It is also obvious from the rather small resistivity change of a factor of approximately 1.5 between liquid helium and room temperature that at 300 K impurity scattering still dominates over the inelastic processes.

On the other hand, also the investigation of the scaling behavior by doping with impurities is problematic. Figures 4.17 and 4.18 investigate the anomalous Hall conductivity. As for the anomalous resistivity, this value is also dependent on the sample magnetization. This implies that even though by doping the Ohmic resistivity is increased by several orders of magnitude, the band structure and the magnetiza-

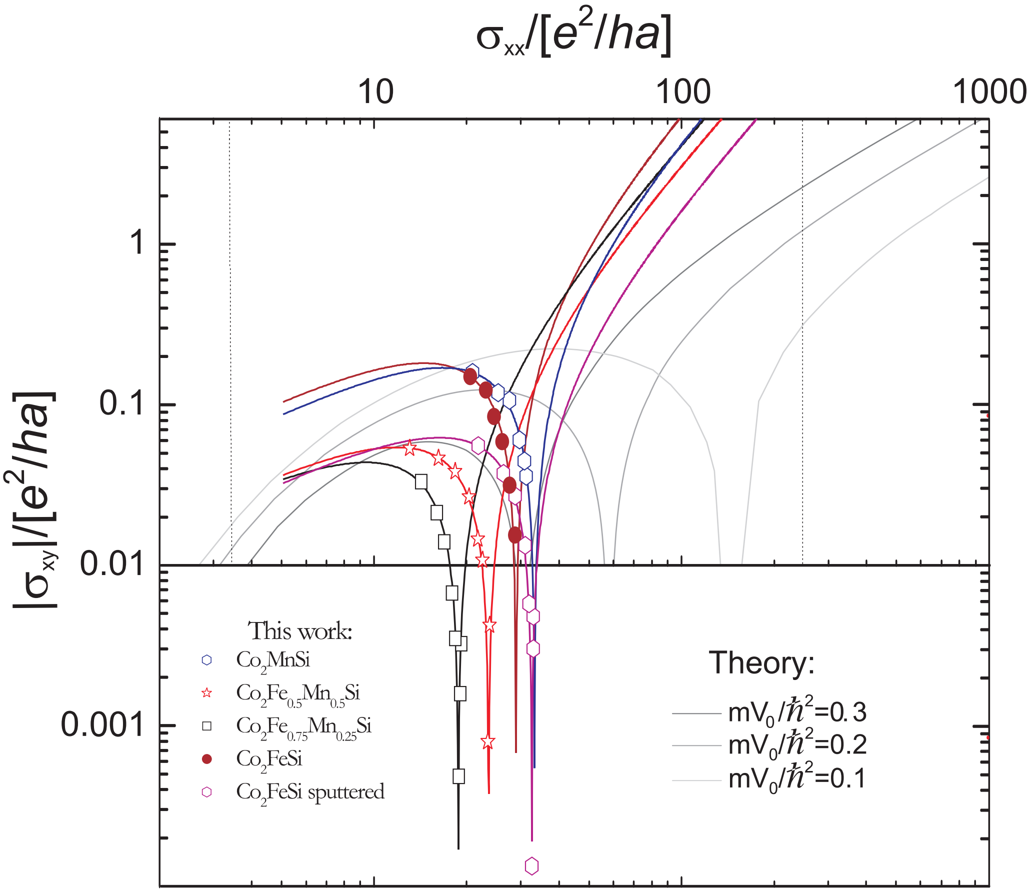

Figure 4.18: Scaling behavior of the anomalous Hall conductivity in the presence of a repulsive impurity potential. The gray lines represent numerical results from reference 186 for different impurity potential strengths $V_0 > 0$. The experimental data (symbols) and the corresponding fits (colored lines) are the same as in figure 4.17.

tion of the samples need to remain constant. From all that is known about Heusler compounds, this approach is not possible.

Finally, it should be kept in mind that the topological models assume *one* intrinsic and *one* skew scattering channel. In the Heusler samples at hand, however, there might exist more than one temperature independent mechanism. Whether they are both of intrinsic nature and caused by different sheets of the Fermi surface cannot be answered at this point. Furthermore, it is unclear what consequences this additional effect has on the total anomalous Hall voltage. The experimental data therefore seem to parallel the model of reference 186, but more research has to be performed in order to draw an unambiguous picture.

Systematic transport experiments performed on $Co_2Mn_{1-x}Fe_xSi$ and comparison with high accuracy band structure calculations allowed the investigation of their electronic properties. The band structure calculations were performed in order to find the position of the Fermi energy with respect to the half-metallic energy gap in the spin minority channel. A systematic shift of the Fermi edge with respect to the minority spin conduction band was found from the calculations. This systematic shift also corresponds to changes of the Fermi surface topology. Calculated cross-sections of the Fermi surfaces show an evolution from a hole-dominated electronic transport for Co_2MnSi to electron-like charge carriers for Co_2FeSi. A change of the sign of the apparent charge carriers in Hall effect measurements is consistent with these band structure calculations. Additionally, the anomalous Hall effect showed the respective changes as well. The total anomalous effect was found to be a superposition of an extrinsic skew scattering contribution and one or more intrinsic contributions. These mechanisms have opposing effects on the anomalous Hall effect and lead in some cases to a sign reversal of the voltage.

CHAPTER 5

FURTHER CHARACTERIZATION

In the previous chapters, the deposition of $Co_2Mn_{1-x}Fe_xSi$ films has been presented. Their structural, magnetic, and transport properties have been discussed. However, the picture drawn from these data is incomplete. Several results could be assessed only qualitatively or have ambiguous interpretations. Therefore, further investigations of these Heusler films have been carried out in collaboration with external research groups. This chapter gives a short account of those experiments relevant to the investigations presented earlier in this work. The results will be discussed with respect to these open questions.

5.1 Kerr Magnetometry

A first glimpse into the anisotropic magnetic properties of Co_2FeSi could be caught with the same magnetometry setup used already in chapter 3. Figure 5.1 shows VSM hysteresis loops of a (110)-oriented Co_2FeSi thin film for different alignments with respect to the external magnetic field. As expected, the angular dependence of the coercitive field in this case shows a uniaxial anisotropy in the film plane. The magnetization data show an easy axis [001] and a hard axis $[1\bar{1}0]$. On the other hand, the same experiment with (100) oriented films failed to detect magnetic anisotropy at all, as shown in the upper part of figure 5.2. This peculiar angular dependence was one of the reasons to extend the investigations to Kerr magnetometry. These experiments were performed by the "AG Magnetismus" at Kaiserslautern University.

If light interacts with a metal, the periodic perturbation of the electrons in the material is the source of the reflected beam [201]. In the presence of a finite magnetic

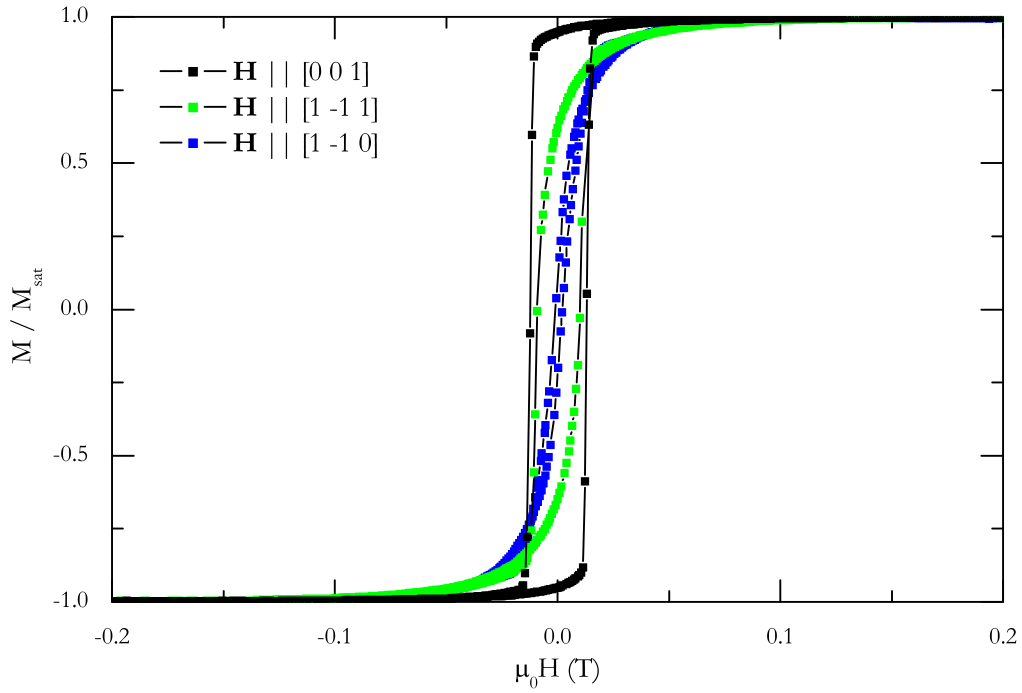

Figure 5.1: VSM hysteresis loops of a Co_2FeSi (110) / Al_2O_3 sample, measured at room temperature.

flux, these electrons experience a Lorentz force perpendicular to their direction of motion. This additional velocity component causes a rotation of the polarization plane. On a microscopic level, this requires the presence of spin-orbit coupled electrons in order to allow interaction between the electrical field of the light and the electron spins. The magneto-optical Kerr effect (MOKE) does not yield absolute magnetization values. Its advantage is the possibility to record hysteresis loops with a high angular resolution. The probing depth in metals is several tens of nanometers. Therefore, like vibrating sample and SQUID magnetometry MOKE probes the bulk properties of the films.

Macroscopically the Kerr effect can be described by magnetization dependent off-diagonal components of the dielectric tensor ε_{ij}. Assuming that the influence of **M** on ε_{ij} is small, the tensor can be expanded [202] as

$$\begin{aligned}\varepsilon_{ij}(\mathbf{M}) &= \varepsilon_{ij}(\mathbf{M}=0) + \left[\frac{\partial \varepsilon_{ij}}{\partial M_k}\right]_{\mathbf{M}=0} M_k + \frac{1}{2}\left[\frac{\partial^2 \varepsilon_{ij}}{\partial M_k \partial M_l}\right]_{\mathbf{M}=0} M_k M_l + \ldots \\ &\equiv \varepsilon_{ij}(\mathbf{M}=0) + K_{ijk}M_k + G_{ijkl}M_k M_l + \ldots\end{aligned} \tag{5.1}$$

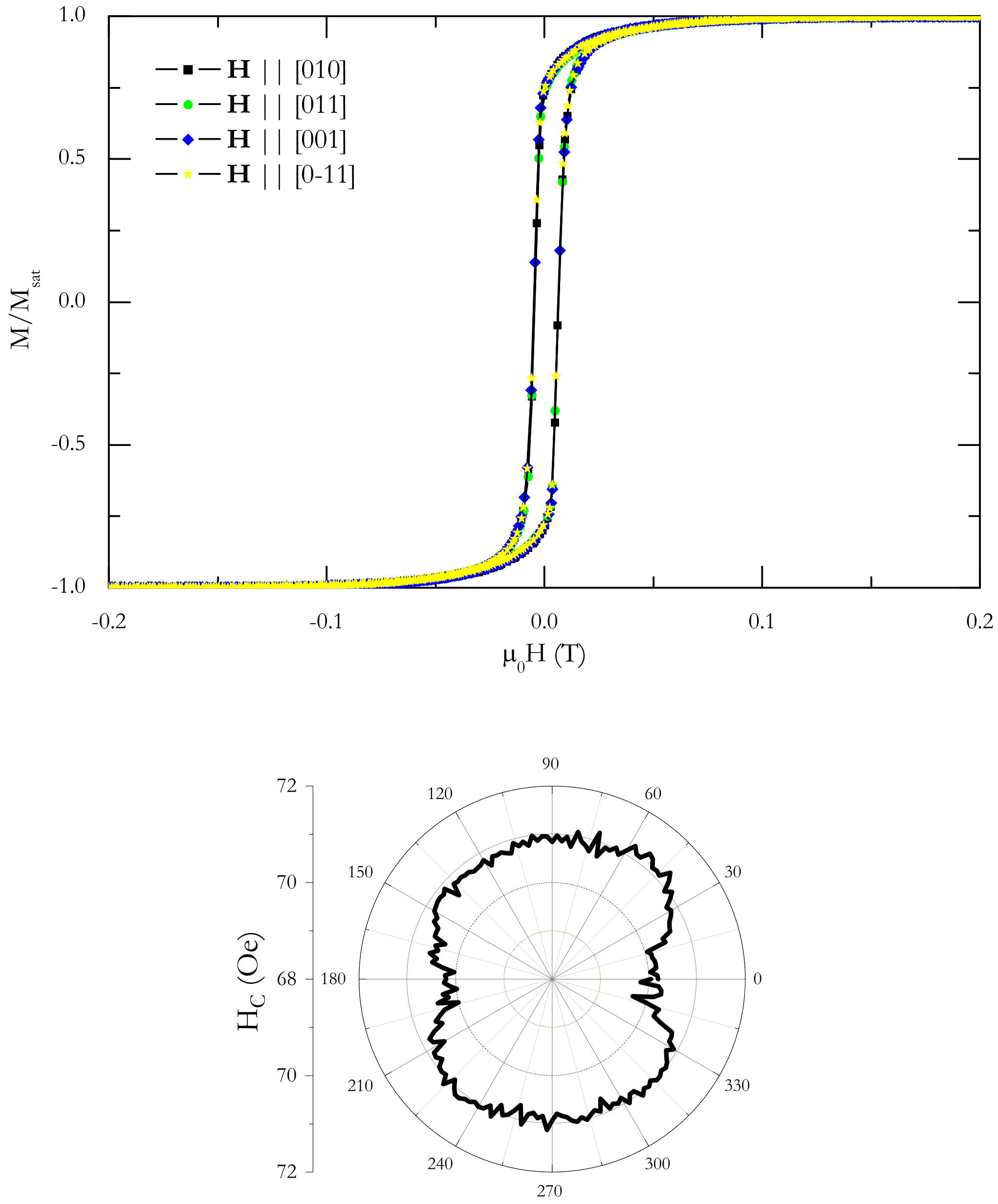

Figure 5.2: Top: Magnetic ansitropy of a Co_2FeSi (100) / MgO sample, measured analogous to figure 5.1. Bottom: Polar plot of the coercitive field, obtained with Kerr magnetometry on the same sample. The polar component denotes the angle α between the [001] film direction and the plane of light incidence (see also figure 5.3.)

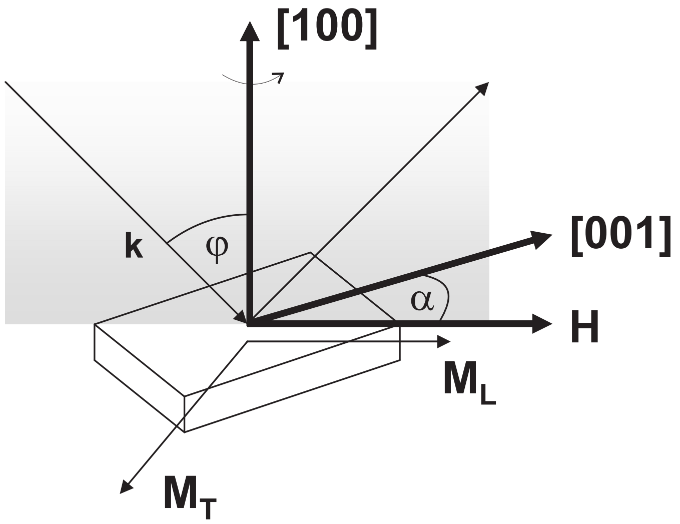

Figure 5.3: Illustration of the longitudinal MOKE geometry.

The data presented here were acquired in the longitudinal MOKE (LMOKE) geometry, as illustrated in figure 5.3: the external magnetic field was applied parallel to the plane of light incidence, the angle between the incident **k**-vector and the film normal was $\varphi = 45$ °. The samples were rotated around the out of plane [100] axis, the value of α denotes the angle between the [001] direction and the plane of incidence. In this geometry, the Kerr rotation is determined by the linear term of equation (5.1), which is proportional to the in plane magnetization component M_{L}.

Microscopically, the LMOKE is caused by the first order spin-orbit interaction energy $E_{\mathrm{SO}} = \mathbf{L} \cdot \mathbf{S}$, causing an energy splitting of the electronic structure [203]. In this case, the LMOKE originates from the part of the electronic structure, where the electron wave vector component **k** is parallel to **M**. It should also be noted that the spin-orbit coupling is also responsible for the magnetocrystalline anisotropy [194], so both effects are closely related.

The lower part of figure 5.2 shows the angular dependence of the coercitive field of the Co_2FeSi / MgO sample. As expected from the VSM data, the plot shows a very weak anisotropy of the coercitive field. The difference between maximum and minimum value is approximately 1 %. What is more surprising is the presence of a weak twofold symmetry instead of the fourfold symmetry expected for a (100)-oriented Heusler crystal.

The data shown in figure 5.2 were obtained from a film with a thickness of 98 nm. Two hysteresis loops corresponding to the same sample are presented on the left hand side of figure 5.4. They reveal another unexpected feature. Although recorded

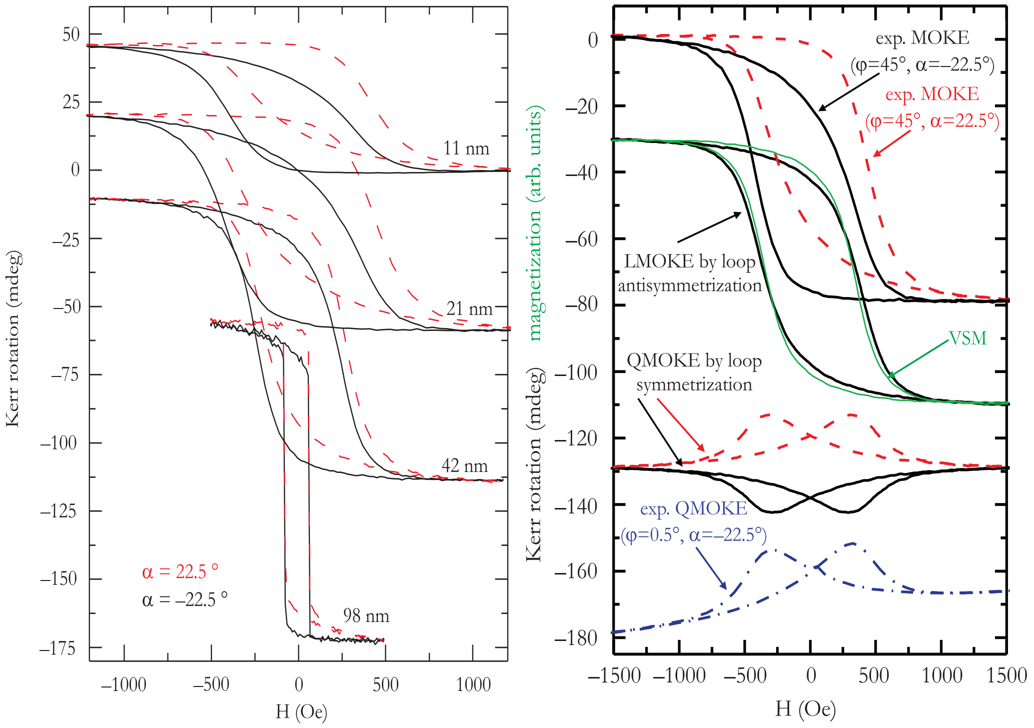

Figure 5.4: Left: MOKE hysteresis loops of Co_2FeSi / MgO films with varying thickness. Right: Kerr effect of the 21 nm thick film. The top loop shows the same raw data as on the left hand side. The next graph shows the LMOKE contribution for $\alpha = -22.5$ °, as determined by antisymmetrization of the experimental loop, and a VSM measurement (scaled to the Kerr data). The third plot shows the QMOKE loop determined by loop symmetrization and the bottom loop the directly measured QMOKE.

along equivalent directions $\alpha = \pm 22.5$ °, it can be seen that these two curves are unequal. Each curve viewed separately is also asymmetrical with respect to field reversal. Additionally, it can be seen in figure 5.4 that this effect is more pronounced in samples with a reduced thickness. As a further complication these asymmetries are not always present, they vanish for example at $\alpha = \pm 45$ °.

Some of these discrepancies between crystal symmetry and magneto-optical properties can be resolved if the second-order term of equation (5.1) is taken into account [204]. As opposed to LMOKE, this quadratic Kerr effect (QMOKE) is caused on a microscopic level from that part of the electronic structure which satisfies $\mathbf{k} \perp \mathbf{M}$. In this situation $\mathbf{L} \cdot \mathbf{S} = 0$, and spin-orbit contributions of order ξ^2 are the dominant source of the Kerr rotation. In contrast to the linear effect, it is an even function of the magnetization. For the latter reason the linear and the quadratic effect can easily be separated by adding or subtracting the respective experimental hysteresis branches.

The decomposition of the Kerr data into even and odd contribution is shown on the right hand side of figure 5.4. The antisymmetrized graph in the second row shows no longer irregularities. Additionally, a comparison with a VSM hysteresis loop of the same sample is presented. It can be seen that these two curves match quite well. It is therefore manifest that the odd contribution is dominated by the linear Kerr effect. In order to check whether or not the even component is actually the QMOKE rotation, the angle of incidence φ was set to nearly zero, as in this experimental configuration LMOKE cancels. The result of such a measurement is presented again in figure 5.4. It is in agreement with the QMOKE contribution obtained from symmetrizing the raw data. The additional linear component visible in the experimental data is an experimental artifact. It results from a Faraday effect induced in the optical elements by stray magnetic fields [205].

These results demonstrate that the observed asymmetries of the magnetization loops are indeed the caused by a combination of linear and quadratic Kerr effect. Further investigations of the angular dependence of the quadratic effect show [205] that the quadratic contribution is minimal for example at $\alpha = \pm 45\ °$, resulting in symmetric Kerr hysteresis loops as mentioned above. The peculiar anisotropy of the coercitive field, however, cannot be resolved. Subtraction of the QMOKE signal does not result in a significant change of the angular dependence of the coercitive field. The 98 nm sample still exhibits a very weak uniaxial anisotropy. Interestingly the thinner films show an equally weak, but fourfold anisotropy. It can therefore be ruled out that this anomalous anisotropy is induced in the films by terraces on the substrates, as proposed for ultrathin Fe films [206]. Another explanation would be the presence of epitaxial strain [207]. But again this would favor anisotropy anomalies in the thinner samples. Additionally, no lattice distortions could be detected. The source of this behavior therefore remains hidden for now.

The presence of the quadratic Kerr effect has been observed not only in the Co_2FeSi samples prepared in this work, but also in other Heusler samples [208, 209], especially in Co_2MnSi thin films [210]. It therefore needs to be assessed how this occurrence relates to the electronic properties of these samples. As mentioned earlier, the QMOKE is connected to terms of second order in the spin orbit interaction energy. This contribution is usually much weaker than the LMOKE.

In Co_2FeSi, the QMOKE is exceptionally pronounced. A maximum amplitude of 30 mdeg was observed in the 21 nm thick sample. At present, this value is the largest quadratic Kerr rotation observed in any material [211]. To put this into perspective: the other Heusler compounds exhibit values between 0.5 and 4 mdeg [208–210], for elemental iron a QMOKE rotation of 5.7 mdeg was reported [204].

However, this isolated value should be taken with a grain of salt, because the Kerr effect is geometry and wavelength dependent. But even if these uncertainties are factored in, a large quadratic effect in Co_2FeSi will likely be retained also under different experimental conditions [212].

One factor in this high absolute value is the presence of a rather large LMOKE rotation. As mentioned above the linear effect is a result of the first order spin-orbit interaction. Therefore, the occurrence of a pronounced LMOKE is generally attributed to a large interaction energy. Van Ek *et al.* compared experimental and calculated Kerr spectra for a number of Heusler compounds [213]. Their work confirms this interpretation in the investigated materials. For systems with a half-metallic band structure and correspondingly small orbital moments the linear Kerr rotation is much less distinct than for compounds with reduced spin polarization [25, 213]. The characteristics of the linear Kerr effect in Co_2FeSi therefore are in line with the conclusions drawn previously in this work. A coupling between the spin and the orbital degrees of freedom is present, and its influence at room temperature is sizeable. However, in order to draw more quantitative conclusions both experimental and calculated Kerr spectra of $Co_2Mn_{1-x}Fe_xSi$ are required.

Apart from the pronounced LMOKE contribution, the large relative magnitude of the quadratic effect is responsible for the absolute QMOKE rotation. The value of the QMOKE amplitude in Co_2FeSi is comparable to the linear effect, whereas in Fe it is 1/10 [214]. Unfortunately, at this time the knowledge of the quadratic Kerr effect is only rudimentary. Calculated Kerr spectra—irrespective of the materials under investigation—only take into account linear spin orbit contributions. Hence, the intrinsic origins of the large effect in Co_2FeSi and the distinctly lower value in Co_2MnSi are unknown. Equally unanswered is the question whether the presence of a quadratic Kerr contribution has any additional effects on the electronic properties.

5.2 Photoemission Spectroscopy

Photoemission spectroscopy has been developed as a powerful tool for electronic band structure determination in solids [215]. It is based on Einstein's interpretation of the photoelectric effect. The famous formula $E_{\text{kin}} = \hbar\omega - E_{\text{B}} - \Phi$ allows the determination of the binding energy of a photoelectron by measuring its kinetic energy, if the photon energy $\hbar\omega$ and the work function Φ are known. Taking into account also momentum and spin conservation, the spin-resolved band structure of a solid may be determined.

The spin resolved photoelectron spectra shown in this work were generated with UV laser light. The photon energy of 5.9 eV results in a very short inelastic scatter-

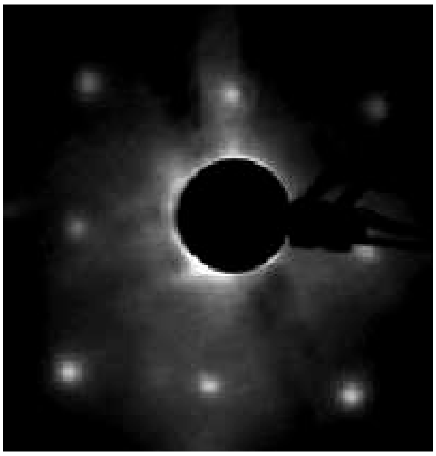

Figure 5.5: LEED pattern of a Co_2FeSi / MgO film after removal of the capping layer and subsequent annealing.

ing length. The resulting information depth is 1 – 2 nm [216, 217]. This allows a very surface sensitive analysis of the Heusler valence bands. On the other hand, it creates severe challenges with respect to sample preparation and handling. A small amount of adsorbents or surface oxidation will seriously degrade the photoelectron spectra.

The spin-resolved photoemission spectra of sputtered Co_2FeSi films presented here have been measured by the members of "AG Aeschlimann" at Kaiserslautern University. After *ex situ* transportation, the samples were transferred into a UHV system. Due to the extreme surface sensitivity, it was necessary to remove the Al protection layer prior to measurement. This was accomplished by Ar ion bombardment. The process was monitored by Auger electron spectroscopy. Subsequently, the samples were annealed at 300 °C in order to reconstruct the surface crystal structure.

LEED images taken after this preparation procedure show indeed an ordered fourfold surface for the films deposited on MgO. An example is presented in figure 5.5. The (110)-oriented Co_2FeSi / Al_2O_3 films do not show a crystalline surface. Spin-resolved spectra taken at room temperature are presented in figure 5.6. Over the accessible energy range, no structure is observed. For the majority states, this is to be expected from the band structure calculations. However, the clearly visible minority states contradict the theoretical predictions. In these measurements, the maximum spin polarization of Co_2FeSi / MgO is 12 %. This maximum is located 1.5 eV below the Fermi energy. At E_F, only 4 % spin polarization could be observed. For Co_2FeSi / Al_2O_3 no spin polarization could be detected at E_F.

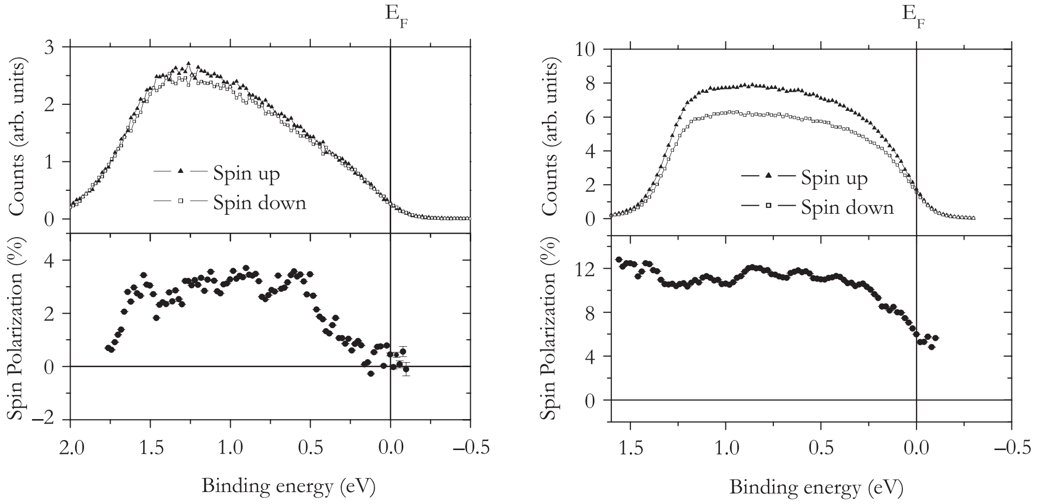

Figure 5.6: Left: Spin resolved photoemission spectra (top) and corresponding spin polarization (bottom) for a Co_2FeSi / Al_2O_3 film. Right: Analogous data for a Co_2FeSi / MgO film.

Most probably, these values are not intrinsic. Bulk magnetometry shows that these Heusler samples are clearly ferromagnetic. A reduction of surface magnetism can also be observed in XMCD spectra (see next section), but it is highly unlikely that the spin polarization drops to zero. These low values might rather be caused by the sputtering process. Different sputtering rates for the different elements in the film can induce additional surface degradation. From the LEED images, it is not possible to tell whether the surface consists of a Heusler layer or for example of fcc iron.

5.3 X-Ray Magnetic Circular Dichroism

X-ray magnetic circular dichroism (XMCD) spectroscopy is a rather new analytical technique [219]. Its main advantage is the possibility to perform element specific analysis of orbital and spin magnetic moments in a solid. Furthermore, it is possible in thin films and multilayers to assess bulk, surface, and interface magnetic properties [80, 220]. On a microscopic level, XMCD spectroscopy of transition metal atoms is realized by resonant X-ray absorption of highly localized, spin-orbit split *L* shell core electrons, as illustrated on the left hand side of figure 5.7 [221]. The experiments were performed in collaboration with the “AG Magnetismus” of the University of Mainz.

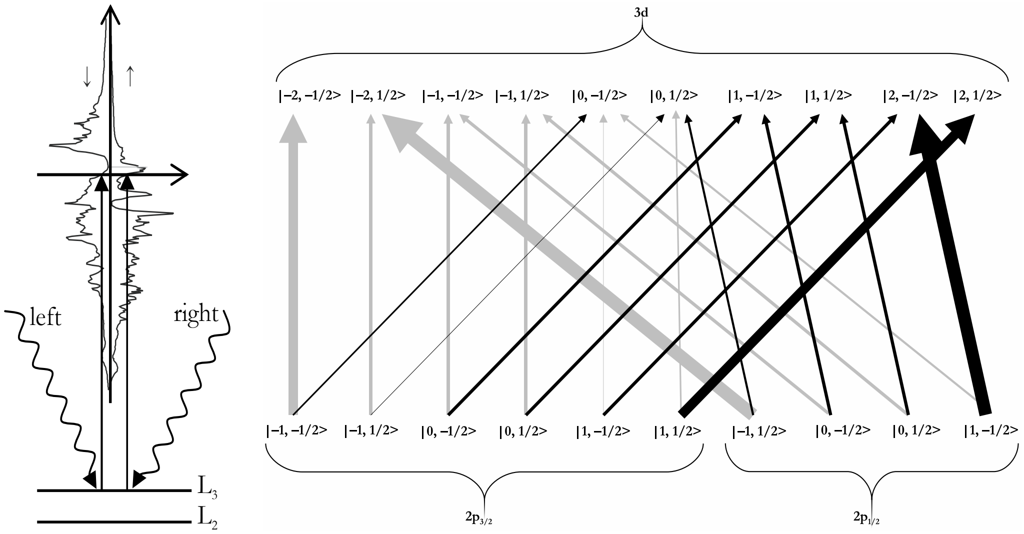

Figure 5.7: Left: Principle of an XMCD experiment: Circularly polarized photons excite the electrons of the spin-orbit split core shells into the exchange-split final states above the Fermi edge. Right: The spin polarization of the photoelectrons originates from the dipole transition rules [218]. The width of the arrows is proportional to the transition probability. Black (gray) arrows represent transitions for right (left) circular polarization. The spin-orbit splitting of the $3d$ states is small and has been neglected for better readability.

In a simple one-electron model of this process, the core level electrons are excited into empty states above the Fermi level. The channels $2p_{1/2} \rightarrow 4s_{1/2}$ and $2p_{3/2} \rightarrow 4s_{1/2}$ are strongly suppressed because of their small transition matrix elements. The remaining $2p \rightarrow 3d$ processes can be utilized to probe the exchange-split d bands at the Fermi surface. It can be seen from the transition probabilities depicted in figure 5.7 that the angular momentum of circularly polarized light is transferred to the photoelectrons [218]. Summing over the final states with different spin orientation, one finds that the excitation processes from the L_2 edge produces a net spin polarization of the photoelectrons for right circularly polarized light of +25 % and an orbital polarization of 75 %. For the opposite photon polarization one gets an electron spin polarization of −50 %, the orbital polarization again has a value of 75 %. The exchange split states at the Fermi energy then act as a spin detector for the excited electrons.

The resulting intensity difference for left and right circularly polarized radiation can then be used to determine spin and orbital contributions to the magnetic moment. A quantitative analysis can be performed with the following sum rules. For magnetic $3d$ elements the relations between absorption and magnetic moments are given by

$$m_{\mathrm{orb}} = -\frac{4\int_{L_3+L_2}(\mu_+ - \mu_-)\,dE}{3\int_{L_3+L_2}(\mu_+ + \mu_-)\,dE}(10 - n_{3d})$$

and

$$m_{\mathrm{spin}} = -\frac{6\int_{L_3}(\mu_+ - \mu_-)\,dE - 4\int_{L_2}(\mu_+ - \mu_-)\,dE}{3\int_{L_3+L_2}(\mu_+ + \mu_-)\,dE}(10 - n_{3d}),$$

with the absorption coefficients $\mu_\pm$ for left and right circularly polarized light, the photon energy E and the number of d electrons n_{3d}.

Two main problems complicate a quantitative sum rule analysis analysis: First, the sum rules depend on the number of d-electrons, which is in most cases—and especially for the Heusler alloys—only known theoretically. And second, it is often problematic to separate the signals from the L_2 and L_3 edges of light elements since spin-orbit splitting is small.

For a rigorous description the transition from a $2p^6 3d^M$ initial configuration into a $2p^5 3d^{M+1}$ final configuration has to be considered. This model takes correlation effects into account and reproduces the multiplet structures observed in XMCD spectra of oxides. However, for metallic 3d system the one electron model presented before is sufficient.

All X-ray absorption spectra presented here were taken at the UE56/1-SGM beamline of the BESSY II synchrotron light source. Instead of switching the polarization of the incident light, the magnetization was aligned parallel or antiparallel to the wave vector of the beam. For surface sensitive measurements the electric current created by Auger and secondary electron cascades was recorded (total electron yield, TEY). The escape depth of these electrons is in the order of a few nanometer. The transmitted (TM) intensity and therefore bulk properties could be analyzed because the X-ray light causes luminescence in the Al_2O_3 and MgO substrates. This light could be detected with a standard photodiode.

Figure 5.8 shows typical TEY and transmission spectra for a sputter deposited Co_2FeSi thin film. The two data sets for each orientation of the polarization were measured simultaneously. One can see a jump in intensity at the Co L_3 and L_2 energies. Additional peaks can be seen 4 eV above the maxima, the broadening above the L_2 edge is due to a shorter lifetime of the excited states. This feature is caused by a hybridization of Co d-band states with sp states from the main group element [55]. It can only be seen in $L2_1$ ordered thin films. In B2 ordered $Co_2Cr_{0.6}Fe_{0.4}Al$ films this additional feature is very weak [141], in oxidized bulk samples it vanishes completely [45]. Figure 5.9 shows the total X-ray absorption spectra for TM and

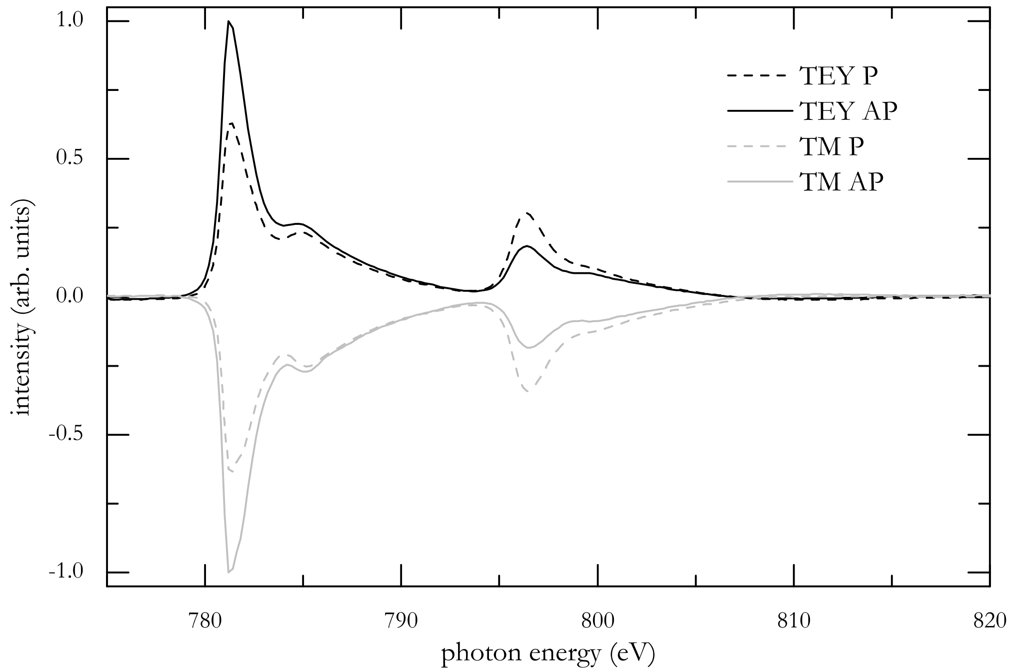

Figure 5.8: Total electron yield (TEY) and transmitted (TM) intensity for a sputtered Co_2FeSi film at the Co $L_{2,3}$ edges. Spectra for parallel and antiparallel alignment of magnetization and polarization vector are shown. A background caused by $2p \rightarrow 4s$ transitions and the reference luminescence of a naked substrate have been subtracted.

TEY modes. It can be seen here that this additional feature is more pronounced in the bulk, indicating a larger disorder at the surface.

This difference can also be observed in the XMCD spectra, as shown in figure 5.10. The bulk data has a greater asymmetry between the L_2 and L_3 transmission processes. From the sum rules follows that the spin magnetic moment at the surface is reduced by a factor of 1.1. Assuming an information depth of 30 Å for the TEY and that this reduction is due to magnetically dead layers, it is found that the topmost 1.5 Å of the film is nonmagnetic. A larger discrepancy and therefore a larger dead layer of 5.5 Å was found in $Co_2Cr_{0.6}Fe_{0.4}Al$ thin films [94]. This might explain the low spin polarization of junctions comprising of (110)-oriented $Co_2Cr_{0.6}Fe_{0.4}Al$ electrodes [149].

Furthermore, the transmission signals for Co_2FeSi films with varying thickness were investigated [80]. For a constant bulk magnetization, the product of magnetization and thickness should be linear in film thickness. This was confirmed experimentally. However, the linear fit does not intersect with the origin of the plot,

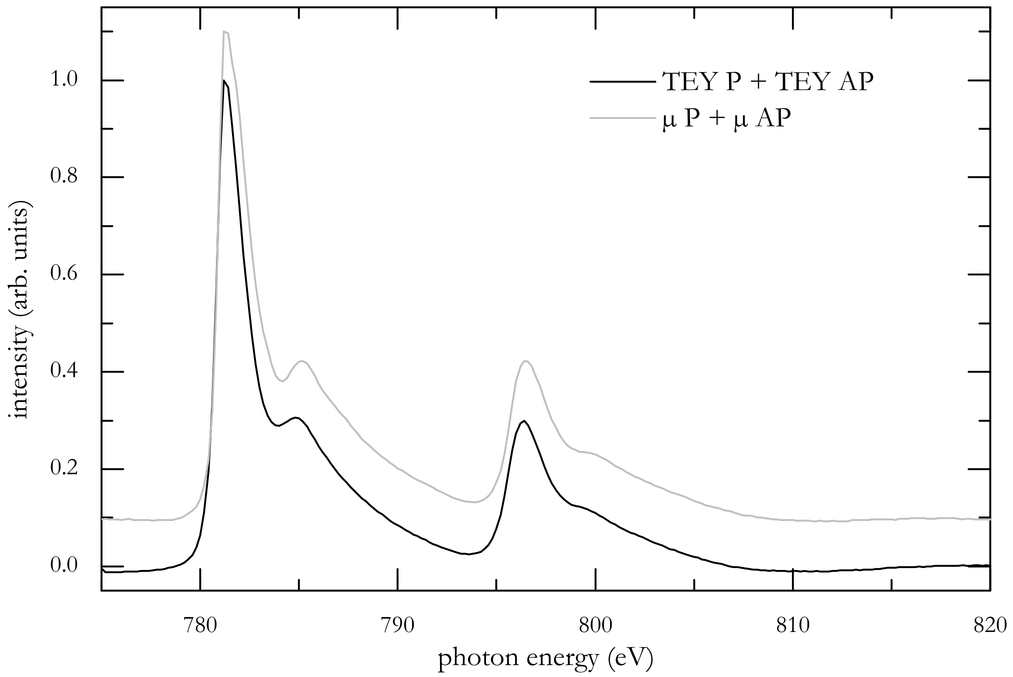

Figure 5.9: X-ray absorption spectra obtained by summing over the contributions shown in figure 5.8. μ denotes the absorption coefficient in transmission. Data were normalized to the absorption maxima at the L_3 edge and graphs were shifted vertically for better visibility.

which is due to magnetically dead portions. It was found that the dead layer has a thickness of 8 Å. From the discrepancy to the TEY result one can conclude, that the substrate-film interface is also magnetically degraded. Here the dead layer has a thickness of 6.5 Å.

Comparison of the magnetic properties of sputtered and laser ablated Co_2FeSi films could also be performed. Since XMCD is a surface averaging method, the covering of the film surface with melt droplets is a much smaller source of error than for bulk magnetometry. Comparison of the XMCD signal of two samples shows a much higher asymmetry for the laser ablated film. Employing the sum rules for the Co and Fe signals one finds that the total magnetization increases by 10 % [222], assuming the same stoichiometry and band structure for both sputtered and laser ablated films.

Finally, XMCD sprectroscopy allowed the mapping of the spin-polarized unoccupied densities of state of a $Co_2Mn_{1-x}Fe_xSi$ series [152]. On the assumption that the angular transition matrix elements can be averaged at every energy value it is

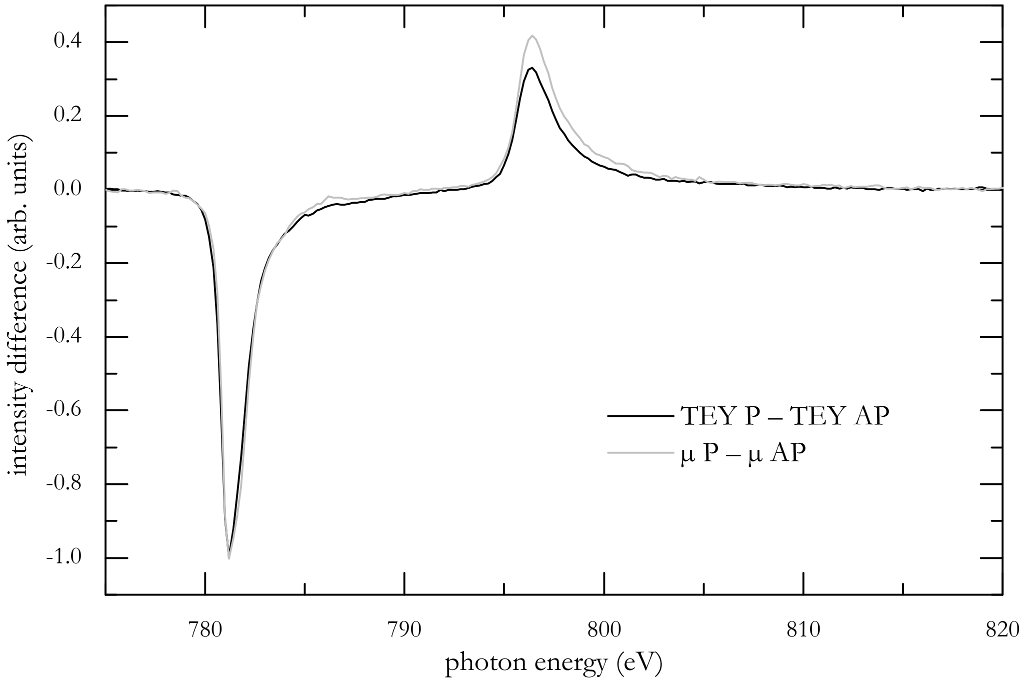

Figure 5.10: XMCD spectra for a Co_2FeSi sample. Spectra were obtained by subtracting the spin-resolved spectra in figure 5.8. Data were normalized to the L_3 minimum.

possible to invert the sum rules:

$$D^{\uparrow(\downarrow)}(1-f) \propto \frac{\mu^+ + \mu^-}{2} - s + (-)\frac{\mu^+ - \mu^-}{2P_j}, \tag{5.2}$$

where f denotes the Fermi distribution, s the step-like background function and P_j the spin polarization of the photoelectrons given on page 102.

The result of this inversion is shown in figure 5.11. For Co_2FeSi the minority states have a large maximum approximately 0.6 eV above the Fermi energy, at $E = 1$ eV a clear shoulder is observed. These features can be correlated to the theoretical band structure shown in figure 1.4 on page 12. Furthermore, the broad shoulder at 5 eV is caused by the hybridization of Co and Si also predicted from the theoretical model. For $Co_2Mn_{0.5}Fe_{0.5}Si$ and Co_2MnSi, the peak in the minority density of states shifts away from the Fermi energy as predicted in the same band structure calculations. However, the difference between Co_2FeSi and Co_2MnSi is only 0.4 eV, the predicted effect is larger by a factor of 4. In addition, despite a clear double-peak structure in the band structures, only weak modulations are present in

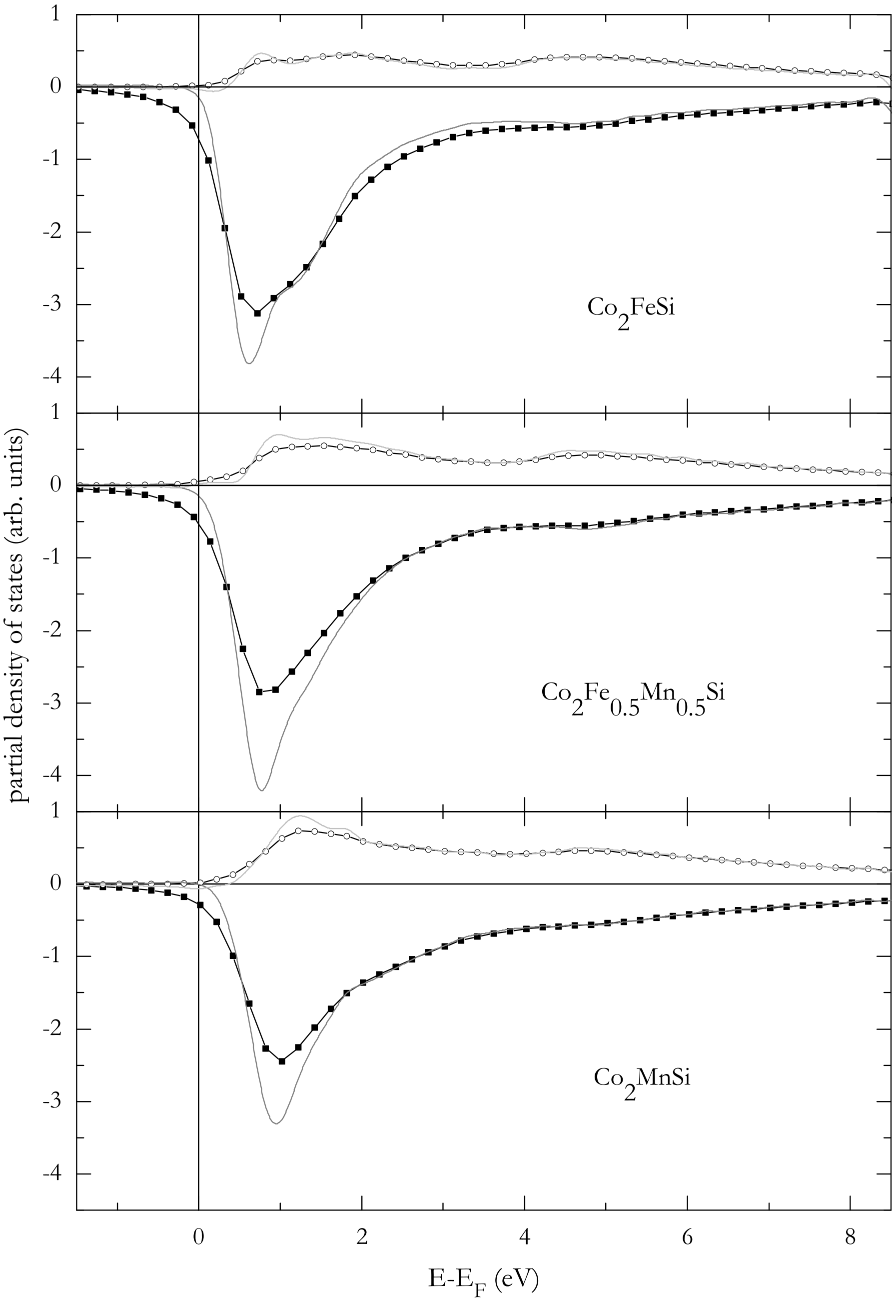

Figure 5.11: Reconstruction of the partial density of states of Co$_2$Mn$_{1-x}$Fe$_x$Si from Co XAS spectra. Majority states are shown on the positive scale. Symbols represent data reconstucted from measured data, according to equation (5.2). Full lines indicate deconvoluted data; an instrumental resolution of 0.4 eV was assumed.

the experimental data. If this is due to shortcomings of the calculations or surface degradation remains to be seen.

The question whether these materials are half-metals depends crucially on the position of the Fermi energy. Its value had to be obtained by comparison with theoretical data, and therefore an unambiguous answer is not possible. However, it could be shown that general features predicted by theory could be reproduced and the shift of the Fermi energy across a minimum in the minority density of states corroborates the findings from the Hall effect data.

The cooperation with external groups allowed the application of further experimental techniques. They allowed a more sophisticated view on the properties of $Co_2Mn_{1-x}Fe_xSi$. Due to the nature of the sample preparation prior to photoemission spectroscopy, it was not possible to obtain meaningful results. However, this highlights the delicate nature of the Heusler compounds with respect to contamination and disorder. In order to improve this situation, uncoated Heusler films were transferred to the photoemission setup in the portable vacuum chamber presented on page 26. Preliminary results show more structured spectra as well as clearly higher spin asymmetries at the Fermi edge.

MOKE magnetometry allowed a view into the magnetic properties of the Heusler films. A very large quadratic contribution was found in Co_2FeSi, much larger than in Co_2MnSi. The origin of this large effect is unknown at present. Equally unknown is the origin of the large difference to the Co_2MnSi samples. This situation opens plenty of opportunities to improve the understanding the nature of both the quadratic MOKE and the microscopic nature of the magnetism in Heusler compounds.

XMCD served at first as an independent source of magnetometry data. The results confirm the bulk properties obtained from vibrating sample or SQUID magnetometry. More important, it allowed investigating independently bulk and surface magnetism of the samples. Finally, an inversion procedure supports the calculated band structure and the results obtained from Hall experiments in this work: The Fermi energy of $Co_2Mn_{1-x}Fe_xSi$ moves closer to the minority conduction band if the Fe fraction is increased.

SUMMARY

During this work, thin films of Co-based Heusler compounds were deposited under optimized conditions, and their structural, magnetic, and transport properties were investigated. The growth of the thin film samples was accomplished by two different methods. At first $Co_2Cr_{0.6}Fe_{0.4}Al$ and Co_2FeSi were deposited by sputter deposition from stoichiometric targets. This is considered the standard technique for the preparation of thin Heusler films. Also for the compounds investigated here it resulted in samples with a high degree of $L2_1$ ordering. An excess of Fe atoms on Si sites was discovered by a detailed X-ray analysis in conjunction with NMR spectroscopy. The choice of different substrates allowed the adjustment of the growth direction. On the other hand, bulk magnetometry revealed that these sputter deposited films exhibit only a reduced magnetic moment, which is an indication of a reduced spin asymmetry at the Fermi level. One source of this problem seems to be a high residual gas pressure, which leads to an increased sample contamination.

To improve this situation, a pulsed laser deposition system was constructed and put into operation. The resulting film growth under ultra-high vacuum conditions led to a further improvement of the short-range crystallographic ordering and a clear enhancement of the magnetic properties. The additional use of a metallic buffer layer resulted in samples with a smooth surface. This opens the door for a number of further analytical experiments, such as tunneling spectroscopy or Brillouin light scattering. After this successful demonstration of this growth technique, an additional method for the flexible variation of the film stoichimetry was implemented. In this work, this method was successfully applied in the deposition of $Co_2Mn_{1-x}Fe_xSi$ films. All samples in this series show a high degree of atomic ordering. Their magnetization values are compatible with the Slater-Pauling rule for half-metallic Heusler compounds.

The availableness of these high quality quaternary alloy films allowed the systematic investigation of their electronic properties. Band structure calculations predict that the substitution of Mn by Fe leads to a shift of the Fermi energy over the minority energy gap, whereas the density of states remains nearly unchanged. The corresponding changes in the topology of the Fermi surface could be tested by electronic transport measurements. This is particularly obvious in the normal Hall effect. Here a transition from a hole-like charge transport in Co_2MnSi to an electron-like transport in Co_2FeSi could be demonstrated. This is in accordance with the corresponding band structure calculations. Additionally, with these samples comparative XMCD experiments were performed. The densities of states reconstructed from these spectra show the expected shift of the Fermi energy as well.

Furthermore, the behavior of the anomalous Hall effect was studied. Here it could be seen that the effect is influenced by two mechanisms: On the one hand an intrinsic contribution, caused by the topology of the Fermi surface and on the other hand by temperature dependent impurity scattering. These two effects have an opposing influence on the anomalous Hall effect. This can lead to an observable sign reversal of the anomalous contribution. This behavior has been predicted just recently and was in this work systematically investigated for the first time for Heusler compounds.

APPENDIX A

SAMPLE PATTERNING

The following list illustrates the film patterning process and serves as a protocol of the procedure.

0		**Untreated thin film.**
1		**Spin coating with positive photoresist and subsequent hardening.** Spin AZ 7812 photoresist at 4000 rpm for 30 s Bake for 2 minutes at 110 °C
2	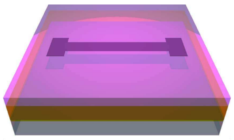	**Shadow mask is brought into contact with resist and illuminated with UV light.** 60 seconds exposure to Hg-vapor light.
3	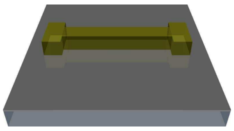	**Illuminated areas are removed with developer.** 30 s immersion in AZ MIF 300. Rinse with distilled water.
4		**Ion beam etching of the exposed film regions.** Optical control of film removal. (Typical exposure time: 10 min) **Remaining resist is dissolved in acetone.**

APPENDIX B

HALL RESISTIVITY AND HALL CONDUCTIVITY

Different formulations of the anomalous Hall effect describe either ρ_{xy} as a function of ρ_{xx} or σ_{xy} as a function of σ_{xx}. It is shown here how these two quantities are converted into each other. Especially, it is shown how the presence of a nonvanishing anomalous Hall resistivity affects the evolution of the transverse conductivity.

Experimentally, the electrical field produced by a given current is measured. For this reason, the resistivity tensor is chosen as a starting point:

$$(\rho_{ik}) = \begin{pmatrix} \rho_{xx,\perp}(\mathbf{B},\mathbf{M}) & -\rho_{xy}(\mathbf{B},\mathbf{M}) & 0 \\ \rho_{xy}(\mathbf{B},\mathbf{M}) & \rho_{xx,\perp}(\mathbf{B},\mathbf{M}) & 0 \\ 0 & 0 & \rho_{xx,\|}(\mathbf{B},\mathbf{M}) \end{pmatrix}. \qquad (4.1)$$

Inversion of ρ_{ik} results in the conductivity tensor

$$(\sigma_{ik}) = \frac{1}{\rho_{xx,\perp}^2 + \rho_{xy}^2} \begin{pmatrix} \rho_{xx,\perp} & \rho_{xy} & 0 \\ -\rho_{xy} & \rho_{xx,\perp} & 0 \\ 0 & 0 & \frac{\rho_{xx,\perp}^2 + \rho_{xy}^2}{\rho_{xx,\|}} \end{pmatrix}. \qquad (B.1)$$

Since the thin films investigated here as well as the samples reported in literature show that $\rho_{xx,\perp}^2 \approx \rho_{xx,\|}^2 \gg \rho_{xy}^2$, the relations between resistivity and conductivity can be simplified to

$$\sigma_{xx} = \frac{1}{\rho_{xx}} \text{ and } \sigma_{xy} = -\frac{\rho_{xy}}{\rho_{xx}^2}. \qquad (B.2)$$

Now a power law behavior between the anomalous Hall resistivity $\rho_{\mathrm{S}} \equiv \mu_0 R_{\mathrm{S}} M$ and the diagonal resistivity ρ_{xx} is assumed:

$$\rho_{\mathrm{S}} = \alpha \rho_{xx}^{\beta}. \tag{B.3}$$

The established theories predict $\beta = 1$ or $\beta = 2$, in which case the anomalous conductivity σ_{S} assumes

$$\sigma_{\mathrm{S}} = -\alpha \sigma_{xx} \text{ or } \sigma_{\mathrm{S}} = \text{const.}, \tag{B.4}$$

respectively. Linear fits of the experimental data in this works show a sizable anomalous contribution independent of ρ_{xx}. Equation (B.3) is therefore expanded to

$$\rho_{\mathrm{S}} = \alpha \rho_{xx}^{\beta} + \rho_{\mathrm{S},0} \tag{B.5}$$

This relation results in the following evolution of the anomalous Hall conductivity:

$$\sigma_{\mathrm{S}} = -\alpha \sigma_{xx}^{2-\beta} - \rho_{\mathrm{S},0} \sigma_{xx}^{2} \tag{B.6}$$

For the special cases $\beta = 1$ or 2, σ_{S} behaves as

$$\sigma_{\mathrm{S}} = -\alpha \sigma_{xx} - \rho_{\mathrm{S},0} \sigma_{xx}^{2} \text{ or} \tag{B.7}$$

$$\sigma_{\mathrm{S}} = -\alpha - \rho_{\mathrm{S},0} \sigma_{xx}^{2}, \tag{B.8}$$

respectively. For $\beta = 1$ an extremum is located at

$$\sigma_{xx} = -\frac{\alpha}{2\rho_{\mathrm{S},0}}. \tag{B.9}$$

BIBLIOGRAPHY

[1] M. N. Baibich, J. M. Broto, A. Fert, F. N. van Dau, F. Petroff, P. Etienne, G. Creuzet, A. Friederich, and J. Chazelas, *Physical Review Letters* **61**, 2472 (1988).
http://link.aps.org/doi/10.1103/PhysRevLett.61.2472, doi:10.1103/PhysRevLett.61.2472.

[2] G. Binasch, P. Grünberg, F. Saurenbach, and W. Zinn, *Physical Review B* **39**, 4828 (1989).
http://link.aps.org/doi/10.1103/PhysRevB.39.4828, doi:10.1103/PhysRevB.39.4828.

[3] G. A. Prinz, *Science* **282**, 1660 (1998).
http://www.sciencemag.org/cgi/doi/10.1126/science.282.5394.1660, doi:10.1126/science.282.5394.1660.

[4] S. A. Wolf, D. D. Awschalom, R. A. Buhrman, J. M. Daughton, S. von Molnár, M. L. Roukes, A. Y. Chtchelkanova, and D. M. Treger, *Science* **294**, 1488 (2001).
http://www.ncbi.nlm.nih.gov/pubmed/11711666, doi:10.1126/science.1065389.

[5] R. Richter, L. Bär, J. Wecker, and G. Reiss, *Journal of Applied Physics* **91**, 8402 (2002).
http://link.aip.org/link/JAPIAU/v91/i10/p8402/s1&Agg=doi, doi:10.1063/1.1447202.

[6] C. H. Smith and R. W. Schneider, in *Proceedings Sensors EXPO Boston*, 139 (1997).

[7] M. Julliere, *Physics Letters A* **54**, 225 (1975).
http://linkinghub.elsevier.com/retrieve/pii/0375960175901747, doi:10.1016/0375-9601(75)90174-7.

[8] R. A. de Groot, F. M. Mueller, P. G. van Engen, and K. H. J. Buschow, *Physical Review Letters* **50**, 2024 (1983).
http://link.aps.org/doi/10.1103/PhysRevLett.50.2024, doi:10.1103/PhysRevLett.50.2024.

[9] A. P. Ramirez, *Journal of Physics: Condensed Matter* **9**, 8171 (1997).
http://iopscience.iop.org/0953-8984/9/39/005, doi:10.1088/0953-8984/9/39/005.

[10] D. Serrate, J. M. de Teresa, and M. R. Ibarra, *Journal of Physics: Condensed Matter* **19**, 023201 (2007).
http://stacks.iop.org/0953-8984/19/i=2/a=023201?key=crossref.c682812d9d899d156577e366cddf1dbd, doi:10.1088/0953-8984/19/2/023201.

[11] M. Pénicaud, B. Siberchicot, C. B. Sommers, and J. Kübler, *Journal of Magnetism and Magnetic Materials* **103**, 212 (1992).
http://linkinghub.elsevier.com/retrieve/pii/030488539290255M, doi:10.1016/0304-8853(92)90255-M.

[12] K. Schwarz, *Journal of Physics F: Metal Physics* **16**, L211 (1986).
http://iopscience.iop.org/0305-4608/16/9/002, doi:10.1088/0305-4608/16/9/002.

[13] J.-H. Park, E. Vescovo, H.-J. Kim, C. Kwon, R. Ramesh, and T. Venkatesan, *Nature* **392**, 794 (1998). doi:10.1038/33883.

[14] M. Bowen, M. Bibes, A. Barthélémy, J.-P. Contour, A. Anane, Y. Lemaître, and A. Fert, *Applied Physics Letters* **82**, 233 (2003).
http://link.aip.org/link/APPLAB/v82/i2/p233/s1&Agg=doi, doi:10.1063/1.1534619.

[15] I. Galanakis and P. Mavropoulos, *Journal of Physics: Condensed Matter* **19**, 315213 (2007).

http://stacks.iop.org/0953-8984/19/i=31/a=315213?key=crossref.b7b9bad7b90e64cdf834a2e4833f6d94,
doi:10.1088/0953-8984/19/31/315213.

[16] F. Heusler, *Verhandlungen der Deutschen Physikalischen Gesellschaft* **5**, 219 (1903).

[17] F. Heusler, W. Starck, and E. Haupt, *Verhandlungen der Deutschen Physikalischen Gesellschaft* **5**, 220 (1903).

[18] P. J. Webster and K. R. A. Ziebeck, *Landolt-Börnstein New Series 1, Group III: Crystal and Solid State Physics, Volume 19: Magnetic Properties of Metals, Subvolume c: Alloys and Compounds of d-Elements with Main Group Elements, Part 2*, 75 (Springer) (1988).

[19] K. R. A. Ziebeck and K.-U. Neumann, *Landolt-Börnstein New Series 1, Group III: Condensed Matter, Volume 32: Magnetic Properties of Metals, Subvolume A: 3d, 4d and 5d Elements, Alloys and Compounds*, 64 (Springer) (2001).

[20] V. C. Rakhecha, R. Chakravarthy, and N. S. Satya Murthy, *Pramāna* **11**, 159 (1978).
http://www.ias.ac.in/j_archive/pramana/11/2/159-169/viewpage.html.

[21] K. R. A. Ziebeck and P. J. Webster, *Journal of Physics F: Metal Physics* **5**, 1756 (1975).
http://iopscience.iop.org/0305-4608/5/9/015,
doi:10.1088/0305-4608/5/9/015.

[22] P. J. Webster and K. R. A. Ziebeck, *Physics Letters A* **98**, 51 (1983).
http://linkinghub.elsevier.com/retrieve/pii/0375960183905431,
doi:10.1016/0375-9601(83)90543-1.

[23] S. Waki, Y. Yamaguchi, and K. Mitsugi, *Journal of the Physics Society Japan* **54**, 1673 (1985).
http://jpsj.ipap.jp/link?JPSJ/54/1673/,
doi:10.1143/JPSJ.54.1673.

[24] K. Ullakko, J. K. Huang, C. Kantner, R. C. O'Handley, and V. V. Kokorin, *Applied Physics Letters* **69**, 1966 (1996).

http://link.aip.org/link/APPLAB/v69/i13/p1966/s1&Agg=doi,
doi:10.1063/1.117637.

[25] I. Galanakis, P. H. Dederichs, and N. Papanikolaou, *Physical Review B* **66**, 174429 (2002).
http://link.aps.org/doi/10.1103/PhysRevB.66.174429,
doi:10.1103/PhysRevB.66.174429.

[26] G. H. Fecher, H. C. Kandpal, S. Wurmehl, J. Morais, H.-J. Lin, H.-J. Elmers, G. Schönhense, and C. Felser, *Journal of Physics: Condensed Matter* **17**, 7237 (2005).
http://stacks.iop.org/0953-8984/17/i=46/a=008?key=crossref.a816341695406eb8c42b102a66dc6941,
doi:10.1088/0953-8984/17/46/008.

[27] S. Wurmehl, G. H. Fecher, H. C. Kandpal, V. Ksenofontov, C. Felser, H.-J. Lin, and J. Morais, *Physical Review B* **72**, 184434 (2005).
http://link.aps.org/doi/10.1103/PhysRevB.72.184434,
doi:10.1103/PhysRevB.72.184434.

[28] S. Ishida, S. Fujii, S. Kashiwagi, and S. Asano, *Journal of the Physical Society of Japan* **64**, 2152 (1995).
http://jpsj.ipap.jp/link?JPSJ/64/2152/,
doi:10.1143/JPSJ.64.2152.

[29] K. Yakushiji, K. Saito, S. Mitani, K. Takanashi, Y. K. Takahashi, and K. Hono, *Applied Physics Letters* **88**, 222504 (2006).
http://link.aip.org/link/APPLAB/v88/i22/p222504/s1&Agg=doi,
doi:10.1063/1.2207987.

[30] C. Palmstrøm, *MRS Bull.* **28**, 725 (2003).
http://www.mrs.org/s_mrs/sec_subscribe.asp?CID=2987&DID=76961&action=detail.

[31] Y. Sakuraba, J. Nakata, M. Oogane, H. Kubota, Y. Ando, A. Sakuma, and T. Miyazaki, *Japanese Journal of Applied Physics* **44**, L1100 (2005).
http://jjap.ipap.jp/link?JJAP/44/L1100/,
doi:10.1143/JJAP.44.L1100.

[32] S. Kämmerer, A. Thomas, A. Hütten, and G. Reiss, *Applied Physics Letters* **85**, 79 (2004).

http://link.aip.org/link/APPLAB/v85/i1/p79/s1&Agg=doi, doi:10.1063/1.1769082.

[33] P. J. Webster, *Journal of Physics and Chemistry of Solids* **32**, 1221 (1971). http://linkinghub.elsevier.com/retrieve/pii/S0022369771801804, doi:10.1016/S0022-3697(71)80180-4.

[34] C. C. M. Campbell, *Journal of Physics F: Metal Physics* **5**, 1931 (1975). http://iopscience.iop.org/0305-4608/5/10/016, doi:10.1088/0305-4608/5/10/016.

[35] K. H. J. Buschow, P. G. van Engen, and R. Jongebreur, *Journal of Magnetism and Magnetic Materials* **38**, 1 (1983). http://linkinghub.elsevier.com/retrieve/pii/0304885383900975, doi:10.1016/0304-8853(83)90097-5.

[36] Y. Miura, M. Shirai, and K. Nagao, *Journal of Applied Physics* **99**, 08J112 (2006). http://link.aip.org/link/JAPIAU/v99/i8/p08J112/s1&Agg=doi, doi:10.1063/1.2176907.

[37] H. C. Kandpal, G. H. Fecher, and C. Felser, *Journal of Physics D: Applied Physics* **40**, 1507 (2007). http://stacks.iop.org/0022-3727/40/i=6/a=S01?key=crossref.8c36f4c05d83651dbdadb44cc018908c, doi:10.1088/0022-3727/40/6/S01.

[38] A. J. Bradley and J. W. Rodgers, *Proceedings of the Royal Society of London. Series A, Containing Papers of a Mathematical and Physical Character (1905-1934)* **144**, 340 (1934). http://rspa.royalsocietypublishing.org/cgi/doi/10.1098/rspa.1934.0053, doi:10.1098/rspa.1934.0053.

[39] P. J. Brown, K. U. Neumann, P. J. Webster, and K. R. A. Ziebeck, *Journal of Physics: Condensed Matter* **12**, 1827 (2000). http://iopscience.iop.org/0953-8984/12/8/325, doi:10.1088/0953-8984/12/8/325.

[40] P. J. Webster, *Contemporary Physics* **10**, 559 (1969). http://www.informaworld.com/openurl?genre=article&doi=10.1080/00107516908204800&

magic=crossref||D404A21C5BB053405B1A640AFFD44AE3, doi:10.1080/00107516908204800.

[41] J. C. Slater, *Physical Review* **49**, 931 (1936). http://link.aps.org/doi/10.1103/PhysRev.49.931, doi:10.1103/PhysRev.49.931.

[42] L. Pauling, *Physical Review* **54**, 899 (1938). http://link.aps.org/doi/10.1103/PhysRev.54.899, doi:10.1103/PhysRev.54.899.

[43] I. Galanakis, P. Mavropoulos, and P. H. Dederichs, *Journal of Physics D: Applied Physics* **39**, 765 (2006). http://stacks.iop.org/0022-3727/39/i=5/a=S01?key=crossref.1df9ab74ad7cc55a138f3a0a70618151, doi:10.1088/0022-3727/39/5/S01.

[44] G. H. Fecher, H. C. Kandpal, S. Wurmehl, C. Felser, and G. Schönhense, *Journal of Applied Physics* **99**, 08J106 (2006). http://link.aip.org/link/JAPIAU/v99/i8/p08J106/s1&Agg=doi, doi:10.1063/1.2167629.

[45] H. J. Elmers, S. Wurmehl, G. H. Fecher, G. Jakob, C. Felser, and G. Schönhense, *Journal of Magnetism and Magnetic Materials* **272–276**, 758 (2004). http://linkinghub.elsevier.com/retrieve/pii/S0304885303025666, doi:10.1016/j.jmmm.2003.12.1086.

[46] W. H. Wang, M. Przybylski, W. Kuch, L. I. Chelaru, J. Wang, Y. F. Lu, J. Barthel, H. L. Meyerheim, and J. Kirschner, *Physical Review B* **71**, 144416 (2005). http://link.aps.org/doi/10.1103/PhysRevB.71.144416, doi:10.1103/PhysRevB.71.144416.

[47] A. Yamasaki, S. Imada, R. Arai, H. Utsunomiya, S. Suga, T. Muro, Y. Saitoh, T. Kanomata, and S. Ishida, *Physical Review B* **65**, 104410 (2002). http://link.aps.org/doi/10.1103/PhysRevB.65.104410, doi:10.1103/PhysRevB.65.104410.

[48] I. Galanakis, *Physical Review B* **71**, 012413 (2005). http://link.aps.org/doi/10.1103/PhysRevB.71.012413, doi:10.1103/PhysRevB.71.012413.

[49] K. Inomata, S. Okamura, A. Miyazaki, M. Kikuchi, N. Tezuka, M. Wojcik, and E. Jedryka, *Journal of Physics D: Applied Physics* **39**, 816 (2006). `http://stacks.iop.org/0022-3727/39/i=5/a=S07?key=crossref.1852c23d1a946228e5c04e72f7062e99`, `doi:10.1088/0022-3727/39/5/S07`.

[50] Y. V. Kudryavtsev, V. A. Oksenenko, N. N. Lee, Y. P. Lee, J. Y. Rhee, and J. Dubowik, *Journal of Applied Physics* **97**, 113903 (2005). `http://link.aip.org/link/JAPIAU/v97/i11/p113903/s1&Agg=doi`, `doi:10.1063/1.1921327`.

[51] G. E. Bacon and J. S. Plant, *Journal of Physics F: Metal Physics* **1**, 524 (1971). `http://stacks.iop.org/0305-4608/1/i=4/a=325?key=crossref.579b052e6eec2021b1561729492a8cd7`, `doi:10.1088/0305-4608/1/4/325`.

[52] Y. Miura, K. Nagao, and M. Shirai, *Physical Review B* **69**, 144413 (2004). `http://link.aps.org/doi/10.1103/PhysRevB.69.144413`, `doi:10.1103/PhysRevB.69.144413`.

[53] S. Picozzi, A. Continenza, and A. J. Freeman, *Physical Review B* **69**, 094423 (2004). `http://link.aps.org/doi/10.1103/PhysRevB.69.094423`, `doi:10.1103/PhysRevB.69.094423`.

[54] I. Galanakis, K. Özdoğan, B. Aktaş, and E. Şaşıoğlu, *Applied Physics Letters* **89**, 042502 (2006). `http://link.aip.org/link/APPLAB/v89/i4/p042502/s1&Agg=doi`, `doi:10.1063/1.2235913`.

[55] S. Wurmehl, G. H. Fecher, K. Kroth, F. Kronast, H. A. Dürr, Y. Takeda, Y. Saitoh, K. Kobayashi, H.-J. Lin, G. Schönhense, and C. Felser, *Journal of Physics D: Applied Physics* **39**, 803 (2006). `http://stacks.iop.org/0022-3727/39/i=5/a=S06?key=crossref.94556badf0db94b5fb7e14de91682829`, `doi:10.1088/0022-3727/39/5/S06`.

[56] B. Balke, G. H. Fecher, and C. Felser, *Applied Physics Letters* **90**, 242503 (2007). `http://link.aip.org/link/APPLAB/v90/i24/p242503/s1&Agg=doi`, `doi:10.1063/1.2748341`.

[57] K. Inomata, M. Wojcik, E. Jedryka, N. Ikeda, and N. Tezuka, *Physical Review B* **77**, 214425 (2008).
`http://link.aps.org/doi/10.1103/PhysRevB.77.214425`,
`doi:10.1103/PhysRevB.77.214425`.

[58] S. Wurmehl, J. T. Kohlhepp, H. J. M. Swagten, B. Koopmans, C. G. F. Blum, V. Ksenofontov, H. Schneider, G. Jakob, D. Ebke, and G. Reiss, *Journal of Physics D: Applied Physics* **42**, 084017 (2009).
`http://stacks.iop.org/0022-3727/42/i=8/a=084017?key=crossref.21abf492592d7effcaec26704e630e37`,
`doi:10.1088/0022-3727/42/8/084017`.

[59] T. Block, C. Felser, G. Jakob, J. Ensling, B. Mühling, P. Gütlich, and R. J. Cava, *Journal of Solid State Chemistry* **176**, 646 (2003).
`http://linkinghub.elsevier.com/retrieve/pii/S0022459603004225`,
`doi:10.1016/j.jssc.2003.07.002`.

[60] M. Zhang, Z. Liu, H. Hu, G. Liu, Y. Cui, J. Chen, G. Wu, X. Zhang, and G. Xiao, *Journal of Magnetism and Magnetic Materials* **277**, 130 (2004).
`http://linkinghub.elsevier.com/retrieve/pii/S0304885303008898`,
`doi:10.1016/j.jmmm.2003.10.017`.

[61] C. Felser, B. Heitkamp, F. Kronast, D. Schmitz, S. Cramm, H. A. Dürr, H.-J. Elmers, G. H. Fecher, S. Wurmehl, T. Block, D. Valdaitsev, S. A. Nepijko, A. Gloskovskii, G. Jakob, G. Schönhense, and W. Eberhardt, *Journal of Physics: Condensed Matter* **15**, 7019 (2003).
`http://stacks.iop.org/0953-8984/15/i=41/a=010?key=crossref.8bad13ddf8c75e9b421c6a2420195017`,
`doi:10.1088/0953-8984/15/41/010`.

[62] K. H. J. Buschow and P. G. van Engen, *Journal of Magnetism and Magnetic Materials* **25**, 90 (1981).
`http://linkinghub.elsevier.com/retrieve/pii/0304885381901517`,
`doi:10.1016/0304-8853(81)90151-7`.

[63] G. H. Fecher, private communication (2009).

[64] K. Inomata, N. Tezuka, S. Okamura, H. Kurebayashi, and A. Hirohata, *Journal of Applied Physics* **95**, 7234 (2004).
`http://link.aip.org/link/?JAP/95/7234/1&Agg=doi`,
`doi:10.1063/1.1651813`.

[65] G. Jakob, F. Casper, V. Beaumont, S. Falk, N. Auth, H.-J. Elmers, C. Felser, and H. Adrian, *Journal of Magnetism and Magnetic Materials* **290–291**, 1104 (2005).
http://linkinghub.elsevier.com/retrieve/pii/S0304885304017329,
doi:10.1016/j.jmmm.2004.11.466.

[66] T. Marukame, T. Kasahara, K.-i. Matsuda, T. Uemura, and M. Yamamoto, *Japanese Journal of Applied Physics* **44**, L521 (2005).
http://jjap.ipap.jp/link?JJAP/44/L521/,
doi:10.1143/JJAP.44.L521.

[67] A. Conca, M. Jourdan, and H. Adrian, *Journal of Physics D: Applied Physics* **40**, 1534 (2007).
http://stacks.iop.org/0022-3727/40/i=6/a=S03?key=crossref.0b65e48e16785c2c8b3f0ae6f7818576,
doi:10.1088/0022-3727/40/6/S03.

[68] C. Herbort, E. Arbelo Jorge, and M. Jourdan, *Applied Physics Letters* **94**, 142504 (2009).
http://link.aip.org/link/APPLAB/v94/i14/p142504/s1&Agg=doi,
doi:10.1063/1.3114425.

[69] A. Hirohata, H. Kurebayashi, S. Okamura, M. Kikuchi, T. Masaki, T. Nozaki, N. Tezuka, and K. Inomata, *Journal of Applied Physics* **97**, 103714 (2005).
http://link.aip.org/link/JAPIAU/v97/i10/p103714/s1&Agg=doi,
doi:10.1063/1.1888050.

[70] T. Marukame, T. Ishikawa, K.-I. Matsuda, T. Uemura, and M. Yamamoto, *Applied Physics Letters* **88**, 262503 (2006).
http://link.aip.org/link/APPLAB/v88/i26/p262503/s1&Agg=doi,
doi:10.1063/1.2217166.

[71] W. H. Butler, X.-G. Zhang, T. C. Schulthess, and J. M. MacLaren, *Physical Review B* **63**, 054416 (2001).
http://link.aps.org/doi/10.1103/PhysRevB.63.054416,
doi:10.1103/PhysRevB.63.054416.

[72] S. Picozzi, A. Continenza, and A. J. Freeman, *Physical Review B* **66**, 094421 (2002).
http://link.aps.org/doi/10.1103/PhysRevB.66.094421,
doi:10.1103/PhysRevB.66.094421.

[73] B. Balke, G. H. Fecher, H. C. Kandpal, C. Felser, K. Kobayashi, E. Ikenaga, J.-J. Kim, and S. Ueda, *Physical Review B* **74**, 104405 (2006).
`http://link.aps.org/doi/10.1103/PhysRevB.74.104405`,
`doi:10.1103/PhysRevB.74.104405`.

[74] M. P. Raphael, B. Ravel, M. A. Willard, S. F. Cheng, B. N. Das, R. M. Stroud, K. M. Bussmann, J. H. Claassen, and V. G. Harris, *Applied Physics Letters* **79**, 4396 (2001).
`http://link.aip.org/link/APPLAB/v79/i26/p4396/s1&Agg=doi`,
`doi:10.1063/1.1428625`.

[75] B. Ravel, M. P. Raphael, V. G. Harris, and Q. Huang, *Physical Review B* **65**, 184431 (2002).
`http://link.aps.org/doi/10.1103/PhysRevB.65.184431`,
`doi:10.1103/PhysRevB.65.184431`.

[76] Y. Sakuraba, M. Hattori, M. Oogane, H. Kubota, Y. Ando, A. Sakuma, and T. Miyazaki, *Journal of Physics D: Applied Physics* **40**, 1221 (2007).
`http://stacks.iop.org/0022-3727/40/i=5/a=S02?key=crossref.eff7a63c5303d40ea52e1fa0f049c497`,
`doi:10.1088/0022-3727/40/5/S02`.

[77] D. Wang, C. Nordman, J. M. Daughton, Z. Qian, and J. Fink, *IEEE Transactions on Magnetics* **40**, 2269 (2004).
`http://ieeexplore.ieee.org/lpdocs/epic03/wrapper.htm?arnumber=1325474`, `doi:10.1109/TMAG.2004.830219`.

[78] J. S. Moodera and G. Mathon, *Journal of Magnetism and Magnetic Materials* **200**, 248 (1999).
`http://linkinghub.elsevier.com/retrieve/pii/S0304885399005156`,
`doi:10.1016/S0304-8853(99)00515-6`.

[79] F. Bloch, *Zeitschrift für Physik* **61**, 206 (1930).
`http://www.springerlink.com/index/10.1007/BF01339661`,
`doi:10.1007/BF01339661`.

[80] M. Kallmayer, H. Schneider, G. Jakob, H. J. Elmers, B. Balke, and S. Cramm, *Journal of Physics D: Applied Physics* **40**, 1552 (2007).
`http://stacks.iop.org/0022-3727/40/i=6/a=S07?key=crossref.080736123b4c05b3c12c5d689684154a`,
`doi:10.1088/0022-3727/40/6/S07`.

[81] N. D. Telling, P. S. Keatley, L. R. Shelford, E. Arenholz, G. van der Laan, R. J. Hicken, Y. Sakuraba, S. Tsunegi, M. Oogane, Y. Ando, K. Takanashi, and T. Miyazaki, *Applied Physics Letters* **92**, 192503 (2008).
`http://link.aip.org/link/APPLAB/v92/i19/p192503/s1&Agg=doi`,
`doi:10.1063/1.2927482`.

[82] Y. Sakuraba, M. Hattori, M. Oogane, Y. Ando, H. Kato, A. Sakuma, T. Miyazaki, and H. Kubota, *Applied Physics Letters* **88**, 192508 (2006).
`http://link.aip.org/link/APPLAB/v88/i19/p192508/s1&Agg=doi`,
`doi:10.1063/1.2202724`.

[83] J. J. Attema, G. A. de Wijs, and R. A. de Groot, *Journal of Physics: Condensed Matter* **19**, 315212 (2007).
`http://stacks.iop.org/0953-8984/19/i=31/a=315212?key=crossref.883b464b5386cd7e7beee08d1eb70c5f`,
`doi:10.1088/0953-8984/19/31/315212`.

[84] L. Chioncel, Y. Sakuraba, E. Arrigoni, M. I. Katsnelson, M. Oogane, Y. Ando, T. Miyazaki, E. Burzo, and A. I. Lichtenstein, *Physical Review Letters* **100**, 086402 (2008).
`http://link.aps.org/doi/10.1103/PhysRevLett.100.086402`,
`doi:10.1103/PhysRevLett.100.086402`.

[85] J. A. Hertz and D. M. Edwards, *Journal of Physics F: Metal Physics* **3**, 2174 (1973).
`http://iopscience.iop.org/0305-4608/3/12/018`,
`doi:10.1088/0305-4608/3/12/018`.

[86] C. Lü, M. W. Wu, and X. F. Han, *Physics Letters A* **319**, 205 (2003).
`http://linkinghub.elsevier.com/retrieve/pii/S037596010301538X`,
`doi:10.1016/j.physleta.2003.10.010`.

[87] V. Drewello, J. Schmalhorst, A. Thomas, and G. Reiss, *Physical Review B* **77**, 014440 (2008).
`http://link.aps.org/doi/10.1103/PhysRevB.77.014440`,
`doi:10.1103/PhysRevB.77.014440`.

[88] S. Chadov, G. H. Fecher, C. Felser, J. Minár, J. Braun, and H. Ebert, *Journal of Physics D: Applied Physics* **42**, 084002 (2009).
`http://stacks.iop.org/0022-3727/42/i=8/a=084002?key=crossref.bac78927a6bdccb3c572159c9d867a0c`,
`doi:10.1088/0022-3727/42/8/084002`.

[89] V. Niculescu, T. J. Burch, K. Raj, and J. I. Budnick, *Journal of Magnetism and Magnetic Materials* **5**, 60 (1977).
`http://linkinghub.elsevier.com/retrieve/pii/0304885377901974`,
`doi:10.1016/0304-8853(77)90197-4`.

[90] R. M. Martin, *Electronic Structure* (Cambridge University Press) (2004).

[91] J. Kübler, A. R. William, and C. B. Sommers, *Physical Review B* **28**, 1745 (1983).
`http://link.aps.org/doi/10.1103/PhysRevB.28.1745`,
`doi:10.1103/PhysRevB.28.1745`.

[92] H. C. Kandpal, G. H. Fecher, C. Felser, and G. Schönhense, *Physical Review B* **73**, 094422 (2006).
`http://link.aps.org/doi/10.1103/PhysRevB.73.094422`,
`doi:10.1103/PhysRevB.73.094422`.

[93] G. H. Fecher, B. Balke, S. Ouardi, C. Felser, G. Schönhense, E. Ikenaga, J.-J. Kim, S. Ueda, and K. Kobayashi, *Journal of Physics D: Applied Physics* **40**, 1576 (2007).
`http://stacks.iop.org/0022-3727/40/i=6/a=S11?key=crossref.4677ae9c18aab0a75a77be2a8b1fad6d`,
`doi:10.1088/0022-3727/40/6/S11`.

[94] M. Kallmayer, H. J. Elmers, B. Balke, S. Wurmehl, F. Emmerling, G. H. Fecher, and C. Felser, *Journal of Physics D: Applied Physics* **39**, 786 (2006).
`http://stacks.iop.org/0022-3727/39/i=5/a=S03?key=crossref.a7cb6a5838ceafce1e2ed6301c832b5c`,
`doi:10.1088/0022-3727/39/5/S03`.

[95] S. Wurmehl, J. T. Kohlhepp, H. J. M. Swagten, B. Koopmans, M. Wójcik, B. Balke, C. G. F. Blum, V. Ksenofontov, G. H. Fecher, and C. Felser, *Applied Physics Letters* **91**, 052506 (2007).
`http://link.aip.org/link/APPLAB/v91/i5/p052506/s1&Agg=doi`,
`doi:10.1063/1.2760158`.

[96] D. Ebke, J. Schmalhorst, A. Hütten, G. Reiss, B. Balke, and C. Felser, *Verhandlungen der Deutschen Physikalischen Gesellschaft VI* **4/2007**, 448 (2007).

[97] A. Hütten, private communication (2007).

[98] G. Kotliar, S. Y. Savrasov, K. Haule, V. S. Oudovenko, O. Parcollet, and C. A. Marianetti, *Reviews of Modern Physics* **78**, 865 (2006).
http://link.aps.org/doi/10.1103/RevModPhys.78.865,
doi:10.1103/RevModPhys.78.865.

[99] S. Chadov, private communication (2009).

[100] U. Geiersbach, A. Bergmann, and K. Westerholt, *Journal of Magnetism and Magnetic Materials* **240**, 546 (2002).
http://linkinghub.elsevier.com/retrieve/pii/S0304885301008666,
doi:10.1016/S0304-8853(01)00866-6.

[101] N. D. Telling, P. S. Keatley, G. van der Laan, R. J. Hicken, E. Arenholz, Y. Sakuraba, M. Oogane, Y. Ando, and T. Miyazaki, *Physical Review B* **74**, 224439 (2006).
http://link.aps.org/doi/10.1103/PhysRevB.74.224439,
doi:10.1103/PhysRevB.74.224439.

[102] P. Villars and L. D. Calvert, *Pearson's Handbook of Crystallographic Data for Intermetallic Phases* (ASM International) (1996).

[103] D. L. Smith, *Thin-film deposition: principles and practice* (McGraw-Hill) (1995).

[104] A. Goswami, *Thin Film Fundamentals* (New Age International) (1996).

[105] R. Kelekar and B. M. Clemens, *Journal of Applied Physics* **96**, 540 (2004).
http://link.aip.org/link/JAPIAU/v96/i1/p540/s1&Agg=doi,
doi:10.1063/1.1759399.

[106] D. K. Aswal, K. P. Muthe, S. Tawde, S. Chodhury, N. Bagkar, A. Singh, S. K. Gupta, and J. V. Yakhimi, *Journal of Crystal Growth* **236**, 661 (2002).
http://linkinghub.elsevier.com/retrieve/pii/S0022024802008527,
doi:10.1016/S0022-0248(02)00852-7.

[107] W. Braun, *Applied RHEED* (Springer) (1999).

[108] M. Oogane, Y. Sakuraba, J. Nakata, H. Kubota, Y. Ando, A. Sakuma, and T. Miyazaki, *Journal of Physics D: Applied Physics* **39**, 834 (2006).
http://stacks.iop.org/0022-3727/39/i=5/a=S09?key=crossref.58411bf15ef99a6b843edd5cd8d76ec1,
doi:10.1088/0022-3727/39/5/S09.

[109] M. Murugesan, H. Obara, Y. Nakagawa, S. Kosaka, and H. Yamasaki, *Superconductor Science and Technology* **17**, 113 (2004). `http://stacks.iop.org/0953-2048/17/i=1/a=019?key=crossref.e4fceb284883bbb72b088e365d4ef436`, `doi:10.1088/0953-2048/17/1/019`.

[110] A. Conca, *Development and demonstration of a new deposition chamber for TMR elements*, Diploma thesis, Johannes Gutenberg-Universität Mainz (2003).

[111] H. J. Elmers, private communication (2006).

[112] J. Hamrle, private communication (2008).

[113] S. Rossnagel, *Handbook of Thin-Film Deposition Processes and Techniques*, 319 (Noyes Publications) (2002).

[114] M. Yamamoto, T. Marukame, T. Ishikawa, K. Matsuda, T. Uemura, and M. Arita, *Journal of Physics D: Applied Physics* **39**, 824 (2006). `http://stacks.iop.org/0022-3727/39/i=5/a=S08?key=crossref.d4e36a2229b43d9f5bf10d09ac2a9ac4`, `doi:10.1088/0022-3727/39/5/S08`.

[115] S. M. Green, A. Piqué, K. S. Harshavardhan, and J. S. Bernstein, *Pulsed Laser Deposition of Thin Films*, 23 (John Wiley & Sons, Inc.) (1994).

[116] R. Kelly and A. Miotello, *Pulsed Laser Deposition of Thin Films*, 55 (John Wiley & Sons, Inc.) (1994).

[117] D. B. Geohegan, *Pulsed Laser Deposition of Thin Films*, 115 (John Wiley & Sons, Inc.) (1994).

[118] J. Schou, *Applied Surface Science* **255**, 5191 (2009). `http://linkinghub.elsevier.com/retrieve/pii/S0169433208022617`, `doi:10.1016/j.apsusc.2008.10.101`.

[119] L.-C. Chen, *Pulsed Laser Deposition of Thin Films*, 167 (John Wiley & Sons, Inc.) (1994).

[120] R. E. Muenchausen and X. D. Wu, *Pulsed Laser Deposition of Thin Films*, 357 (John Wiley & Sons, Inc.) (1994).

[121] J. C. S. Kools, *Pulsed Laser Deposition of Thin Films*, 455 (John Wiley & Sons, Inc.) (1994).

[122] J. Giapintzakis, C. Grigorescu, A. Klini, A. Manousaki, V. Zorba, J. Androulakis, Z. Viskadourakis, and C. Fotakis, *Applied Physics Letters* **80**, 2716 (2002). http://link.aip.org/link/APPLAB/v80/i15/p2716/s1&Agg=doi, doi:10.1063/1.1469211.

[123] J. H. Clark and R. G. Weston, *Measurement Science and Technology* **7**, 823 (1996). http://iopscience.iop.org/0957-0233/7/5/014/, doi:10.1088/0957-0233/7/5/014.

[124] N. W. Ashcroft and N. D. Mermin, *Solid State Physics* (Harcourt Brace & Company), 1st edition (1976).

[125] C. T. Chantler, K. Olsen, R. A. Dragoset, J. Chang, A. R. Kishore, S. A. Kotochigova, and D. S. Zucker, *X-Ray Form Factor, Attenuation and Scattering Tables*. http://physics.nist.gov/PhysRefData/FFast/Text/cover.html.

[126] W. Kraus and G. Nolze, *Journal of Applied Crystallography* **29**, 301 (1996). http://scripts.iucr.org/cgi-bin/paper?S0021889895014920, doi:10.1107/S0021889895014920.

[127] Bundesanstalt für Materialforschung und -prüfung, *PowderCell*. http://www.bam.de/de/service/publikationen/powder_cell.htm.

[128] H. Kiessig, *Annalen der Physik* **402**, 769 (1931). http://doi.wiley.com/10.1002/andp.19314020702, doi:10.1002/andp.19314020702.

[129] L. G. Parratt, *Physical Review* **95**, 359 (1954). http://link.aps.org/doi/10.1103/PhysRev.95.359, doi:10.1103/PhysRev.95.359.

[130] C. Braun, Hahn-Meitner-Institut Berlin GmbH, Parratt32 (1997 – 2002).

[131] E. Bauer, *Journal of Vacuum Science and Technology* **7**, 3 (1970). doi:10.1116/1.1315823.

[132] P. J. Estrup and E. G. McRae, *Surface Science* **25**, 1 (1971).
http://linkinghub.elsevier.com/retrieve/pii/0039602871902093,
doi:10.1016/0039-6028(71)90209-3.

[133] S. Foner, *Review of Scientific Instruments* **30**, 548 (1959).
http://link.aip.org/link/RSINAK/v30/i7/p548/s1&Agg=doi,
doi:10.1063/1.1716679.

[134] A. H. Silver and J. E. Zimmerman, *Physical Review* **157**, 317 (1967).
http://link.aps.org/doi/10.1103/PhysRev.157.317,
doi:10.1103/PhysRev.157.317.

[135] V. D. Kuznetsov, *Soviet Physics Journal* **27**, 118 (1984).
http://www.springerlink.com/index/10.1007/BF00900130,
doi:10.1007/BF00900130.

[136] B. D. Josephson, *Physics Letters* **1**, 251 (1962).
http://linkinghub.elsevier.com/retrieve/pii/0031916362913690,
doi:10.1016/0031-9163(62)91369-0.

[137] P. Stamenov and J. M. D. Coey, *Review of Scientific Instruments* **77**, 015106 (2006).
http://link.aip.org/link/RSINAK/v77/i1/p015106/s1&Agg=doi,
doi:10.1063/1.2149190.

[138] D. B. Williams and C. B. Carter, *Transmission Electron Microscopy* (Plenum Press) (1996).

[139] M. E. Smith and J. H. Strange, *Measurement Science and Technology* **7**, 449 (1996).
http://iopscience.iop.org/0957-0233/7/4/002,
doi:10.1088/0957-0233/7/4/002.

[140] S. Wurmehl and J. T. Kohlhepp, *Journal of Physics D: Applied Physics* **41**, 173002 (2008).
http://stacks.iop.org/0022-3727/41/i=17/a=173002?key=crossref.8f164c33eca5d20ff8334af8a1a18bd1,
doi:10.1088/0022-3727/41/17/173002.

[141] M. Kallmayer, H. Schneider, G. Jakob, H. J. Elmers, K. Kroth, H. C. Kandpal, U. Stumm, and S. Cramm, *Applied Physics Letters* **88**, 072506 (2006).

http://link.aip.org/link/APPLAB/v88/i7/p072506/s1&Agg=doi, doi:10.1063/1.2175486.

[142] A. Conca, *Magnetic Tunneling Junctions with the Heusler compound* $Co_2Cr_{0.6}Fe_{0.4}Al$, Ph.D. thesis, Johannes Gutenberg-Universität Mainz (2007).

[143] M. Kallmayer, K. Hild, T. Eichhorn, H. Schneider, G. Jakob, A. Conca, M. Jourdan, H. J. Elmers, A. Gloskovskii, S. Schuppler, and P. Nagel, *Applied Physics Letters* **91**, 192501 (2007). http://link.aip.org/link/APPLAB/v91/i19/p192501/s1&Agg=doi, doi:10.1063/1.2805812.

[144] E. W. Otten, *Repetitorium Experimentalphysik* (Springer) (1998).

[145] H. Bach, K. Westerholt, and U. Geiersbach, *Journal of Crystal Growth* **237–239**, 2046 (2002). http://linkinghub.elsevier.com/retrieve/pii/S0022024801023089, doi:10.1016/S0022-0248(01)02308-9.

[146] C. C. Murdock, *Physical Review* **35**, 8 (1930). http://link.aps.org/doi/10.1103/PhysRev.35.8, doi:10.1103/PhysRev.35.8.

[147] P. Scherrer, *Nachrichten von der Gesellschaft der Wissenschaften zu Göttingen, Mathematisch-Physikalische Klasse* **1918**, 98 (1918).

[148] U. Köbler, *Journal of Physics: Condensed Matter* **14**, 8861 (2002). http://stacks.iop.org/0953-8984/14/i=38/a=310?key=crossref.3b5a7b12e29ae378f82de32da2316e68, doi:10.1088/0953-8984/14/38/310.

[149] A. Conca, S. Falk, G. Jakob, M. Jourdan, and H. Adrian, *Journal of Magnetism and Magnetic Materials* **290–291**, 1127 (2005). http://linkinghub.elsevier.com/retrieve/pii/S030488530401738X, doi:10.1016/j.jmmm.2004.11.473.

[150] J. T. Cheung, *Pulsed Laser Deposition of Thin Films*, 1 (John Wiley & Sons, Inc.) (1994).

[151] M. Jourdan, private communication (2010).

[152] M. Kallmayer, P. Klaer, H. Schneider, E. Arbelo Jorge, C. Herbort, G. Jakob, M. Jourdan, and H. J. Elmers, *Physical Review B* **80**, 020406 (2009). http://link.aps.org/doi/10.1103/PhysRevB.80.020406, doi:10.1103/PhysRevB.80.020406.

[153] J. M. Ziman, *Electrons and Phonons* (Oxford) (2001).

[154] C. M. Hurd, *Advances in Physics* **23**, 315 (1974). http://www.informaworld.com/openurl?genre=article&doi=10.1080/00018737400101361&magic=crossref||D404A21C5BB053405B1A640AFFD44AE3, doi:10.1080/00018737400101361.

[155] J. F. Nye, *Physical Properties of Crystals* (Oxford) (1985).

[156] R. Spal, *Journal of Applied Physics* **51**, 4221 (1980). http://link.aip.org/link/JAPIAU/v51/i8/p4221/s1&Agg=doi, doi:10.1063/1.328281.

[157] L. J. van der Pauw, *Philips Research Reports* **13**, 1 (1958).

[158] I. Isenberg, B. R. Russell, and R. F. Greene, *Review of Scientific Instruments* **19**, 685 (1948). http://link.aip.org/link/RSINAK/v19/i10/p685/s1&Agg=doi, doi:10.1063/1.1741078.

[159] I. Mannari, *Progress of Theoretical Physics* **22**, 335 (1959). http://ptp.ipap.jp/link?PTP/22/335/, doi:10.1143/PTP.22.335.

[160] D. L. Mills, A. Fert, and I. A. Campbell, *Physical Review B* **4**, 196 (1971). http://link.aps.org/doi/10.1103/PhysRevB.4.196, doi:10.1103/PhysRevB.4.196.

[161] R. Richter, M. Wolf, and F. Goedsche, *Physica Status Solidi (b)* **95**, 473 (1979). http://doi.wiley.com/10.1002/pssb.2220950217, doi:10.1002/pssb.2220950217.

[162] K. Kubo and N. Ohata, *Journal of the Physical Society of Japan* **33**, 21 (1972). http://jpsj.ipap.jp/link?JPSJ/33/21/, doi:10.1143/JPSJ.33.21.

[163] N. Furukawa, *Journal of the Physics Society Japan* **69**, 1954 (2000). http://jpsj.ipap.jp/link?JPSJ/69/1954/, doi:10.1143/JPSJ.69.1954.

[164] J. S. Moodera and D. M. Mootoo, *Journal of Applied Physics* **76**, 6101 (1994). http://link.aip.org/link/JAPIAU/v76/i10/p6101/s1&Agg=doi, doi:10.1063/1.358318.

[165] L. J. Singh, Z. H. Barber, Y. Miyoshi, W. R. Branford, and L. F. Cohen, *Journal of Applied Physics* **95**, 7231 (2004). http://link.aip.org/link/?JAP/95/7231/1&Agg=doi, doi:10.1063/1.1667857.

[166] C. Hordequin, D. Ristoiu, L. Ranno, and J. Pierre, *The European Physical Journal B* **16**, 287 (2000). http://www.springerlink.com/index/10.1007/s100510070230, doi:10.1007/s100510070230.

[167] P. A. Lee and T. V. Ramakrishnan, *Reviews of Modern Physics* **57**, 287 (1985). http://link.aps.org/doi/10.1103/RevModPhys.57.287, doi:10.1103/RevModPhys.57.287.

[168] I. A. Campbell and A. Fert, *Ferromagnetic Materials, Volume 3*, 747 (North-Holland Publishing) (1982).

[169] J. Smit, *Physica* **17**, 612 (1951). http://linkinghub.elsevier.com/retrieve/pii/0031891451901176, doi:10.1016/0031-8914(51)90117-6.

[170] I. A. Campbell, A. Fert, and A. Jaoul, *Journal of Physics C: Solid State Physics* **3**, S95 (1970). http://stacks.iop.org/0022-3719/3/i=1S/a=310?key=crossref.7ad4c63bac4080ccfe65105e0e3add71, doi:10.1088/0022-3719/3/1S/310.

[171] B. Raquet, M. Viret, E. Sondergard, O. Cespedes, and R. Mamy, *Physical Review B* **66**, 024433 (2002). http://link.aps.org/doi/10.1103/PhysRevB.66.024433, doi:10.1103/PhysRevB.66.024433.

[172] C. M. Hurd, *The Hall Effect in Metals and Alloys* (Plenum Press) (1972).

[173] W. H. Butler, *Physical Review B* **29**, 4224 (1984). http://link.aps.org/doi/10.1103/PhysRevB.29.4224, doi:10.1103/PhysRevB.29.4224.

[174] D. A. Evtushinsky, A. A. Kordyuk, V. B. Zabolotnyy, D. S. Inosov, B. Büchner, H. Berger, L. Patthey, R. Follath, and S. V. Borisenko, *Physical Review Letters* 100, 236402 (2008).
`http://link.aps.org/doi/10.1103/PhysRevLett.100.236402`, `doi:10.1103/PhysRevLett.100.236402`.

[175] J. Sinova, T. Jungwirth, and J. Černe, *International Journal of Modern Physics B* **18**, 1083 (2004).
`http://www.worldscinet.com/ijmpb/18/1808/S0217979204024677.html`, `doi:10.1142/S0217979204024677`.

[176] R. Karplus and J. M. Luttinger, *Physical Review* **95**, 1154 (1954).
`http://link.aps.org/doi/10.1103/PhysRev.95.1154`, `doi:10.1103/PhysRev.95.1154`.

[177] M.-C. Chang and Q. Niu, *Physical Review B* **53**, 7010 (1996).
`http://link.aps.org/doi/10.1103/PhysRevB.53.7010`, `doi:10.1103/PhysRevB.53.7010`.

[178] J. Smit, *Physica* **21**, 877 (1955).
`http://linkinghub.elsevier.com/retrieve/pii/S0031891455925969`, `doi:10.1016/S0031-8914(55)92596-9`.

[179] J. Smit, *Physica* **24**, 39 (1958).
`http://linkinghub.elsevier.com/retrieve/pii/S0031891458935419`, `doi:10.1016/S0031-8914(58)93541-9`.

[180] L. Berger, *Physical Review B* **2**, 4559 (1970).
`http://link.aps.org/doi/10.1103/PhysRevB.2.4559`, `doi:10.1103/PhysRevB.2.4559`.

[181] N. Nagaosa, J. Sinova, S. Onoda, A. H. MacDonald, and N. P. Ong, *Reviews of Modern Physics* **82**, 1539 (2010).
`http://link.aps.org/doi/10.1103/RevModPhys.82.1539`, `doi:10.1103/RevModPhys.82.1539`.

[182] D. J. Thouless, M. Kohmoto, M. P. Nightingale, and M. den Nijs, *Physical Review Letters* **49**, 405 (1982).
`http://link.aps.org/doi/10.1103/PhysRevLett.49.405`, `doi:10.1103/PhysRevLett.49.405`.

[183] M. V. Berry, *Proceedings of the Royal Society A: Mathematical, Physical and Engineering Sciences* **392**, 45 (1984).
http://rspa.royalsocietypublishing.org/cgi/doi/10.1098/rspa.1984.0023, doi:10.1098/rspa.1984.0023.

[184] T. Jungwirth, Q. Niu, and A. H. MacDonald, *Physical Review Letters* **88**, 207208 (2002).
http://link.aps.org/doi/10.1103/PhysRevLett.88.207208, doi:10.1103/PhysRevLett.88.207208.

[185] G. Sundaram and Q. Niu, *Physical Review B* **59**, 14915 (1999).
http://link.aps.org/doi/10.1103/PhysRevB.59.14915, doi:10.1103/PhysRevB.59.14915.

[186] A. A. Kovalev, Y. Tserkovnyak, K. Výborný, and J. Sinova, *Physical Review B* **79**, 195129 (2009).
http://link.aps.org/doi/10.1103/PhysRevB.79.195129, doi:10.1103/PhysRevB.79.195129.

[187] A. Crépieux and P. Bruno, *Physical Review B* **64**, 014416 (2001).
http://link.aps.org/doi/10.1103/PhysRevB.64.014416, doi:10.1103/PhysRevB.64.014416.

[188] S. Onoda, N. Sugimoto, and N. Nagaosa, *Progress of Theoretical Physics* **116**, 61 (2006).
http://ptp.ipap.jp/link?PTP/116/61/, doi:10.1143/PTP.116.61.

[189] S. Onoda, N. Sugimoto, and N. Nagaosa, *Physical Review Letters* **97**, 126602 (2006).
http://link.aps.org/doi/10.1103/PhysRevLett.97.126602, doi:10.1103/PhysRevLett.97.126602.

[190] S. Onoda, N. Sugimoto, and N. Nagaosa, *Physical Review B* **77**, 165103 (2008).
http://link.aps.org/doi/10.1103/PhysRevB.77.165103, doi:10.1103/PhysRevB.77.165103.

[191] W.-L. Lee, S. Watauchi, V. L. Miller, R. J. Cava, and N. P. Ong, *Science* **303**, 1647 (2004).
http://www.ncbi.nlm.nih.gov/pubmed/15016994, doi:10.1126/science.1094383.

[192] C. M. Hurd, I. Shiozaki, and S. P. McAlister, *Physical Review B* **26**, 701 (1982).
http://link.aps.org/doi/10.1103/PhysRevB.26.701,
doi:10.1103/PhysRevB.26.701.

[193] J. J. Rhyne, *Physical Review* **172**, 523 (1968).
http://link.aps.org/doi/10.1103/PhysRev.172.523,
doi:10.1103/PhysRev.172.523.

[194] C. Kittel, *Einführung in die Festkörperphysik* (Oldenbourg), 13th edition (2002).

[195] L. Klein, J. R. Reiner, T. H. Geballe, M. R. Beasley, and A. Kapitulnik, *Physical Review B* **61**, R7842 (2000).
http://link.aps.org/doi/10.1103/PhysRevB.61.R7842,
doi:10.1103/PhysRevB.61.R7842.

[196] M. Singh, C. S. Wang, and J. Callaway, *Physical Review B* **11**, 287 (1975).
http://link.aps.org/doi/10.1103/PhysRevB.11.287,
doi:10.1103/PhysRevB.11.287.

[197] S. J. Youn and B. I. Min, *Physical Review B* **51**, 10436 (1995).
http://link.aps.org/doi/10.1103/PhysRevB.51.10436,
doi:10.1103/PhysRevB.51.10436.

[198] Y. Yao, L. Kleinman, A. H. MacDonald, J. Sinova, T. Jungwirth, D.-s. Wang, E. Wang, and Q. Niu, *Physical Review Letters* **92**, 037204 (2004).
http://link.aps.org/doi/10.1103/PhysRevLett.92.037204,
doi:10.1103/PhysRevLett.92.037204.

[199] J. Kondo, *Progress of Theoretical Physics* **27**, 772 (1962).
http://ptp.ipap.jp/link?PTP/27/772/, doi:10.1143/PTP.27.772.

[200] S.-K. Lyo, *Physical Review B* **8**, 1185 (1973).
http://link.aps.org/doi/10.1103/PhysRevB.8.1185,
doi:10.1103/PhysRevB.8.1185.

[201] Z. Q. Qiu and S. D. Bader, *Review of Scientific Instruments* **71**, 1243 (2000).
http://link.aip.org/link/RSINAK/v71/i3/p1243/s1&Agg=doi,
doi:10.1063/1.1150496.

[202] Š. Višňovský, *Czechoslovak Journal of Physics B* **36**, 1424 (1986).
http://www.springerlink.com/index/10.1007/BF01959567,
doi:10.1007/BF01959567.

[203] R. M. Osgood III, S. D. Bader, B. M. Clemens, R. L. White, and H. Matsuyama, *Journal of Magnetism and Magnetic Materials* **182**, 297 (1998).
http://linkinghub.elsevier.com/retrieve/pii/S0304885397010457,
doi:10.1016/S0304-8853(97)01045-7.

[204] K. Postava, D. Hrabovský, J. Pištora, A. R. Fert, Š. Višňovský, and T. Yamaguchi, *Journal of Applied Physics* **91**, 7293 (2002).
http://link.aip.org/link/JAPIAU/v91/i10/p7293/s1&Agg=doi,
doi:10.1063/1.1449436.

[205] J. Hamrle, S. Blomeier, O. Gaier, B. Hillebrands, H. Schneider, G. Jakob, K. Postava, and C. Felser, *Journal of Physics D: Applied Physics* **40**, 1563 (2007).
http://stacks.iop.org/0022-3727/40/i=6/a=S09?key=crossref.1bf2292e55ade6f32c92f581a620c1b5,
doi:10.1088/0022-3727/40/6/S09.

[206] M. Dumm, M. Zölfl, R. Moosbühler, M. Brockmann, T. Schmidt, and G. Bayreuther, *Journal of Applied Physics* **87**, 5457 (2000).
http://link.aip.org/link/JAPIAU/v87/i9/p5457/s1&Agg=doi,
doi:10.1063/1.373371.

[207] S. Trudel, J. Hamrle, B. Hillebrands, T. Taira, and M. Yamamoto, *Journal of Applied Physics* **107**, 043912 (2010).
http://link.aip.org/link/JAPIAU/v107/i4/p043912/s1&Agg=doi,
doi:10.1063/1.3296350.

[208] P. K. Muduli, W. C. Rice, L. He, and F. Tsui, *Journal of Magnetism and Magnetic Materials* **320**, L141 (2008).
http://linkinghub.elsevier.com/retrieve/pii/S0304885308007063,
doi:10.1016/j.jmmm.2008.06.027.

[209] M. R. Paudel, C. S. Wolfe, H. M. A. Patton, J. Simonson, I. Dubenko, N. Ali, and S. Stadler, *Journal of Applied Physics* **105**, 07E902 (2009).
http://link.aip.org/link/JAPIAU/v105/i7/p07E902/s1&Agg=doi,
doi:10.1063/1.3068530.

[210] O. Gaier, J. Hamrle, S. J. Hermsdoerfer, H. Schultheiß, B. Hillebrands, Y. Sakuraba, M. Oogane, and Y. Ando, *Journal of Applied Physics* **103**, 103910 (2008).
`http://link.aip.org/link/JAPIAU/v103/i10/p103910/s1&Agg=doi`,
`doi:10.1063/1.2931023`.

[211] S. Trudel, G. Wolf, H. Schultheiss, J. Hamrle, B. Hillebrands, T. Kubota, and Y. Ando, *The Review of scientific instruments* **81**, 026105 (2010).
`http://www.ncbi.nlm.nih.gov/pubmed/20192522`,
`doi:10.1063/1.3276715`.

[212] J. Hamrle, private communication (2010).

[213] J. van Ek, W. Huang, and J. M. MacLaren, *Journal of Applied Physics* **81**, 5429 (1997).
`http://link.aip.org/link/JAPIAU/v81/i8/p5429/s1&Agg=doi`,
`doi:10.1063/1.364562`.

[214] K. Postava, H. Jaffres, A. Schuhl, F. N. van Dau, M. Goiran, and A. R. Fert, *Journal of Magnetism and Magnetic Materials* **172**, 199 (1997).
`http://linkinghub.elsevier.com/retrieve/pii/S030488539700098X`,
`doi:10.1016/S0304-8853(97)00098-X`.

[215] F. Reinert and S. Hüfner, *New Journal of Physics* **7**, 97 (2005).
`http://stacks.iop.org/1367-2630/7/i=1/a=097?key=crossref.628e43da34de03ceaf654ceb005bc987`,
`doi:10.1088/1367-2630/7/1/097`.

[216] J.-P. Wüstenberg, M. Cinchetti, M. Sánchez Albaneda, M. Bauer, and M. Aeschlimann, *Journal of Magnetism and Magnetic Materials* **316**, e411 (2007).
`http://linkinghub.elsevier.com/retrieve/pii/S030488530700279X`,
`doi:10.1016/j.jmmm.2007.02.164`.

[217] C. J. Powell, A. Jablonski, I. S. Tilinin, S. Tanuma, and D. R. Penn, *Journal of Electron Spectroscopy and Related Phenomena* **98–99**, 1 (1999).
`http://linkinghub.elsevier.com/retrieve/pii/S0368204898002710`,
`doi:10.1016/S0368-2048(98)00271-0`.

[218] W. Kuch, *Abbildende magnetische Mikrospektroskopie*, Habilitation, Martin-Luther-Universität Halle-Wittenberg (2002).

[219] G. Schütz, W. Wagner, W. Wilhelm, P. Kienle, R. Zeller, R. Frahm, and G. Materlik, *Physical Review Letters* **58**, 737 (1987).
`http://link.aps.org/doi/10.1103/PhysRevLett.58.737`,
`doi:10.1103/PhysRevLett.58.737`.

[220] J. Stöhr, *Journal of Magnetism and Magnetic Materials* **200**, 470 (1999).
`http://linkinghub.elsevier.com/retrieve/pii/S0304885399004072`,
`doi:10.1016/S0304-8853(99)00407-2`.

[221] J. Stöhr, *Journal of Electron Spectroscopy and Related Phenomena* **75**, 253 (1995).
`http://linkinghub.elsevier.com/retrieve/pii/0368204895025375`,
`doi:10.1016/0368-2048(95)02537-5`.

[222] M. Kallmayer, private communication (2009).

ACKNOWLEDGMENTS

Due to present-day privacy concerns, I cannot not mention the persons I want to thank by name and have to keep my praise a bit general. So, here it goes:

First and foremost, I would like to thank my tutor for the opportunity to work on this topic and for his infinite patience and infinite knowledge. My colleagues—both past and present—I thank for a fruitful cooperation and lots of helpful hands and ideas during working hours. Of course, I will not forget the fun we had after work either. The same applies also to the members of the external groups I had the privilege to work with. Even though my family and friends did not directly assist me in the creation of this work, their help in many areas outside of academia was an invaluable support.

LIST OF PUBLICATIONS

1. M. Jourdan, A. Zakharov, H. Schneider, and H. Adrian:
   Transport anisotropy and $B_{c2}(\Theta, T)$ *of* UNi_2Al_3 *thin films*
   Physica B **359–361** 1153 (2005).

2. M. Kallmayer, H. Schneider, G. Jakob, H. J. Elmers, K. Kroth,
   H. C. Kandpal, U. Stumm, and S. Cramm:
   Reduction of surface magnetism of $Co_2Cr_{0.6}Fe_{0.4}Al$ *Heusler alloy films*
   Applied Physics Letters **88** 072506 (2006).

3. H. Schneider, G. Jakob, M. Kallmayer, H. J. Elmers, M. Cinchetti, B. Balke,
   S. Wurmehl, C. Felser, M. Aeschlimann, and H. Adrian:
   Epitaxial film growth and magnetic properties of Co_2FeSi
   Physical Review B **74** 174426 (2006).

4. M. Kallmayer, A. Conca, M. Jourdan, H. Schneider, G. Jakob, B. Balke,
   A. Gloskovskii, and H. J. Elmers:
   Correlation of local disorder and electronic properties in the Heusler alloy $Co_2Cr_{0.6}Fe_{0.4}Al$
   Journal of Physics D: Applied Physics **40** 1539 (2007).

5. H. Schneider, C. Herbort, G. Jakob, H. Adrian, S. Wurmehl, and C. Felser:
   Structural, magnetic and transport properties of Co_2FeSi *Heusler films*
   Journal of Physics D: Applied Physics **40** 1548 (2007).

6. M. Kallmayer, H. Schneider, G. Jakob, H. J. Elmers, B. Balke, and S. Cramm:
   Interface magnetization of ultrathin epitaxial $Co_2FeSi(110)/Al_2O_3$ *films*
   Journal of Physics D: Applied Physics **40** 1552 (2007).

7. J. Hamrle, S. Blomeier, O. Gaier, B. Hillebrands, H. Schneider, G. Jakob, B. Reuscher, A. Brodyanski, M. Kopnarski, K. Postava, and C. Felser: *Huge quadratic magneto-optical Kerr effect and magnetization reversal in the* Co_2FeSi *Heusler compound* Journal of Physics D: Applied Physics **40** 1558 (2007).
8. J. Hamrle, S. Blomeier, O. Gaier, B. Hillebrands, H. Schneider, G. Jakob, K. Postava, and C. Felser: *Ion beam induced modification of exchange interaction and spin-orbit coupling in the* Co_2FeSi *Heusler compound* Journal of Physics D: Applied Physics **40** 1563 (2007).
9. M. Kallmayer, K. Hild, T. Eichhorn, H. Schneider, G. Jakob, A. Conca, M. Jourdan, H. J. Elmers, A. Gloskovskii, S. Schuppler, and P. Nagel: *Solid state reaction at the interface between Heusler alloys and Al cap accelerated by elevated temperature and rough surface* Applied Physics Letters **91** 192501 (2007).
10. M. Kallmayer, P. Pörsch, T. Eichhorn, H. Schneider, C. A. Jenkins, G. Jakob, and H. J. Elmers: *Compositional dependence of element-specific magnetic moments in* Ni_2MnGa *films* Journal of Physics D: Applied Physics **42** 080408 (2009).
11. H. Schneider, E. Vilanova, B. Balke, C. Felser, and G. Jakob: *Hall effect in laser ablated* $Co_2(Mn,Fe)Si$ *thin films* Journal of Physics D: Applied Physics **42** 084012 (2009).
12. S. Wurmehl, J. T. Kohlhepp, H. J. M. Swagten, B. Koopmans, C. G. F. Blum, V. Ksenofontov, H. Schneider, G. Jakob, D. Ebke, and G. Reiss: *Off-stoichiometry in* Co_2FeSi *thin films sputtered from stoichiometric targets revealed by nuclear magnetic resonance* Journal of Physics D: Applied Physics **42** 084017 (2009).
13. M. Kallmayer, P. Klaer, H. Schneider, E. Arbelo Jorge, C. Herbort, G. Jakob, M. Jourdan, and H. J. Elmers: *Spin-resolved unoccupied density of states in epitaxial Heusler-alloy films* Physical Review B **80** 020406 (2009).
14. O. Gaier, J. Hamrle, S. Trudel, B. Hillebrands, H. Schneider, and G. Jakob: *Exchange stiffness in the* Co_2FeSi *Heusler compound* Journal of Physics D: Applied Physics **42** 232001 (2009).

15. H. Schneider, E. Vilanova Vidal, S. Chadov, G. H. Fecher, C. Felser, and G. Jakob:
    Hall effect and electronic structure of $Co_2Fe_xMn_{1-x}Si$ *films*
    Journal of Magnetism and Magnetic Materials **322** 579 (2010).

16. V. Ksenofontov, M. Wojcik, S. Wurmehl, H. Schneider, B. Balke, G. Jakob, and C. Felser:
    Hyperfine magnetic field on iron atoms and Co-Fe disordering in Co_2FeSi
    Journal of applied Physics **107** 09B106 (2010).

LEBENSLAUF

entfernt aus Datenschutzgründen